ABSTRACT

Investigation of Organic Dyes for Dye-Sensitized and Organic Solar Cell Applications

Andrew Gregory Smith, Ph.D.

Mentor: Kevin L. Shuford, Ph.D.

Theoretical chemistry can be a driving force for experimentalists. Using computer software, molecules can be easily changed and studied, which can save experimentalists on laboratory costs and time. This work focuses on the organic dyes in dye-sensitized and organic solar cells. More specifically, the changes in fundamental properties such as molecular orbital energies, absorption spectra, and electronic coupling are studied upon heteroatom substitution using density functional theory.

In Chapter Three, the changes in the properties of the D5 organic dye were studied upon heteroatom substitution for sulfur in the thiophene π-bridge. Sulfur was substituted for pnictogens, chalcogens, and various other elements in the second row of the periodic table. Dyes were adsorbed to $(TiO_2)_{16}$ and all substitutions besides boron had favorable electron injections. It was found that the larger elements reduce the HOMO-LUMO gap, red shift the absorption spectrum, increase the dipole moment and are energetically favorable for electron injection.

In Chapter Four, the impact the π-bridge had on the photovoltaic and charge transfer parameters of an organic photovoltaic was studied. Calculations were performed on a

variety of heteroatom substituted bridge units in both fused and unfused perylene diimide (PDI) dimers to directly compare with the previously studied thiophene bridge unit. Fused systems exhibit an improved charge transfer ratio compared to unfused systems, decreased reorganization energy, and had more favorable Gibbs free energies.

The results of Chapter Three and Chapter Four led to asking how multiple heteroatom substitutions would affect the dye molecules. Chapter Five investigates the effects of substituting two heteroatoms, one chalcogen and one pnictogen, into the PDI bay-region by the creation of a five-membered ring. A handful of the combinations were nonplanar, which shows promise for organic solar cell (OSC) applications. All combinations using oxygen for the silicon-bridged system had absorption spectra almost covering the entire visible light region. For the charge transfer properties, the main trend observed was the charge transfer ratio, which increased by a minimum of about 10^4 s^{-1} when moving along the period of the periodic table.

Investigation of Organic Dyes for Dye-Sensitized and Organic Solar Cell Applications

by

Andrew Gregory Smith, B.S.

A Dissertation

Approved by the Department of Chemistry and Biochemistry

_____

Patrick Farmer, Ph.D., Chairperson

Submitted to the Graduate Faculty of
Baylor University in Partial Fulfillment of the
Requirements for the Degree
of

Doctor of Philosophy

Approved by the Dissertation Committee

_____

Kevin L. Shuford, Ph.D., Chairperson

_____

Carlos E. Manzanares, Ph.D.

_____

Darrin J. Bellert, Ph.D.

_____

Caleb D. Martin, Ph.D.

_____

Enrique Blair, Ph.D.

Accepted by the Graduate School

August 2018

_____

J. Larry Lyon, Ph.D., Dean

Page bearing signatures is kept on file in the Graduate School.

TABLE OF CONTENTS

LIST OF FIGURES

LIST OF TABLES

ACKNOWLEDGMENTS

First off, I would like to thank my advisor Dr. Kevin Shuford for his guidance and support through my years in his laboratory. He always encouraged me throughout my studies and gave great insight in how to approach different problems. I would also like to thank the rest of my committee members: Dr. Carlos Manzanares, Dr. Darrin Bellert, Dr. Caleb Martin, and Dr. Erik Blair. All of them provided great discussions, whether it be in the classroom or the hallway, and had a great impact on my professional growth. I'd like to thank Michael Spiegel and Dr. Patrick Farmer for choosing to collaborate with me on one of their projects. I especially want to thank Dr. Charles Garner, who had a major role in telling me about Baylor. He gave me the opportunities to attend the Advanced Instrumentation Workshop and also a summer research program here at Baylor. It was from his words and these experiences I chose to attend Baylor for my graduate studies, and I have no regrets about any of it.

I would like to thank Paul Brown and Emvia Calixte of the Shuford lab. They both provided great insights into my research projects and made new suggestions I hadn't yet considered. They also provided great conversation when times were slow. I would also like to thank the undergraduate students who worked under me: Salcido Rodrigo, Patrick Englett and Samuel Lee.

I am thankful for my longtime friends Andrew Gaydos, Luke Sturgeon, Nate Sturgeon, Matt Meiste, and others, as I couldn't have accomplished this without them. I am thankful for my great friend Chris Taylor, who I have known since middle school and

went through all of my high school and undergraduate studies alongside. We constantly pushed each other and that helped me reach this point in my studies. I am also thankful for the close friends I have made at Baylor, including Michael Pettit, Ricardo Francis and Thomas Dunnam.

Lastly, I want to thank my family. My parents have supported my academic aspirations every step of the way, and their support was pivotal to me completing this milestone. I am also grateful to my wife's parents, Glenn and Cristi, who have supported us and given us a place to stay when we visit Michigan. I will be forever grateful to my wife, Kara, whose support will never be forgotten.

DEDICATION

To Kara for her love and support through my studies.

To all my family members for their support throughout my whole academic career.

To my friends, who provided countless hours of entertainment.

CHAPTER ONE

Introduction

1.1 The Need for Renewable Energy

In 2003, Richard E. Smalley, who won the Nobel Prize in Chemistry in 1996 for the discovery of buckminsterfullerene, stated that energy will be the number one problem for humanity over the next 50 years. Society will be facing an energy crisis due to the gradual depletion of fossil fuels and the increasing energy demand to support economic growth.[1] By 2040 the global energy consumption is estimated to increase by 28%, due to growth in both world population and economy.[2] Currently, about 81% of consumed energy in the United States is from non-renewable energy sources, which includes coal, petroleum and natural gas, and around 10% is from renewable energy, with the rest being from nuclear power.[2] At some point these sources will become depleted, leaving a major deficit, and is why renewable sources of energy are the future. There are several ways energy is generated using renewable, or 'green' methods, including: hydroelectric, biomass, wind, solar, and geothermal. Out of all these sources, solar only accounted for 6% of the renewable energy generated in the United States in 2017.[3] The total solar energy absorbed by the earth in an hour, was more than the world used in all of 2002. In 2000, the world energy assessment estimated that at a minimum, which accounts for cloud cover, available land area, etc., there is 1575 exajoules (EJ) of solar energy available to harness.[4] In 2015, the world only consumed 393 EJ.[5]

There has been a massive push to improve the capabilities of these renewable methods, probably the most popular being solar power. There are many different classifications of solar cells, the most well-established being crystalline silicon, multi-junction and thin-film, which have been constantly improved since the mid-1970's. These are all solid-state systems and involve a semiconductor absorber which produces an electron-hole pair, which is then separated by an electric field. However, the crux of this cell architecture is the high cost of materials and manufacturing, which has led to most research being dedicated to finding cheaper and more efficient ways to harvest solar energy. This has been done through innovation of the cell architecture, and also the creation of new materials that are both cheaper and more efficient.

1.2 Evolution of Solar Power

Electricity can be generated from sunlight in two ways: solar thermal technology and photovoltaics. Solar thermal technology utilizes mirrors to focus sunlight and heat up water to create steam, which then passes through a turbine to generate power. By no means is this is a new technology. French inventor Augustin Mouchet looked into alternative energy sources back in the late-19th century from believing that the coal would run out, and debuted a solar engine in 1878.[6] However, due to more efficient transportation of coal, and poor efficiency, the French government deemed solar energy uneconomical. Over the years this technology has been refined and in 2014 the Ivanpah facility was built in the Mojave Desert, which is largest solar thermal plant ever built. The plant produces 392 MW of power but does use natural gas to start up every day. However, this is substantially more than a typical natural gas plant would produce with the same amount of gas.

Solar photovoltaics have seen more growth than solar thermal technology. The Solar Star plant, which occupies approximately the same amount of land as the Ivanpah facility, produces 579 MW of power. This is the largest solar cell plant in the US, and there are others in Asia that can produce over 1000 MW. Solar photovoltaics can be traced back many years, but the "photovoltaic effect", which is the creation of current and voltage due to exposure to sunlight, was first experimentally demonstrated by the French physicist Edmond Becquerel in 1839.[7] He discovered that by putting silver chloride in acidic solution connected to platinum electrodes, voltage and current were generated when illuminated with light. He could not explain the effect, but Albert Einstein was able to many years later.[8] In 1873, Willoughby Smith published in Nature detailing what he discovered regarding the photoconductivity of selenium.[9] In 1883 Charles Fritts constructed the first solar cell by coating selenium with gold to form the junctions, however, it only had an efficiency of approximately 1%.[10] It wasn't until the 1940's that Vadim Lashkaryov and Russell Ohl discovered p-n junctions in copper oxide and silicon, respectively.[11-13] In 1954 the first practical solar cell was developed by Daryl Chapin, Calvin Fuller and Gerald Pearson at the Bell Laboratories. It was the first silicon solar cell and had an efficiency of 6%, much better than previously constructed photovoltaics.[14]

Even though this technology was too expensive to practically use at that point in time, the constant refinement throughout the decades has just recently led it to becoming a viable option. From this, different photovoltaic architectures have been developed, which can be divided into two classifications: crystalline silicon (c-Si) and thin-film. Crystalline silicon cells are the most widespread solar cells used, accounting for over 90% of the photovoltaic technology market share.[15] Even though c-Si cells are the most expensive,

they have proven to be the most efficient and stable. However, thin-film photovoltaics have been extensively researched and have shown to have several advantages over c-Si, such as: being flexible, more resistant to higher temperatures, easier mass production, and cheaper materials. There are many different materials used in thin-film cells, most notably CdTe, GaAs and CIGS.[15] These are examples of solid-state systems and involve a semiconductor absorber producing an electron-hole pair, which is then separated by an electric field. However, the crux of this cell architecture is the high cost of materials and manufacturing, which has led to most research being dedicated to finding cheaper and more efficient ways to harvest solar energy. Two newer thin-film photovoltaic technologies that have been risen up to combat these issues are dye-sensitized solar cells (DSSC) and organic solar cells (OSC).[16-17]

1.3 Efficiency Limits

In 1961, William Shockley and Hans J. Queisser published their paper on the maximum efficiency of an ideal photovoltaic cell.[18] A maximum efficiency of 30% and optimum energy gap of 1.1 eV was found when under the assumption that the sun and cell are blackbodies with temperatures of 6000 K and 300 K, respectively. There have been many other papers discussing the maximum efficiency, but all result with the values for the efficiency and energy gap similar to Shockley and Queisser.[19-21] Figure 1.1 shows the energy losses estimated by Archer *et al.* in 1990. They estimated that ~31% of the light energy is lost due to being too low to excite the dye ($E < E_g$), where E and E_g represent the light energy and energy gap, respectively. They also estimated ~23% of the energy being lost to intraband thermalization of the charge carriers, 12% lost due to entropy, and 1% lost

from radiative recombination. This leaves a maximum efficiency of 33%, with an optimum energy gap of 1.34 eV.[19]

The variations in the calculated values can often be attributed to using different solar spectra, or black body temperature of the sun. The most common solar spectra used for flat panel photovoltaic testing today is the air mass 1.5 global (AM1.5 Global) spectral irradiance distribution, shown in Figure 1.2. Essentially, this spectrum is defined by the

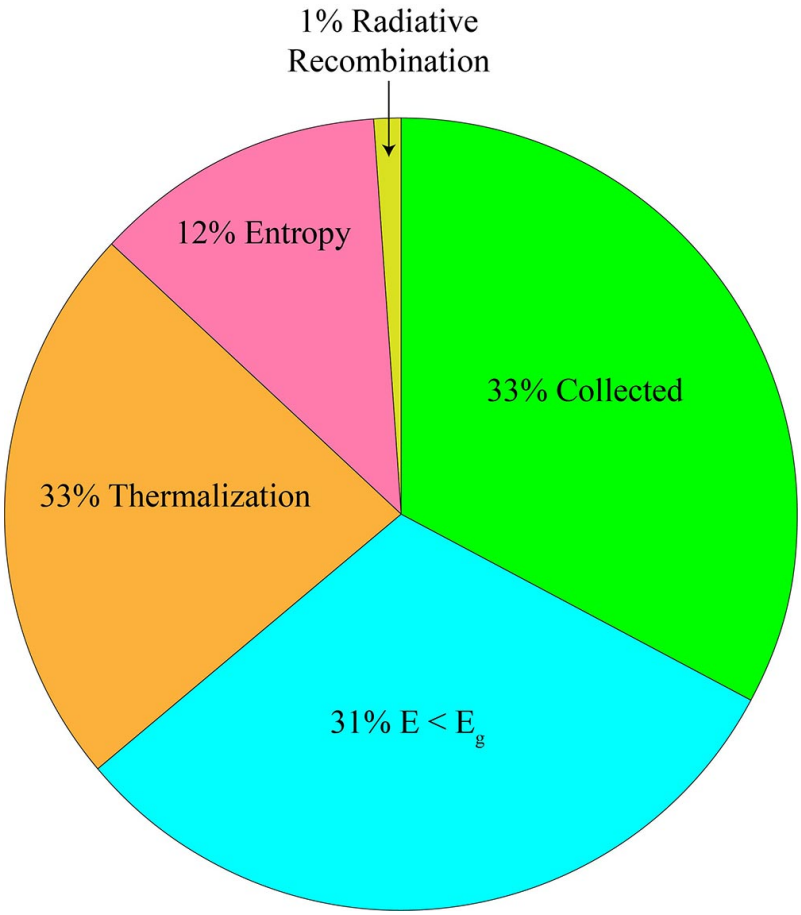

Figure 1.1. Pie chart illustrating the 33% efficiency limit and where the rest of the energy is lost.

angle of the sun to the Earth's surface. The AM coefficient is the optical path length through the Earth's atmosphere, and AM1.5 was selected to be representative of the

average solar radiation over the United States.[22] The American Society for Testing and Materials made this a standard for photovoltaic research. This spectrum has been refined and the current accepted version for flat panel photovoltaics is denoted as the G173-03 standard (Figure 1.2).[23]

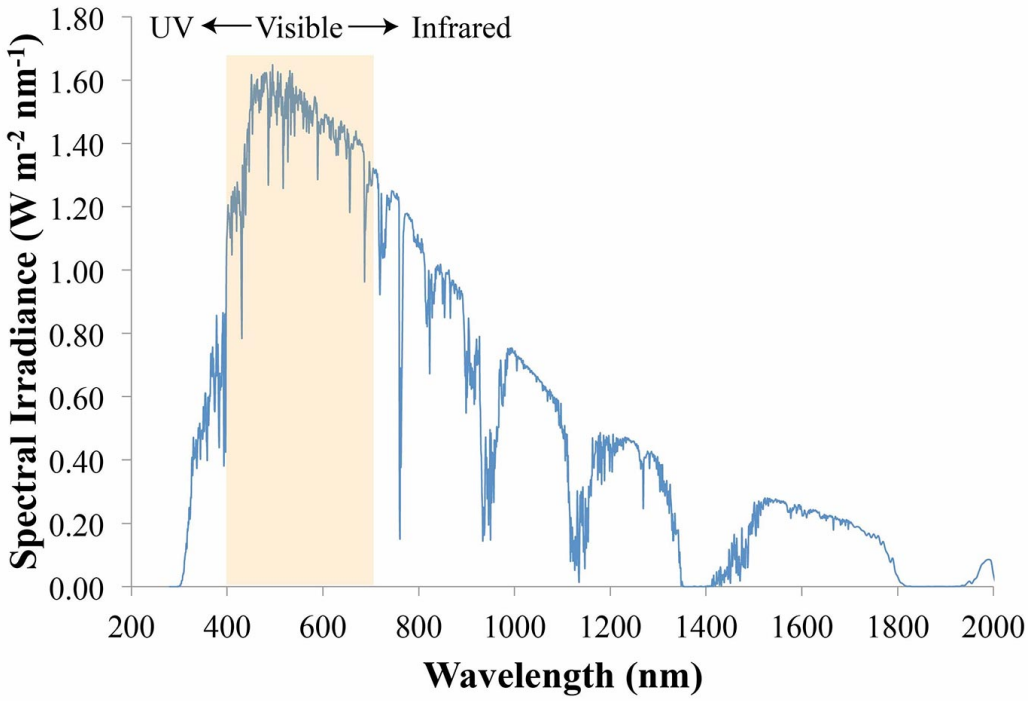

Figure 1.2. G173-03 Am 1.5 solar spectrum. Highlighted region signifies the visible light region.

1.4 Dye-Sensitized Solar Cell

The underlying concept of a DSSC was first outlined in the 1870's. By itself, silver halide shows no activity to visible light, but Vogel et al. demonstrated that when put in a gelatin medium, it became sensitive to this range of light. This concept was further proved by James Moser in 1887, but voltages were only around 0.04 V, much too low for a photovoltaic device. Not much improvement occurred until Hishiki (1965) and Gerischer

(1968) improved upon Moser's work by investigating zinc oxide with cyanine and rose bengal dyes, respectively. Later, Daltrozzo and Tributsch adsorbed Rhodamine B to ZnO, observing the transfer of electrons from the dye to ZnO. It wasn't until 1977 that Spitler and Calvin replaced ZnO with titanium dioxide (TiO_2), which would later become the most popular metal oxide for DSSC's.

It took until the 1990's for DSSC's to become a practical photovoltaic device. The first efficient cell, developed by Michael Grätzel and Brian O'Regan in 1991, had an overall efficiency of 7%. This was less than the silicon cells at the time, but it exhibited a 12% efficiency in diffuse light, which was a problem for other solar cells. The DSSC breaks away from other solar cell technologies in that it separates light absorption and charge transport. In a c-Si cell, the silicon does both actions, while a DSSC utilized the inorganic dye N3 as the absorber, and a TiO_2 semiconductor layer for charge transport.

In the beginning a lot of research went in to developing variations of this ruthenium dye to improve the efficiency. However, it was soon realized that using ruthenium would be too expensive for mass production, which led to the investigation of other metals. A DSSC using a zinc porphyrin complex has recently reached an efficiency of 13%, which set the DSSC efficiency record in 2014, proving to be a suitable replacement for ruthenium-based dyes.[24] There has been a push, however, to eliminate the use of metal-complexes as the dye sensitizer and develop organic replacements, which would dramatically reduce fabrication costs. Organic dyes have improved long term stability, the advantage of having a wide variety of easily modified structures, and also larger absorption coefficients, stemming mainly from intramolecular π-π^* transitions. At first these organic dyes lacked in efficiency compared to the Ru-based dyes, but have recently surpassed metal-based

dyes, setting a new efficiency record of 14.3% in 2015 by co-sensitization of two different organic dyes.[25]

The architecture of a DSSC (Figure 1.3) can be split into five parts, which in order starting from where the sunlight enters the cell:[26]

1. Transparent glass allowing light to pass into the cell.
2. A transparent conducting oxide (TCO) acting as the anode. Tin oxide doped with either fluorine (FTO) or indium (ITO) is the most prevalent material.
3. The active layer which includes:
    i. A mesoporous oxide layer which is deposited on the anode and is typically titanium dioxide (TiO_2), although other metal oxides like ZnO are currently being explored.
    ii. A monomolecular layer of dye molecules, such as N3 in the cell developed by Michael Grätzel. This is deposited onto the oxide layer and is used to harvest incident sunlight.
    iii. An electrolyte layer usually containing some organic solution, like ethanol (EtOH) or dichloromethane (DCM), and a redox mediator. The most prevalent mediator used has been an iodide/triiodide couple, but more recently metal complexes utilizing cobalt or copper have been gaining traction.
4. A counter electrode similar to layer (2) in which a glass sheet is covered in FTO or ITO, but is then coated with a catalyst such as platinum. This layer acts as the cathode of the cell and catalyzes the reaction to regenerate the redox mediator.

The mechanism of a DSSC is based on a photo-electrochemical process.[26-27] When illuminated the dye becomes excited, bringing an electron from the highest occupied molecular orbital (HOMO) to the lowest occupied molecular orbital (LUMO):

$$S + h\nu \rightarrow S^*$$

Where S^* denotes the excited state of the dye molecule. The excited electron is then injected from the LUMO of the dye, to the semiconductor surface, which then travels through this layer to reach the electron collecting photoanode. This leads to the dye molecule becoming oxidized:

$$S^* \rightarrow S^+ + e^-_{TiO2}$$

where S^+ is the oxidized state and e^-_{TiO2} represents the electron that has been transferred to the semiconductor layer. At this point, the dye molecule can no longer donate electrons unless it is restored to its neutral ground state. This is done using a redox mediator as a reducing agent via:

$$S^+ + M \rightarrow S + M^{ox}$$

where M/M^{ox} represent the redox mediator in its neutral and oxidized states, respectively. The mediator is then reduced back to its neutral state at the counter electrode:

$$M^{ox} + e^-_{CE} \rightarrow M$$

where e^-_{CE} represents the electron coming from the counter electrode. It is at this point the whole system is back to its original state and the process can be repeated. This process is occurring consistently and creates a current in the cell, which in turn generates electricity. The mechanism of the cell is illustrated in Figure 1.4. With the path of the electron, and also path of recombination, being displayed. The electron travels between the cathode and

anode, and the dye is excited from a ground to excited state. The overall photo-conversion efficiency (PCE or η) of the cell is defined as:[28]

$$\eta = FF\frac{V_{oc}J_{sc}}{P_{inc}}$$

where V_{oc} is the open-circuit voltage, J_{sc} is the photocurrent density at short circuit, FF is the fill factor, and P_{inc} is the power of incident light.

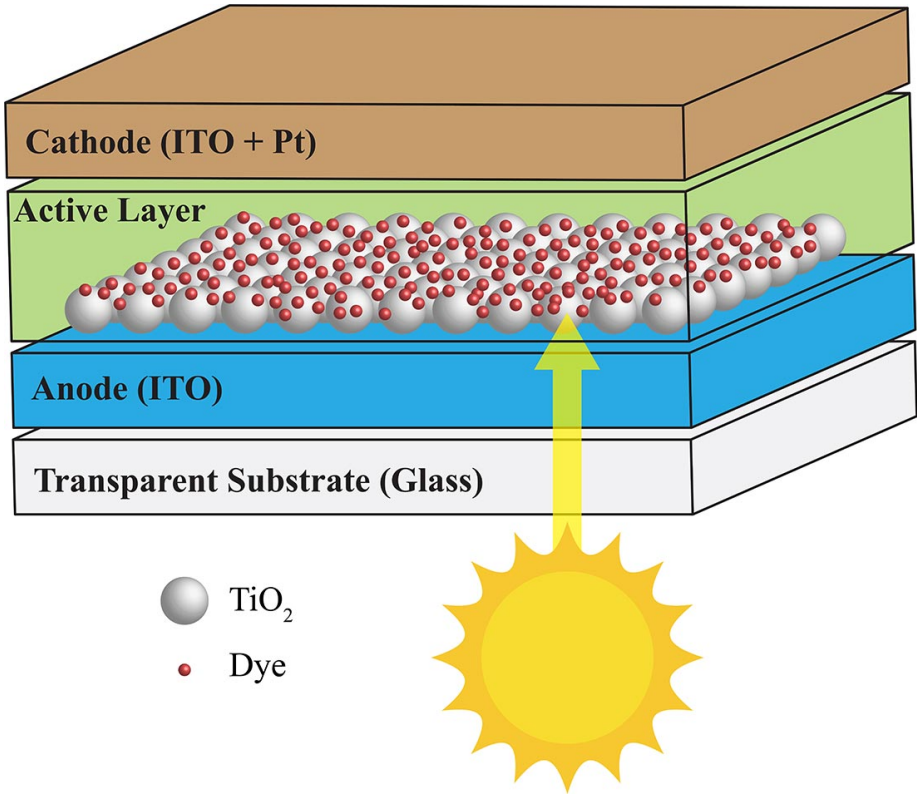

Figure 1.3. Architecture of a dye-sensitized solar cell

1.5 Organic Solar Cells

At first, DSSC's were created by the desire to create more economical solar cells compared to the c-Si cells at the time. Then, the desire not to use rare metals like ruthenium in DSSC's drove the movement in creating organic molecules to act as the photosensitizer. This led to the idea of eliminating the metal oxide surface as well, and thus an entirely new

classification of solar cell was created, called an organic solar cell (OSC).[17, 29-32] This involves one or more organic dyes in an active layer which absorb solar radiation to reach an excited state and perform intermolecular electron transfer to transport charge throughout the cell. Due to the infancy of this technology it is sometimes referred to as an organic photovoltaic (OPV).

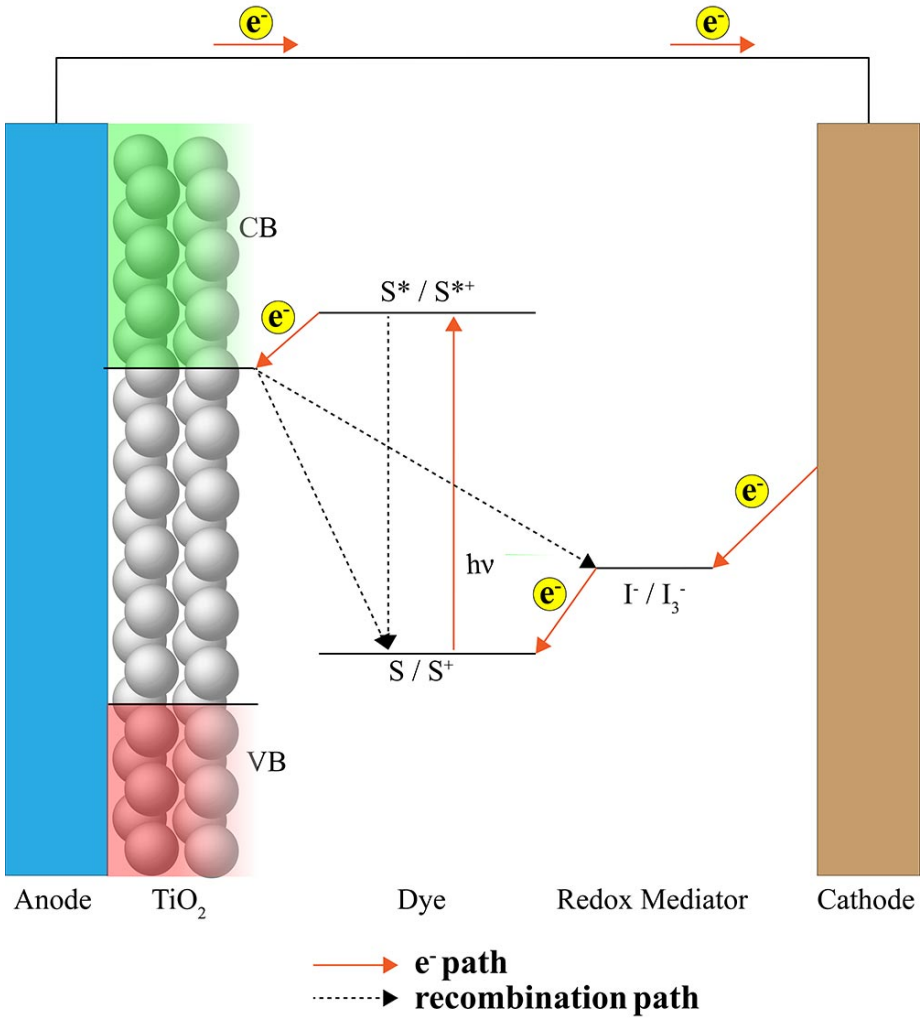

Figure 1.4. Mechanism of electron transfer in a dye-sensitized solar cell. The electron path is illustrated with the solid line, and the recombination pathways with a dotted line.

In 1906, Pochettino published a paper making anthracene the first organic compound in which photoconductivity was observed.[29] Originally, organic solar cells

utilized an active layer made of a single organic material put between two electrodes. Upon absorption of light, Coulomb-bound electron-hole pairs are created called excitons. The exciton would then diffuse to one of the electrodes and dissociate so the electron or hole can be collected. This single layer has the intrinsic limitation that makes one have to choose whether to use a p-type (donor) or n-type (acceptor) organic compound. This limitation makes it so the organic layer cannot properly generate individual charges from the formed excitons. The Coulombic energy binding the electron and hole together is ~0.35-0.50 eV for most organic semiconductors.[33] This kind of exciton is commonly defined as a Frenkel exciton, due to its molecular localization and the Coulombic binding energy exceeding the thermal energy at room temperature.[34] Weakly bound, delocalized excitons (< 0.1 eV) are defined as Wannier-Mott, which are the type in bulk semiconductor solar cells using materials like Si, CdS and CdSe.[35-36] In order to overcome this binding energy, a driving force is needed to dissociate the Frenkel exciton, and the lack of one is one reason why the single layer cells were inefficient.

Since the invention of the organic solar cell, it can be argued that there are three pioneering publications that have brought OSC's to where they are today. The first being the fabrication of a bilayer cell in 1986 by Tang et al., which dramatically improved the efficiency over the current OSC's at the time to an unprecedented ~0.9%.[17] This cell split the active layer into two separate layers, one made of a donor material, and the other an acceptor. The cell mechanism involves the donor layer absorbing light to become excited and form an exciton, diffusion of the exciton to the bilayer interface, and then dissociation into an electron and hole. The energy difference between the donor and acceptor orbitals acts as the driving force mentioned earlier to dissociate the exciton, by providing the

electron a lower energy state within the acceptor. The electron is transferred to the acceptor and travels to the electrode, while the hole remains in the donor and travels to the opposite electrode. Most of the improvement in efficiency can be assigned to the inclusion of this driving force.[34] However, the future for the bilayer system was bleak because there was still a limitation on poor charge transport inside the two individual layers. This is due to the fact that the diffusion length of an exciton is only ~10 nm, while the donor layer thickness would be >100 nm.[37-39] This meant only a small fraction of excitons would make it to the bilayer interface and dissociate. Also, vacuum systems were still necessary for depositing the organic layers, which wasn't ideal.

1.5.1 Bulk-Heterojunctions

The second and third milestones that led organic solar cells to where they are today are closely related. There was the introduction of bulk heterojunction (BHJ) architectures in 1992, which utilized polymers and fullerene,[31] and then a few years later in 1995, Yu et al. published the first work on solution processed BHJ solar cells.[32] This cell utilized $PC_{61}BM$ instead of the bare C_{60} fullerene, and resulted in an efficiency of 2.9%. In a BHJ, there is a single active layer, however, it contains both donor and acceptor organic molecules. The donor is typically a polymer, while the acceptor is frequently a fullerene derivative like [6,6]-phenyl-C_{61}-butyric acid methyl ester ($PC_{61}BM$) and [6,6]-phenyl-C_{71}-butyric acid methyl ester ($PC_{71}BM$).[32-33] The active layer is distributed on the cell by spin-coating the donor-acceptor mixture,[40-41] or through co-deposition.[42-43] Due to the donor and acceptor materials being thoroughly mixed, there are now a plethora of donor-acceptor junctions throughout the active layer, as opposed to a single junction for the bilayer system. This allows excitons to efficiently dissociate, and create electron-hole pairs, however, the

downside to this mixture is that is more likely the charge carriers recombine. Overall, the improvement in device efficiency vastly outweigh the flaws. Figure 1.5 illustrates the different active layer architectures for OSC's, and also molecular structures of the donors and acceptors used in the first cells.

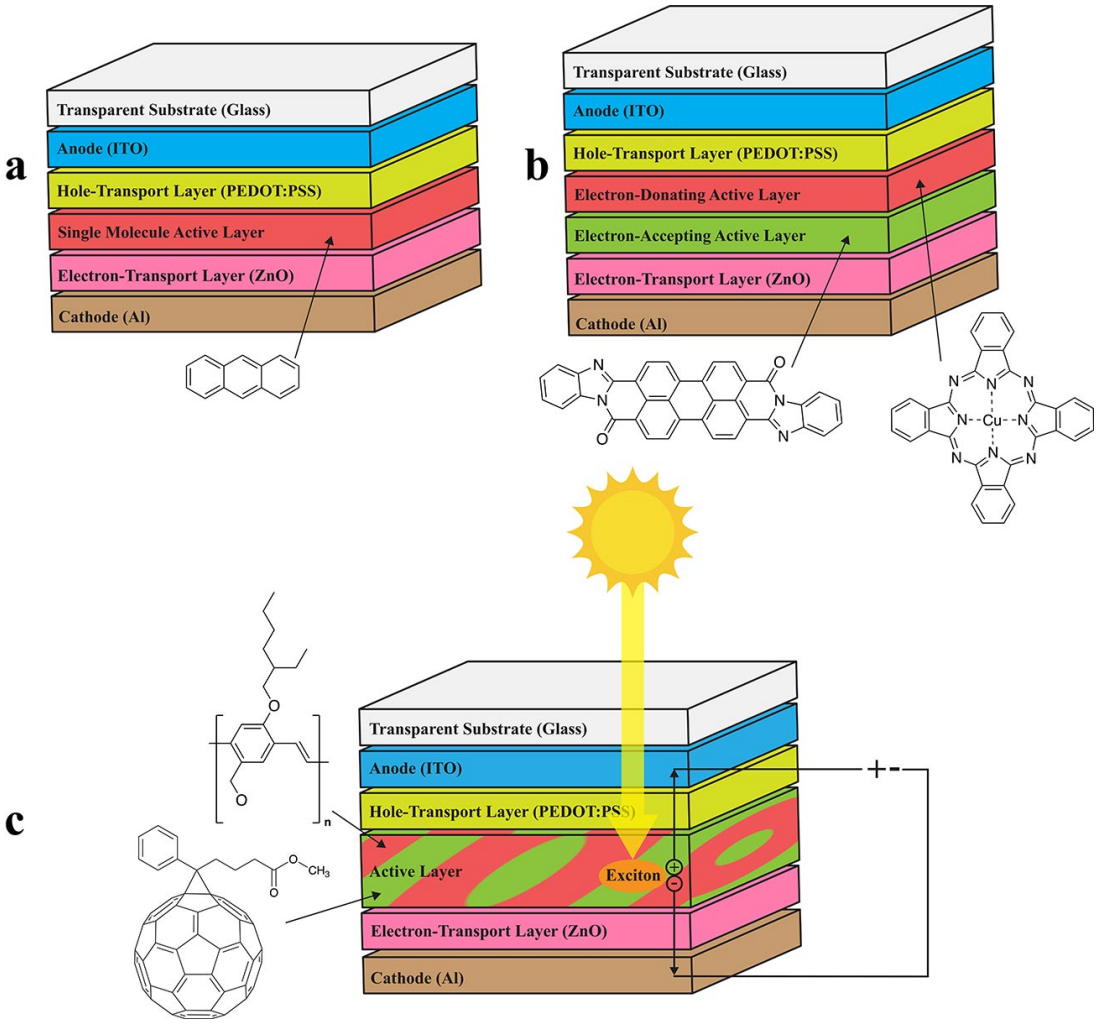

Figure 1.5. The architecture for the a) single active layer b) bilayer and c) bulk-heterojunction cells.

Even though there are a variety of cell structures used in organic solar cells, the typical cell is similar to a DSSC and uses the following layers:[33]

1. Glass that allows light to pass through into the cell.

2. The anode which is typically either fluorine (FTO) or indium tin oxide (ITO), which is also transparent, so light can reach the active layer.
3. Hole-transport layer (HTL) to minimize carrier recombination by blocking electrons and transporting holes, and is usually PEDOT:PSS. Also, it improves Ohmic contact between the active layer and anode.[44]
4. The active layer of the cell. In the case of a BHJ this contains the mixture of donor and acceptor molecules, which can range from polymers, to fullerenes or other small molecules.
5. An electron-transport layer (ETL) to block holes and transport electrons. ZnO has shown to be an effective material and is used extensively.[45-48]
6. The cathode of the cell, which is typically a low work-function material like aluminum.

The mechanism of the BHJ cell is similar to that of bilayer cells, since they both utilize donor and acceptor molecules. The elementary steps for the photoinduced charge separation are:[49]

$$\mathrm{D} + A + \mathrm{h}\nu \rightleftharpoons \mathrm{D}^* + A$$

$$\mathrm{D}^* + A \rightleftharpoons [D^*, A]$$

$$[D^*, A] \rightleftharpoons [D^+, A^-]$$

$$[D^+, A^-] \rightleftharpoons \mathrm{D}^+ + A^-$$

which involves, in order, photoexcitation of the donor, diffusion of the exciton forming an encounter pair, electron transfer to form a geminate pair, and charge separation. These steps are illustrated below, with Figure 1.6a showing the steps within the active layer, and Figure

1.6b illustrating the process in relation to the HOMO and LUMO orbitals. These processes can advance in a similar way in the case of an excited acceptor, which is discussed later.

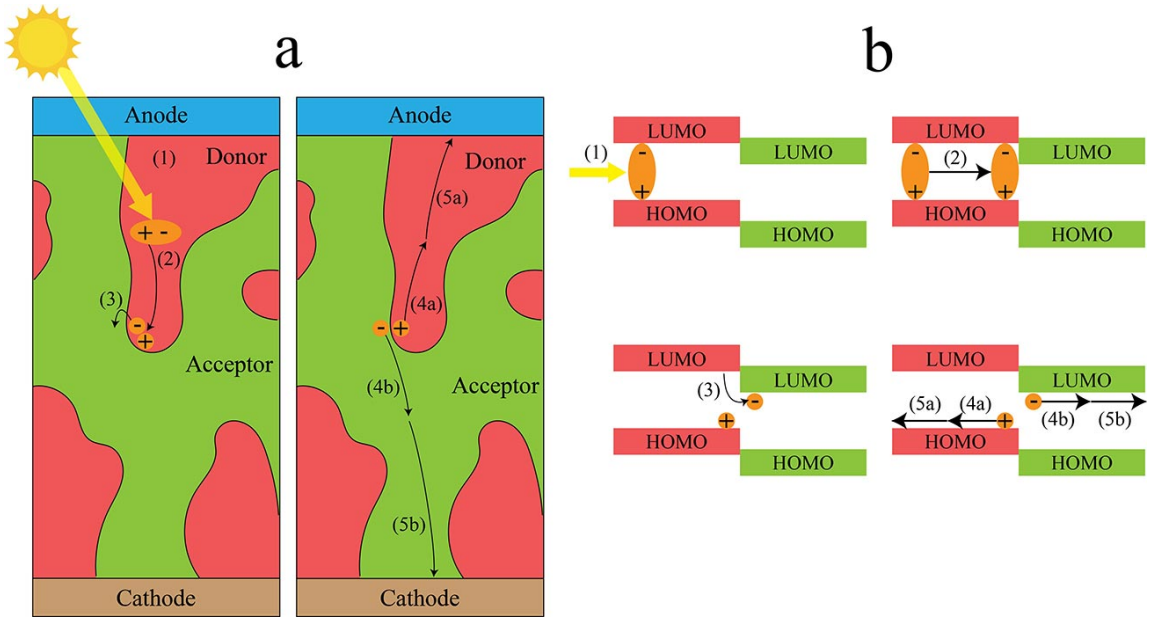

Figure 1.6. Mechanism of a BHJ cell with relation to a) the active layer and b) the HOMO and LUMO orbitals. 1) photoexcitation of the donor 2) diffusion of the exciton 3) electron transfer forming a geminate pair 4) charge separation and 5) charge transfer to cathode or anode. For steps 4 and 5, 'a' and 'b' signify the hole and electron transfer, respectively.

1.5.2 Non-Fullerene Acceptor

Over the last 10 years, more attention has been given to the development of new donor materials, rather than new acceptors, for organic solar cells. The most common acceptors have been derivatives of C_{60} fullerene, such as $PC_{61}BM$ and $PC_{71}BM$. These fullerene derivatives have positive qualities like high electron mobilities, 3D character and delocalized LUMOs, and readily forms interpenetrating networks with donor molecules, which aides charge separation and transport. These qualities helped lead single-layer OSC's to efficiencies between 10-11%,[50-51] but there are negatives associated with fullerene derivatives. It is difficult to tune the molecular orbital energy levels in fullerene

derivatives, and have weak absorption in the visible and NIR regions.[52] There are also many long-term thermal and photochemical stability concerns,[53-54] as well as high material and production costs.[55]

Organic small molecules can address all these negatives associated with fullerenes such as: easily tunable chemical structures and orbital energies, increased absorption in the visible and NIR regions, improved long-term stability, and can be more easily synthesized.[52] These qualities led to the development of organic non-fullerene (NF) acceptors for OSCs. However, even with all the positives, in the beginning poor efficiencies were observed for cells using NF acceptors. This has been attributed to the planar nature of the organic molecules, leading to premature aggregation and crystallization.[56] This prevents sufficient donor-acceptor mixing, and leads to poor efficiencies. However, much progress has been made within the last few years and efficiencies have improved from ~6% to >14% for OSCs based on NF acceptors,[57-58] while fullerene-based cells still have efficiencies <13%.[59-60]

There have been many advances in the design of new organic NF acceptors, and the two classes of molecules leading the way are perylene diimides (PDIs) and fused-ring electron acceptors (FREAs), both shown in Figure 1.7.[61-62] Both of these classes of molecules exhibit strong absorption in the visible-NIR region, have high electron mobilities, and have easily tunable electronic and optical properties.[52] The downside to PDIs is that they tend to suffer due to their planarity, forming π stacks in their crystals.[63] However, connecting multiple PDIs by a bridge unit has improved their miscibility with donor molecules, and have made them excellent NF acceptors.[64] PDIs have been used as an acceptor material for many years, even being in the first bilayer cell by Tang et al.,[17] but

FREAs are a more recent development. A FREA consists of a fused-ring bridge with a strong electron withdrawing group at each end. The presence of side chains along the bridge affect the miscibility with donor molecules, mainly by preventing the π stacking issue seen in other organic NF acceptors like PDI.[65] The leading organic solar cell utilizes a FREA, and has an efficiency of 15%.[66]

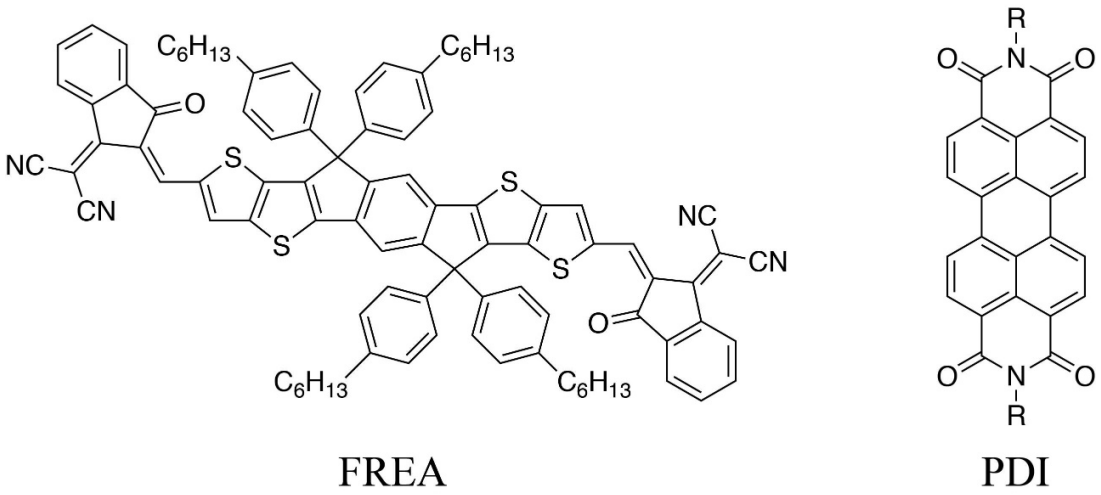

Figure 1.7. Chemical structures for fused-ring electron acceptors (FREA) and perylene diimides (PDI).

1.6 Objective

The objective of the research presented in this dissertation was to thoroughly investigate the organic dyes used in photovoltaic applications, and more specifically, DSSC and OSC devices. There are a plethora of publications in the literature regarding various aspects of these solar cells including surface materials, electrodes, dyes, etc., however, there is still much we do not know about these devices. The use of organic dyes instead of inorganic dyes that utilize rare metals has been of strong interest and efficiencies increase every year. From a theoretical perspective there are still a lot of unanswered questions

about why certain organic dyes produce better efficiencies than others, also, determining properties that match experimental values is still a challenge.

Thiophene has played a key role in organic dyes for many years due to its electronic properties and is used in most organic dyes as a π-bridge. Our first thought was to question why thiophene was the most common, and when no answer was found in the literature, we sought to answer it ourselves. So, throughout this dissertation we seek to answer this question by substituting various heteroatoms for sulfur in the thiophene ring. The change in several properties such as the molecular orbital energies and absorption spectra, are laid out and thoroughly analyzed. Chapter Three studies organic dyes for DSSCs and shows that π-bridge systems using a phosphorus or selenium atom in the five-membered ring could prove to be more efficient than thiophene. Chapter Four looked at OSCs, and found that larger atoms, had improved photovoltaic as well as Marcus theory parameters, and show potential to perform better than typical thiophene linkers. Chapter Five also investigated OSCs, focusing on utilizing multiple heteroatoms in the organic dye, separate from the thiophene bridge, and found that combinations of S+P and S+As would most likely provide the best results in an actual cell, regardless if the bridge was thiophene or not. Throughout each of these chapters the most accurate methods are determined, to ensure that the most accurate results are obtained.

1.7 Author Contributions

Rodrigo Salcido was a contributor for NICS analysis calculations done in Chapter Four. Andrew G. Smith did all other data collection. Andrew G. Smith also did all of the manuscript writing, with edits by Kevin L. Shuford.

CHAPTER TWO

Overview of Theories and Methods

2.1 Schrodinger Equation

All quantum mechanics methods stem from the Schrödinger equation. This equation for an N-electron system, in its time-independent form, and governed by the Born-Oppenheimer principle is:

$$\mathbf{H}\Psi = E\Psi \tag{2.1}$$

where $\Psi = \Psi(x_1, x_2, ..., x_N)$ is the wavefunction, E is the electronic energy, and **H** is the Hamiltonian operator. In its basic form:

$$\mathbf{H} = \mathbf{T} + \mathbf{V} = (\mathbf{T}_n + \mathbf{T}_e) + \left(\mathbf{V}_{en} + \mathbf{V}_{nn} + \mathbf{V}_{ee}\right) \tag{2.2}$$

where T and V represent the kinetic and potential energies, respectively. When expanded, the kinetic energy consists of two terms, the kinetic energy of electrons ($\mathbf{T}_e$) and nuclei ($\mathbf{T}_n$). The potential energy can be expanded into three different Coulombic forces: the electron-nucleus attraction ($\mathbf{V}_{en}$), nucleus-nucleus repulsion ($\mathbf{V}_{nn}$), and electron-electron repulsion ($\mathbf{V}_{ee}$). It is because of the last term, the electron-electron repulsion, that the equation is not separable into single particle terms. This is problematic because for each additional electron included in the system, the number of parameters increases exponentially. This is why H and He^+ are the systems students solve for when learning quantum mechanics, since both only have one electron.

2.2 Hartree-Fock Theory

This issue regarding the many-body Hamiltonian has led to the development of numerous approximations in order to solve for the energy of multi-electron systems. One such theory is known as Hartree-Fock (HF), or sometimes the Self-Consistent Field technique (SCF), which is one of the earliest computational methods to solve the Schrödinger equation.[67-68] This formed the foundation of modern molecular orbital theory, approximating that there are no electron-electron interactions and are described using one-electron wavefunctions.

Hartree-Fock theory is based on the variational principle. To explain this principle, the expectation value for the energy of a system with a given wavefunction is shown below.

$$E = \frac{\langle \Psi | \mathbf{H} | \Psi \rangle}{\langle \Psi | \Psi \rangle} = \int_{-\infty}^{\infty} \Psi^* \mathbf{H} \Psi \, dr^3 \tag{2.3}$$

The variational principle states that for any wavefunction other than the true one, the energy will always be greater than the true energy.

$$E \geq E_0 \tag{2.4}$$

where E_0 represents the true ground state energy of the system.

Using the variational principle, Hartree-Fock theory attempts to minimize the total energy of a system by iteratively guessing the one-electron wavefunction. Before this process starts, Hartree-Fock theory makes two approximations: nuclear motion is not considered because electrons move much faster (Born-Oppenheimer approximation) and there are no electron-electron interactions. Under these approximations an N electron system can be described as the product of each wavefunction.

$$\Psi(x_1, x_1, \ldots, x_n) = \psi_1(x_1)\psi_2(x_2)\ldots\psi_N(x_N) \tag{2.5}$$

This, however, does not account for the Pauli Exclusion Principle. An antisymmetric condition must be set, and written as a Slater determinant:

$$\Psi_{HF} = \frac{1}{\sqrt{N!}} \begin{vmatrix} \psi_1(x_1) & \cdots & \psi_N(x_1) \\ \vdots & \ddots & \vdots \\ \psi_1(x_N) & \cdots & \psi_N(x_N) \end{vmatrix} \tag{2.6}$$

where x_i represents the space and spin coordinates of electron *i*. This represents each electron as associated with every orbital, while remaining indistinguishable from each other. The Hartree-Fock energy eigenvalue (E_{HF}) is then calculated by:

$$E_{HF} = \langle \Psi_{HF} | \mathbf{F} | \Psi_{HF} \rangle = \sum_{i=1}^{N} H_i + \frac{1}{2} \sum_{i,j=1}^{N} \left(J_{ij} - K_{ij} \right) + V_{nn} \tag{2.7}$$

where **F** represents the Hartree-Fock Hamiltonian, commonly known as the Fock operator. H_i is a one-electron term that encompasses the kinetic energy and electron-nuclei Coulombic attraction. J_{ij} and K_{ij} are both two-electron terms and represent the electron-electron Coulombic repulsion and exchange integral, respectively. Note that J_{ij} does not account for every individual electron interaction. Instead, it is assumed there is an average potential generated by the electrons, and each electron experiences this potential created by the other electrons in the system. V_{nn} pertains to the nuclear repulsions, and since it does not involve electronic coordinates, it is not included in the sum functions. The variation principle is then applied by minimizing the ground state energy with respect to the spin orbitals.

Later, in 1951, Roothaan proposed to expand the molecular using a linear combination of atomic orbitals (LCAO), represented as:[69]

$$\psi_i = \sum_{s=1}^{m} C_{si} \chi_s \tag{2.8}$$

where χ and C represent the basis functions and molecular orbital coefficients, respectively. This new representation of the molecular orbitals is substituted into the previous HF equations, thus changing the Schrodinger equation.

$$\sum_s C_{si}\mathbf{F}\chi_s = E_i \sum_s C_{si}\chi_s \tag{2.9}$$

When this is multiplied by χ_r^*, integrated, and put into matrix form, it leads to the relation:

$$\sum_{s=1}^{b} C_{si}(F_{rs} - E_i S_{rs}) = 0\ , \quad r = 1, 2, \ldots, b \tag{2.10}$$

where F_{rs} and S_{rs} represent the Fock and overlap matrices, respectively. These are defined as:

$$F_{rs} = \langle \chi_r | F | \chi_r \rangle\ , \quad S_{rs} = \langle \chi_r | \chi_s \rangle \tag{2.11}$$

These equations are more easily solved in matrix form. When the above equation is written in matrix notation, it becomes:

$$\sum_{s=1}^{b} F_{rs}C_{si} = E_i \sum_{s=1}^{b} S_{rs}C_{si}\ , \quad r = 1, 2, \ldots, b \tag{2.12}$$

Or more simply,

$$\mathbf{FC} = \mathbf{SC}E \tag{2.13}$$

Where **F**, **S** and **C** are all square matrices of order *b*. **F** is the Fock matrix, **S** is the overlap matrix, and the elements of **C** are the coefficients C_{si}. E is a diagonal matrix whose diagonal elements are the orbital energies E_i.

First, the Fock and overlap matrices will be generated using a guess, then diagonalization of **F** will be done which will produce an E value for every molecular orbital. This result is fed back into itself, and, using the variational principle, will be done iteratively until E converges.

2.3 Density Functional Theory

2.3.1 Hohenberg-Kohn Theorems

The electronic Hamiltonian, in atomic units, is:

$$\hat{H} = -\frac{1}{2}\sum_{i=1}^{N}\nabla_i^2 + \sum_{i=1}^{N}\upsilon(\mathbf{r}_i) + \sum_{j}\sum_{i<j}\frac{1}{r_{ij}} = T + V_{ne} + V_{ee} \qquad (2.14)$$

where T, V_{ne} and V_{ee} represent the kinetic energies, electron-nuclear attractions, and electron-electron repulsions, respectively. The $\nu(\mathbf{r})$ term included in the electron-nuclear attractions term is defined as the external potential energy acting on electron *i* at point **r**. This is because it originates from charges external to the system of electrons. In 1964, Hohenberg and Kohn proved that the ground state electron density, $\rho_0(\mathbf{r})$, determines the external potential and number of electrons.[70] They devised two theorems, the first being that at the ground state energy, there is a unique electron density and corresponding external potential. The ground state energy is a functional of the density:

$$E_0 = E_0[\rho_0] = T[\rho_0] + V_{ne}[\rho_0] + V_{ee}[\rho_0] = \int \rho_0(\mathbf{r})\upsilon(\mathbf{r})d\mathbf{r} + F[\rho_0] \qquad (2.15)$$

Since $\rho_0(\mathbf{r})$ can be used to determine the electronic wave function, and the T, V_{ne} and V_{ee} terms from earlier are properties determined from the electronic wave function, each of these terms can be expressed as a functional of $\rho_0(\mathbf{r})$. The electron-nuclear attraction potential energy term is known, however, the $T[\rho_0]$ and $V_{ee}[\rho_0]$ terms are not. When V_{ne} is expanded, and the two unknowns are combined into the single term $F[\rho_0]$, the ground state energy equation becomes:

$$E_0 = \int \rho_0(\mathbf{r})\upsilon(\mathbf{r})d\mathbf{r} + F[\rho_0] \qquad (2.16)$$

The second theorem shows that by using the variational principle the ground state energy of a system can be found by optimizing the electron density. The density that results in the lowest energy, is the ground state density.

$$E[\rho] \geq E[\rho_0] \tag{2.17}$$

The energy obtained by the trial density trial density ($E[\rho]$), is an upper bound to the true ground state energy ($E[\rho_0]$). Together, these theorems laid the foundation for the development of Density Functional Theory (DFT), that all observable quantities of a system can be determined from the electron density.

2.3.2 Kohn-Sham Density Functional Theory

Only the foundation of DFT was formed because theorems did not specify how to calculate E_0 from ρ_0, or how to calculate ρ_0 without first finding the wavefunction. In 1965, Kohn and Sham developed a method to solve these two issues.[71] Kohn-Sham (KS) DFT involves the creation of a fictitious reference system, where the electron density is equal to the real system. This reference system utilizes the method involved in HF theory, by being a system of non-interacting electrons where each electron experiences the same averaged potential. By using this reference system, $F[\rho_0]$ becomes:

$$F[\rho_0] = T_s[\rho] + V_s[\rho] + E_{xc}[\rho] \tag{2.18}$$

where the E_{xc} is the exchange-correlation energy functional. T_s and V_s are the kinetic and electron-electron repulsion of the non-interacting reference system.

$$T_s = -\frac{1}{2}\sum_{i=1}^{N}\int \psi_i^*(\mathbf{r})\nabla^2\psi_i(\mathbf{r}) \qquad V_s = \frac{1}{2}\iint \frac{\rho(\mathbf{r}_1)\rho(\mathbf{r}_2)}{r_{12}}d\mathbf{r}_1 d\mathbf{r}_2 \tag{2.19}$$

where V_s is the averaged electrostatic electron-electron repulsion used in HF theory. The equation for T_s can be related back to the density by:

$$\rho[r] = \sum_{i}^{N} \left|\psi_i(r)\right|^2 \tag{2.20}$$

The expanded representation for E_0 then becomes:

$$E_0 = \int \rho_0(\mathbf{r})\upsilon(\mathbf{r})d\mathbf{r} - \frac{1}{2}\sum_{i=1}^{N} \int \psi_i^*(\mathbf{r})\nabla^2\psi_i(\mathbf{r}) + \frac{1}{2}\iint \frac{\rho(\mathbf{r}_1)\rho(\mathbf{r}_2)}{r_{12}} d\mathbf{r}_1 d\mathbf{r}_2 + E_{xc}[\rho] \tag{2.21}$$

In effect, E_{xc} contains the differences in kinetic energy of the reference and real system, and the non-classical components of the electron-electron interaction. This is the key component in KS-DFT required for computing accurate molecular properties, so a good approximation is necessary.

2.3.3 Exchange-Correlation Approximations

There is a plethora of approximations for E_{xc}, with a wide range of classifications. The major classifications are local-density (LDA), generalized-gradient (GGA) and hybrid approximations. From here on, the term 'functional' will be used when talking about an approximation for E_{xc}. To aid in development of these functionals, E_{xc} is split into the sum of two parts:

$$E_{xc} = E_x + E_c \tag{2.22}$$

with E_x and E_c being the exchange-energy functional and correlation-energy functionals, respectively.

2.3.3.1 Local density approximation. The earliest approximation for E_{xc} is the local density approximation (LDA).[71] This method utilizes what is called the homogeneous electron gas (HEG) model, also known as jellium. It assumes that the density varies very slowly with position and can be treated as a uniform HEG. In this case, E_{xc} is the same at each point in the system as an HEG with the same density. LDA provides good results for things like metal Fermi surfaces and work functions, however, it tends to overestimate binding energies and vastly underestimates energy gaps in semiconductors.

2.3.3.2 Local spin-density approximation. For open-shell molecules and molecular systems close to dissociation, the local-spin-density approximation (LSDA) was developed, which is still based on the HEG model like LDA. It allows electrons of opposite spins to have different spatial KS orbitals. This is unlike LDA, where electrons of opposite spins have the same spatial KS orbital. This approximation deals with the electron density associated with the spin-α and spin-β electrons separately. This makes it so all functionals pertaining to the density, like E_{xc}, now have two quantities.

$$E_{xc} = E_{xc}\left[\rho^{\alpha}, \rho^{\beta}\right] \tag{2.23}$$

Where ρ^{α} and ρ^{β} represent the spin-α and spin-β densities, respectively. When all electrons are paired $\rho^{\alpha} = \rho^{\beta}$. LSDA can calculate several properties, such as molecular geometries, dipole moments, transition metal compounds and vibrational frequencies and with decent success. However, dissociation and atomization energies are still a problem and higher level functionals are necessary to get accurate results.

2.3.3.3 Generalized-gradient approximation. In reality, molecules do not have a slowly varying electron density, which is why LDA/LSDA tend to fail. The generalized-

gradient approximation (GGA) improved upon this, by changing the way the density is perceived.[72-73] It's similar to LSDA in that it accounts for spin-α and spin-β electrons separately, but it expands the expression for E_{xc} to account for the gradient of the density. The addition of a gradient brings a more accurate representation on the true non-homogeneous electron density, and was found to give accurate dissociation energies. Just like LDA/LSDA splits E_{xc} into E_x and E_c parts, GGA does the same. The GGA method also opened the door for customization of E_{xc}, by starting the development of different functionals. For example, in 1988 Becke developed a functional for E_x (B88):[74]

$$E_x^{B88} = E_x^{LSDA} - b \sum_{\sigma = \alpha,\beta} \int \frac{(\rho^\sigma)^{\frac{4}{3}} \chi_\sigma^2}{1 + 6b\chi_\sigma \sinh^{-1} \chi_\sigma} d\mathbf{r} \qquad (2.24)$$

where E_x^{LSDA} is the exchange energy using the LSDA method, and b is an empirical factor equal to 0.0042 atomic units.

Empirical factors are used for tuning the basic form of the functional to match the true experimental values. This is done by building a test set of atoms or molecules, then fitting their known energies. The use of empirical factors is a common practice when creating new E_{xc} functionals, however there are some that do not use them, such as the one from Perdew-Burke-Ernzerhof (PBE).[75] This is why GGA methods are sometimes referred to as gradient-corrected functionals, seeing as it is applying a correction to the E_x energy calculated using the LSDA method. Another common GGA functional is the Perdew-Wang 1986 functional (PW86),[76] which does not include any empirical factors. A similar treatment is done to E_c and many functionals have been developed, a popular one being from Lee-Yang-Parr (LYP).[77] Two terms, one being for E_x and another for E_c are combined to form the full E_{xc} expression. Any two terms can be combined, which opens up a plethora

of possibilities. For example, one can combine B88 for E_x, and LYP for E_c, to form the BLYP E_{xc} functional. This was a major advance in the development of DFT.

2.3.3.4 Hybrid functionals. Probably the most widely used expressions for E_{xc} used today are considered hybrid exchange-correlation functionals. The 'hybrid' moniker stems from the fact it combines both DFT and HF parameters into the calculation of E_{xc}. Even though HF theory doesn't properly account for electron correlation, it does involve an almost exact method for electron exchange. The HF exchange energy, labelled as E_x^{exact}, is given by:

$$E_x^{exact} \equiv -\frac{1}{4}\sum_{i=1}^{N}\sum_{j=1}^{N}\left\langle \theta_i^{KS}(1)\theta_j^{KS}(2)\left|\frac{1}{r_{12}}\right|\theta_j^{KS}(1)\theta_i^{KS}(2)\right\rangle \qquad (2.25)$$

which slightly differs from HF theory by replacing HF orbitals with KS orbitals.

A hybrid functional takes a fraction of this definition for E_x and combines it with DFT E_x and E_c approximations. A very popular one, B3LYP, includes the 3-empirical-parameter functional by Becke (B3) and the LYP correlation energy.[78] When all these are combined it leads to the following definition:

$$\begin{aligned} E_{xc}^{B3LYP} = (1 - a_0 - a_x)E_x^{LSDA} + a_0E_x^{exact} + a_xE_x^{B88} \\ + (1 - a_c)E_c^{VWN} + a_cE_c^{LYP} \end{aligned} \qquad (2.26)$$

where E_c^{VWN} is the correlation energy given by Vosko-Wilk-Nusair, which was originally devised for the LSDA method.[79] The empirical parameters a_0, a_x, and a_c are equal 0.20, 0.72 and 0.81, respectively.

The PBE GGA functional was recreated as a hybrid (PBE0), by mixing the PBE and E_x^{exact} energies in a 3 to 1 ratio.[80] For a case like this, it is sometimes referred to as a functional with 25% exact exchange. The benefit of using a non-empirical functional like

PBE or PBE0, is that it should perform universally, that is, it should provide accurate results for most every system. However, it systematically tends to overestimate the band gap energy of systems.

Another kind of hybrid functional is labelled a long-range corrected hybrid, which was first introduced by Savin in 1996 for the LDA exchange functional.[81] Long-range correction is done by partitioning the two-electron operator into short and long-range parts:

$$\frac{1}{r_{12}} = \frac{1 - \mathrm{erf}(\mu r_{12})}{r_{12}} + \frac{\mathrm{erf}(\mu r_{12})}{r_{12}} \tag{2.27}$$

where $r_{12} = |\mathbf{r}_1 - \mathbf{r}_2|$ for coordinate vectors of electrons $\mathbf{r}_1$ and $\mathbf{r}_2$, and μ is a parameter to determine the ratio between these parts. However, Savin's method only worked for LDA since GGA functionals did not usually have corresponding density matrices like LDA. This problem was solved in 2001 when Iikura et al. pushed the gradient terms into the momentum. This allowed the new long-range corrected functionals to reproduce the original GGA exchange functional when μ=0.

Two popular long-range corrected functionals are the CAM-B3LYP and ωB97x-D functionals.[82-84] CAM-B3LYP changes (2.27) to:

$$\frac{1}{r_{12}} = \frac{1 - [\alpha + \beta \cdot \mathrm{erf}(\mu r_{12})]}{r_{12}} + \frac{\alpha + \beta \cdot \mathrm{erf}(\mu r_{12})}{r_{12}} \tag{2.28}$$

where α and β equal 0.19 and 0.46, respectively. The ωB97x functional was the first long-range corrected semiempirical functional:[83]

$$E_{xc}^{\omega B97X} = E_x^{LC(LR)} + c_x E_x^{HF(SR)} + E_x^{B97(SR)} + E_c^{B97} \tag{2.29}$$

where LR and SR represent short and long-range corrections, respectively, and B97 represents the Becke 1997 semiempirical functional.[85] The ωB97x-D functional includes an added van der Waals atom-atom dispersion correction.[84]

Another method to take long-range interactions into account is the screened Coulomb potential functional developed by Heyd-Scuseria-Ernzerhof in 2003.[86] This functional, denoted as HSE, was created by dividing the exchange terms of PBE0 into short and long-range parts:

$$E_{xc}^{HSE} = aE_x^{exact,SR}(\omega) + (1 - a)E_x^{PBE,SR}(\omega) + E_x^{PBE,LR}(\omega) + E_c^{PBE} \qquad (2.30)$$

where ω is a mixing parameter which determines what is considered short and long-range interactions, and a is the parameter that determines the amount of exact exchange is used. One thing to note is that for the exact exchange integral, only the short-range component was included. For the HSE06 iteration of the functional, a=0.25 and ω is an adjustable parameter, typically between 0.1-0.2.[87] The HSE06 functional will also be used extensively in a future chapter.

2.3.4 Time-Dependent Density Functional Theory

For all the benefits that DFT provides, it only helps solve the time-independent Schrödinger equation. It wasn't until 1984 when Runge and Gross developed a time-dependent (TD) extension to KS-DFT.[88] The full derivation is in Ref. [88], but in the end the Runge-Gross theorem states two different time dependent external potentials cannot produce the same time dependent density. This is because the time dependent density is a unique functional of the time dependent external potential. In 1999, van Leeuwen proved this potential and legitimized the TD-KS scheme.[89] One maps the interacting system to a non-interacting one, described by a potential (V_{eff}) which would yield the same density as the interacting system. The TD form of the KS equations is:

$$i\frac{\delta}{\delta t}\phi_i(\mathbf{r},t) = \left(-\frac{1}{2}\nabla^2 + V_{eff}(\mathbf{r},t)\right)\phi_i(\mathbf{r},t) \qquad (2.30)$$

where

$$V_{eff}(\mathbf{r},t) = V_{ext}(\mathbf{r},t) + \int \frac{n(\mathbf{r}',t)}{|\mathbf{r}-\mathbf{r}'|} d\mathbf{r}' + V_{xc}(\mathbf{r},t) \tag{2.31}$$

where V_{ext} is the known external potential of the interacting system, the second term is the Hartree potential, and V_{xc} is the exchange correlation potential. The adiabatic local density approximation (ALDA) is often used for TDDFT,[90-92] in which V_{xc} is approximated as:

$$V_{xc}[\rho](\mathbf{r},t) \approx \frac{\delta E_{xc}[\rho_t]}{\delta \rho_t} = V_{xc}[\rho_t](\mathbf{r}) \tag{2.32}$$

Conveniently, the exchange-correlation functionals used for DFT can be used for TDDFT as well.

TDDFT is most commonly applied to the calculating the energies of excited states, which is based on linear response TDDFT (LR-TDDFT). This theory revolves around applying a small external perturbation that is not enough to destroy the ground state structure of the system, then measuring the response. This measurement yields information regarding the electronic structure of the system.

2.4 Marcus Theory

The field of electron transfer processes began to take off in the late 1940s following the end of the second World War. Before the war only slow electrochemical reactions could be studied, such as the release of the hydronium ion at an electrode to form hydrogen gas. After the war, radioactive isotopes became available, which allowed scientists to study isotopic exchange reactions such as:

$$Fe^{2+} + Fe^{*3+} \rightarrow Fe^{3+} + Fe^{*2+} \tag{2.33}$$

where the asterisk identifies the radioactive isotope in the reaction.

One hurdle scientists faced was that the current instrumentation was not capable of taking measurements at the time scale electron transfer reactions occur. The stopped flow apparatus, which was pioneered by Sutin for inorganic electron transfer reactions, overcame this hurdle.[93] It allowed one to study reactions on the millisecond time scale and was able to study electron transfer between different redox systems, termed "cross reactions," such as:

$$Fe^{2+} + Ce^{4+} \rightarrow Fe^{3+} + Ce^{3+} \qquad (2.34)$$

Throughout the years as instrumentation became more advanced, such as the development of laser spectroscopy, more complex electron transfer reactions started to be studied. In 1953 Henry Taube published the first work on "inner-sphere" electron transfer. He discovered during the following redox reaction:[94]

$$[CoCl(NH_3)_5]^{2+} + [Cr(H_2O)_6]^{2+} \rightarrow [Co(NH_3)_5(H_2O)]^{2+} + [CrCl(H_2O)_5]^{2+} \qquad (2.35)$$

that chlorine acts as a bridge between chromium and cobalt. During the lifetime of the bridged complex, chlorine will act as a channel of electron flow from Co(II) to Cr(III) and create the products Co(III) and Cr(II).

In the late 1950s, the only studied electron transfer reactions were "inner-sphere", but Rudolph Marcus developed a theory to explain the rates of "outer-sphere" electron transfer in 1956.[95] During an "outer-sphere" electron transfer event, the chemical species remain separate and intact throughout the entire reaction. This is opposed to the "inner-sphere" reaction mentioned earlier which involves a chemical bridge forming between two redox sites, in which Marcus extended his theory for a few years later.[93]

The initial hurdle Marcus had to overcome was that according to transition state theory there is an energy of activation to a transition state, which doesn't exist during an

outer-sphere electron transfer reaction. Some basic principles used to postulate Marcus' "outer-sphere" theory were: (i) when an electron is transferred it does not change in energy, (ii) the potential energies for the molecules are represented by the harmonic oscillator, and (iii) the nuclei are thought as stationary since electron transfer happens at a much faster rate than nuclear motion. Using the quadratic relationships between parabolas Marcus derived a relationship to solve for the energy of activation as:[96]

$$\Delta G^{\ddagger} = \frac{(\Delta G + \lambda)^2}{4\lambda} \tag{2.36}$$

where $\Delta G^{\ddagger}$ is the energy of activation, ΔG is the free energy change of the reaction and λ is the reorganization energy. These can be visualized in Figure 2.1. The Marcus theory rates were calculated using this relationship alongside the Eyring equation shown below.[97]

$$k = \kappa A \sigma^2 e^{\left(\frac{-\Delta G^{\ddagger}}{k_B T}\right)} \tag{2.37}$$

In this representation κ represents the averaged transition probability for electron transfer, and $A\sigma^2$ contains dimensions for collision frequency, with σ being the average center-to-center distance between donor and acceptor. These early studies treated the motion of nuclei classically and focused on systems with weak electronic coupling (V_{AB}) between each other. In other words, this rate law represents a diabatic state where V_{AB} is small, however, for an adiabatic state, V_{AB} is large and must be taken into account. This leads to a new first-order electron transfer rate law:

$$k = \frac{2\pi}{\hbar} V_{AB}{}^2 (FC) \tag{2.38}$$

with FC being the Franck-Condon factor. This factor is the vibrational overlap integral between the reactants and products. For treatment of nuclear motion, there are two theories that are typically used: (i) use the harmonic or Morse oscillator for inner-shell coordinates

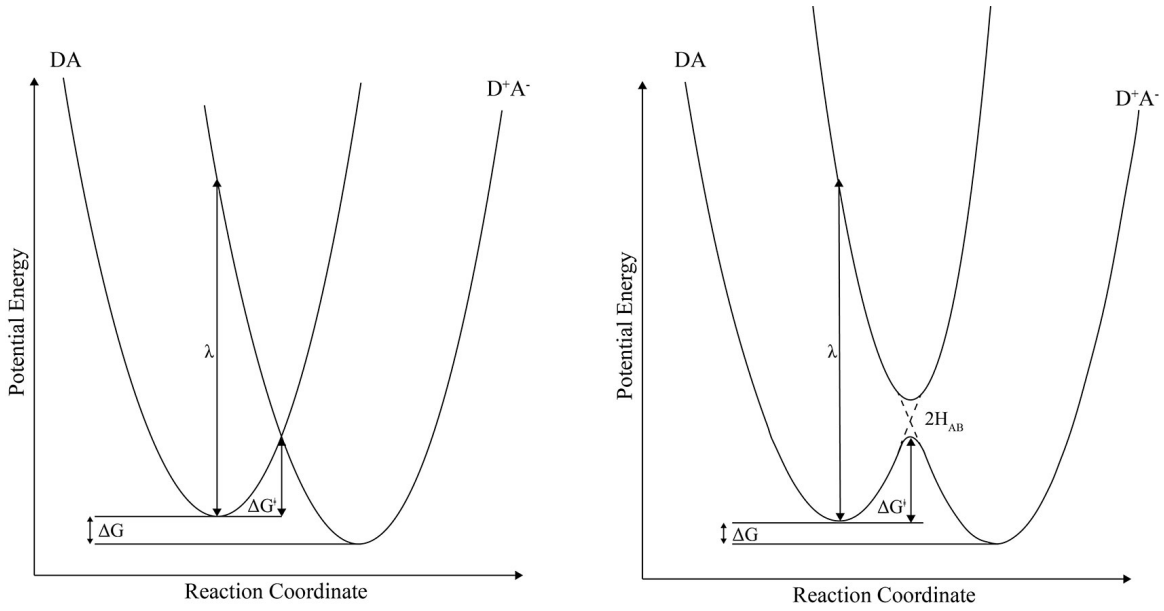

Figure 2.1. Visualization of the Marcus parameters for a) diabatic and b) adiabatic states

and treat motion of the solvent using classical methods or (ii) assume all coordinates as independent oscillators. The latter method has shown to be inadequate for systems with a large entropy of reaction because the rate relies on the enthalpy of reaction. Method (i), however, uses the free energy of reaction instead of the enthalpy, and is therefore unaffected by large entropies. In the high-temperature limit, the rate becomes:

$$k = \frac{2\pi}{\hbar} |V_{AB}|^2 \frac{1}{\sqrt{4\pi\lambda RT}} e^{\left(-\frac{(\Delta G + \lambda)^2}{4\lambda RT}\right)} \tag{2.39}$$

where λ is the summation of the inner and outer reorganization energies and T is the temperature. This can be reorganized as:

$$k = \sqrt{\frac{4\pi^3}{h^2 \lambda k_b T}} |V_{AB}|^2 e^{\left(-\frac{(\Delta G + \lambda)^2}{4\lambda k_b T}\right)} \tag{2.40}$$

when breaking up $\hbar$ and R, which is how the Marcus rate equation is typically written.

Even though the general consensus is that the reaction rate increases as ΔG becomes more negative, this is not always the case in Marcus theory. Marcus postulated that when $|\Delta G| > \lambda$ the rate will begin to decrease and was thusly named the inverted region. This region was not observed until 1984, in which Miller and Closs tested the intramolecular electron transfer rate between a donor and acceptor separated by a long carbon framework.[98] They discovered there was a tipping point, that once ΔG kept decreasing past a certain value, the rate started to exponentially decrease.

CHAPTER THREE

Electronic Effects on a D-π-A Organic Sensitizer Upon Heteroatom Substitutions in the π-Bridge

Portions of this chapter are published as: Smith, A. G.; Shuford, K. L., Electronic effects on a D-π-A organic sensitizer upon heteroatom substitutions in the π-bridge. *Journal of Photochemistry and Photobiology A: Chemistry* **2017,** *332*, 580-585.

3.1 Abstract

Organic donor-pi-acceptor sensitizers are a promising path to achieving cheaper and more efficient dye sensitized solar cells. The π-bridge plays an important part in the photovoltaic properties of the dye, and sulfur systems, like thiophene, have been favorites for this role. We aim to investigate the change in photovoltaic properties for systems that utilize heteroatoms besides sulfur. Using density functional theory, we have investigated the spectroscopic and electronic properties of the D5 organic dye upon heteroatom substitution for sulfur in the π-bridge. We substituted for sulfur with pnictogens, chalcogens, and various other elements in the second row of the periodic table. We find the larger elements reduce the HOMO-LUMO gap, red shift the absorption spectrum, increase the dipole moment and are energetically favorable for electron injection. Dyes were adsorbed onto a $(TiO_2)_{16}$ surface and found favorable electron injections for all substituted systems except boron. In particular, π-bridge systems utilizing selenium or phosphorus, instead of the more prevalent sulfur, could prove to be more efficient based on our analysis of photovoltaic properties.

3.2 Introduction

With growing energy demand, the need for sources other than fossil fuels has been brought into focus. In particular, the conversion of solar energy has gained momentum as a technology that could meet this increase in demand.[99-100] Dye-sensitized solar cells (DSSCs), introduced by O'Regan and Gratzel in 1991,[101] have shown great promise as next-generation photovoltaics. Ru(II)-based dyes have a power conversion efficiency of approximately 11%.[102] However, ruthenium is a rare metal, so widespread application will prove difficult. Alternatively, organic sensitizers possess a number of attractive attributes, most notably cost and availability of raw materials.[103] The leading organic sensitizers utilize the donor-pi-acceptor (D-π-A) framework.[104-106] In this structure, electron donor and acceptor groups are connected by a π-conjugated bridge. The acceptor is linked to the semiconductor surface, typically TiO_2, by a carboxylic acid.

When examining a potential sensitizer, multiple factors must be considered. The lowest unoccupied molecular orbital (LUMO) must lie above the semiconductor conduction band (CB) so it is energetically favorable for the excited electrons to inject into the surface.[107] The highest occupied molecular orbital (HOMO) energy level must lie below the electrolyte redox potential, allowing the dye to gain back the lost electron.[101] Other factors include the presence of an anchor group to bond with the semiconductor,[108-109] directed charge transfer from the sensitizer to the semiconductor, and having a high molar extinction coefficient.[110] The latter implies less of the compound is needed in the cell to obtain the same power input, which could lead to thinner and more efficient cells.[111] More fully utilizing the entire solar spectrum is also highly desirable. Most sensitizers absorb in the ultraviolet or the shorter wavelengths of the visible light range. Therefore,

concurrently accessing longer wavelengths may lead to significant improvements in efficiency.

One D-π-A framework utilizes a triphenylamine donor group, a thiophene π-bridge, and a cyanoacryllic acid acceptor, with excitation involving a charge transfer from the donor to acceptor group. The chemical structure of the dye is shown in Figure 3.1, along with its HOMO and LUMO orbitals. This dye, known as D5, was synthesized

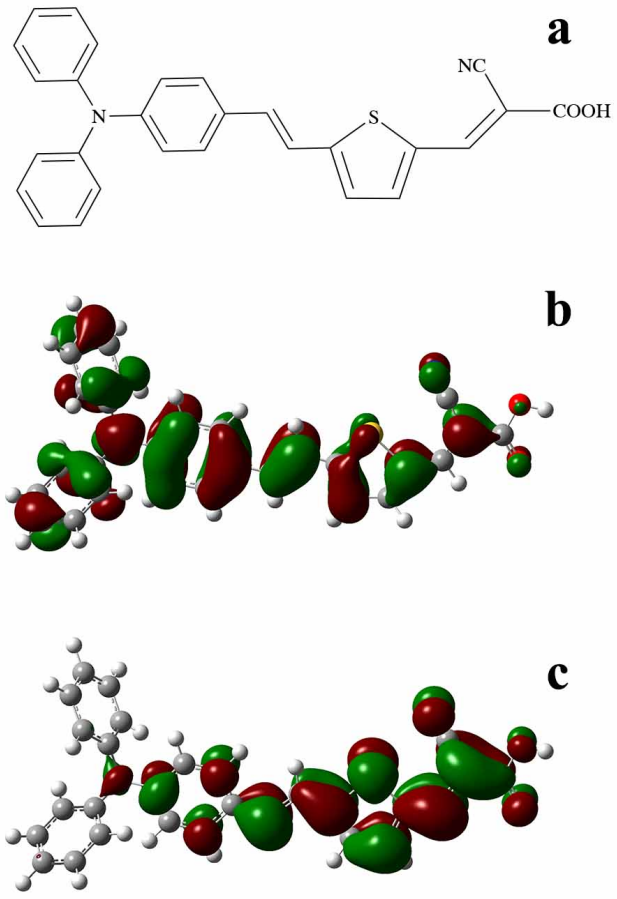

Figure 3.1. a) Chemical structure of the D5 solar dye and its b) HOMO and c) LUMO orbitals

in 2006 and showed promise as an organic sensitizer.[112-113] Since then, many studies on D-π-A dyes have focused on optimization of the donor and acceptor groups,[27, 114] while the

π-bridge portion has received less attention. The π-bridge is very influential to the dynamics of electron transfer within the sensitizer and, if optimized, could increase the efficiency of intramolecular electron transfer.

This study utilizes a theoretical approach to examine potential π-bridge systems, ultimately aimed at improving the properties of D-π-A sensitizers for photovoltaic applications. Using elements from the second row of the periodic table, along with pnictogens and chalcogens up to the fourth row, we have investigated how changing the heteroatom of the π-bridge ring affects the spectroscopic and photovoltaic properties of the dye. D5 was chosen for this study because it is a relatively simple dye with only a single heteroatom in the π-bridge, so the effects of elemental substitution can be analyzed in a straightforward manner. We find these simple atomic substitutions can have interesting effects on the electronics of the D-π-A dye, which may prove beneficial toward development of new molecules for DSSCs.

3.3 Methods

A standard exchange-correlation functional used by density functional theory tends to underestimate the excitation energies for charge transfer of molecules, with the error increasing as the overlap between orbitals decreases. This poses a problem when investigating D-π-A dyes due to the donor and acceptor portions being separated spatially by the π–bridge, which leaves little overlap of the HOMO and LUMO orbitals. Using a hybrid functional reduces the error by including Hartree-Fock exchange, and when using a functional with long-range corrections, the errors are decreased even further.[115] We have examined several different functionals to determine which is most suitable to describe the excitations in the D5 dye variants being studied here. All ground state geometries were

optimized by DFT using the B3LYP functional and the 6-31G(d) basis set. Diffuse functions were not added for they have negligible effects on the electron density in these molecules and are computationally more expensive.[116] Electronic absorption spectra and excitation energies were calculated using several DFT functionals including B3LYP, HSE06, PBE0, ωB97xD, CAM-B3LYP, and M06-HF. For calculations in solution, the SMD model was used, which has been shown to produce accurate results for organic dyes.[117-118] All calculations were done using the Gaussian09 software package.[119]

The total sunlight-to-electricity conversion efficiency (η) is an important parameter to evaluate the performance of a DSSC, and is related to the fill factor (FF), open-circuit voltage (V_{OC}), incident solar power (P_{inc}), and short-circuit density (J_{SC}) via:

$$\eta = FF\frac{V_{OC}J_{SC}}{P_{inc}} \tag{3.1}$$

By increasing the V_{OC} and J_{SC}, we can enhance the total conversion efficiency. A number of factors contribute to V_{OC}, such as the conduction band edge of the semiconductor, the reduction-oxidation potential of the electrolyte, and the density of accessible states in the conduction band; however, Ruhle et al. observed that V_{OC} was linearly dependent on the dipole moment of the dye in the ground state,[120] which is what we will consider here. The J_{SC} value is associated with the light absorption capability and the electron injection efficiency from the dye to the semiconductor. For DSSCs, J_{SC} is determined by the equation:[121]

$$J_{SC} = \int LHE(\lambda)\Phi_{inject}\eta_{collect}d\lambda \tag{3.2}$$

where LHE(λ) is the light harvesting efficiency, $\eta_{collect}$ is the charge collection efficiency, and Φ_{inject} is the electron injection efficiency. For calculations in which the dye is being changed only moderately, and not the surface the dye will be attached to, $\eta_{collect}$ can be

presumed the same for each molecule. Based on Beer's law the LHE can be approximated with the following equation

$$LHE = 1 - 10^{-f} \quad (3.3)$$

where f is the oscillator strength. The Φ_{inject} value is related to the driving force (ΔG^{inject}) of injection from dye to the semiconductor. Electron injection occurs very rapidly in these systems, and there has been experimental evidence that the electron transfer event occurs much faster than the vibrational relaxation of the dye.[122-124] Therefore, the charge transfer can be assumed to take place from an unrelaxed excited state, and ΔG^{inject} can be estimated by:[125-126]

$$\Delta G^{inject} = E^{dye*} - E_{CB} = E^{dye} - E_{EX} - E_{CB} \quad (3.4)$$

where E^{dye*} is the oxidation potential of the dye in the excited state, E_{CB} is the reduction potential of the conduction band edge for the semiconductor, E^{dye} is the redox potential of the dye in the ground state ($-E_{HOMO} = E^{dye}$), and E_{EX} is the excitation energy for the transition associated with the intramolecular charge transfer. Obtaining a correct value of E_{CB} is difficult since it is sensitive to experimental conditions. For TiO_2, E_{CB} has been shown to equal 4.00 eV,[125, 127] which will be used for this study.

We will be reporting λ_{max}, LHE, ΔG^{inject}, and μ of the dye after each π-bridge variation has been substituted. The sun's radiation output peaks at approximately 500 nm and is skewed toward longer wavelengths, so red-shifting the spectra is often beneficial for increasing the dye efficiency. Regarding J_{SC}, the goal is to increase the λ_{max} without sacrificing the LHE, and to maintain a favorable ΔG^{inject}. For the V_{OC}, we will be observing the change in the dipole moment after each substitution in hopes of enhancing V_{OC} alongside J_{SC}. We will use these values as an indicator to determine if a variation would increase or decrease the overall efficiency η.

3.4 Results and Discussion

3.4.1. Establishing Benchmarks

For benchmarking purposes, six functionals have been tested, where we compared the calculated λ_{max} to experiment (Table 3.1). B3LYP, PBE0 and HSE06 are all hybrid

Table 3.1. TD-DFT functional test of D5 dye in gas phase and ethanol solution. The table shows the maximum absorption wavelength (λmax), oscillator strength (*f*), and the difference between the calculated and experimental λmax (Δλ).

	Gas Phase		Ethanol		
Functional	λmax (nm)	*f*	λmax (nm)	*f*	Δλ (nm)
Experiment	-	-	441	-	-
B3LYP	534.5	1.11	594.0	1.25	153.0
HSE06	543.9	1.02	604.4	1.17	163.4
PBE0	510.2	1.24	562.1	1.37	121.1
ωB97xD	422.2	1.74	465.0	1.83	24.0
CAM-B3LYP	433.4	1.69	466.5	1.79	25.5
M06-HF	386.5	1.72	409.6	1.80	-31.4

functionals, while ωB97xD, CAM-B3LYP and M06-HF are long-range corrected DFT hybrids. The experimentally measured λ_{max} of the D5 dye in ethanol is 441 nm and the experimental spectrum is shown in Figure 3.2.[112] The hybrid functionals perform poorly in ethanol, being off from the experimental λ_{max} by over 120 nm when in solution (similar trends are present in gas phase; all peaks are red-shifted when accounting for solvation effects). The long-range corrected functionals predict λ_{max} to be much closer to experiment. M06-HF produces acceptable results when paired with a solvation model, only being off the experimental value by 31.4 nm. The best functional in ethanol using the SMD solvation model is ωB97xD, which predicts λ_{max} to be 24.0 nm from the experimental value. Based on these findings, the combination of ωB97xD and SMD will be used for further TD-DFT

calculations. Additionally, this functional has been shown to produce accurate results for the spectroscopic properties of D-π-A dyes.[118, 128]

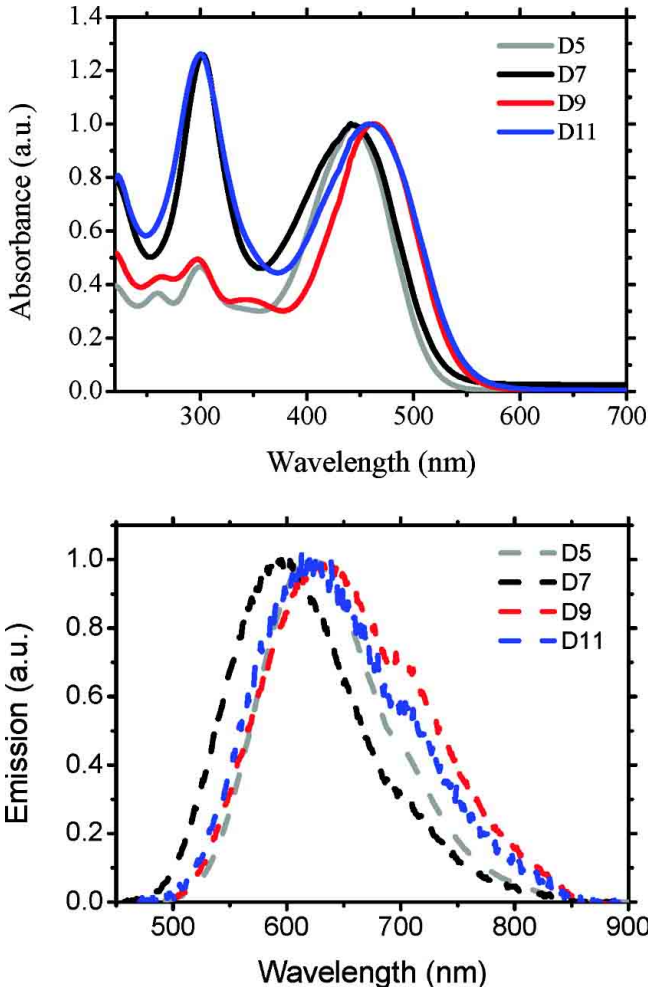

Figure 3.2. Experimental spectrum of the D5 dye in ethanol solution. Reprinted (adapted) with permission from D.P. Hagberg, J.-H. Yum, H. Lee, F. De Angelis, T. Marinado, K.M. Karlsson, R. Humphry-Baker, L. Sun, A. Hagfeldt, M. Grätzel, M.K. Nazeeruddin, Molecular Engineering of Organic Sensitizers for Dye-Sensitized Solar Cell Applications, Journal of the American Chemical Society, 130 (2008) 6259-6266. Copyright (2008) American Chemical Society.

3.4.2. Energy Levels After Substitution

Many studies have previously described the effects of altering the donor or acceptor portions of these sensitizers.[102-103, 114, 129] However, the π-bridge also plays an important

role in the overall D-π-A system, and over the last few years, more papers have focused on modifying that region of the molecule.[130-133] These accounts have substituted various conjugated groups into the π-bridge but have not investigated the effect of heteroatom substitution. For the D5 dye, a thiophene group is used as the π linker between the triphenylamine donor group and the cyanoacryllic acid acceptor (Fig. 3.1a). Instead of thiophene, here we substituted different heteroatoms for the sulfur. All heteroaromatic rings were kept as 5-membered to most closely mimic thiophene, and hydrogen was added to the heteroatom as necessary to fill the valence. This method maintains consistency in the length and rigidity between heterocycles; changes observed can be interpreted as effects of the heteroatom substitution primarily.

As shown in Table 3.2, upon heteroatom substitution the HOMO energy levels stay below the electrolyte reduction potential for I_3/I^- of -4.6 eV in vacuum[134] and -4.8 eV in ethanol,[114] verifying the dye can still regenerate the ground state and complete the circuit

Table 3.2. HOMO and LUMO energy levels of heteroatom substituted dyes with Δ_{H-L} denoting the energy gap between the HOMO and LUMO.

Dye	Gas			Ethanol		
	HOMO (eV)	LUMO (eV)	Δ_{H-L} (eV)	HOMO (eV)	LUMO (eV)	Δ_{H-L} (eV)
B	-5.07	-3.43	1.64	-4.92	-3.35	1.57
C	-5.02	-2.62	2.40	-4.86	-2.60	2.27
N	-5.00	-2.33	2.67	-4.87	-2.30	2.56
O	-5.06	-2.50	2.56	-4.93	-2.53	2.40
P	-5.09	-2.76	2.33	-4.92	-2.75	2.17
S	-5.11	-2.62	2.48	-4.94	-2.64	2.30
As	-5.09	-2.79	2.31	-4.90	-2.73	2.17
Se	-5.10	-2.65	2.45	-4.92	-2.63	2.29

of the cell. The LUMO is most affected by the substitutions, due to the substitution occurring closer to the acceptor region of the dye. It is important to note that all LUMO energy levels are above the TiO_2 conduction band of -4.00 eV;[127] therefore, electron injection into TiO_2 remains favorable throughout the substitutions.

Using the Pauling Electronegativity Scale,[135-136] a general trend is observed that as the electronegativity of the heteroatom increases, the energy gap also increases. This trend can be observed graphically in Figure 3.3, and the tabular data is in Table 3.3. In ethanol, the pnictogens follow this trend with nitrogen having the largest gap of 2.56 eV

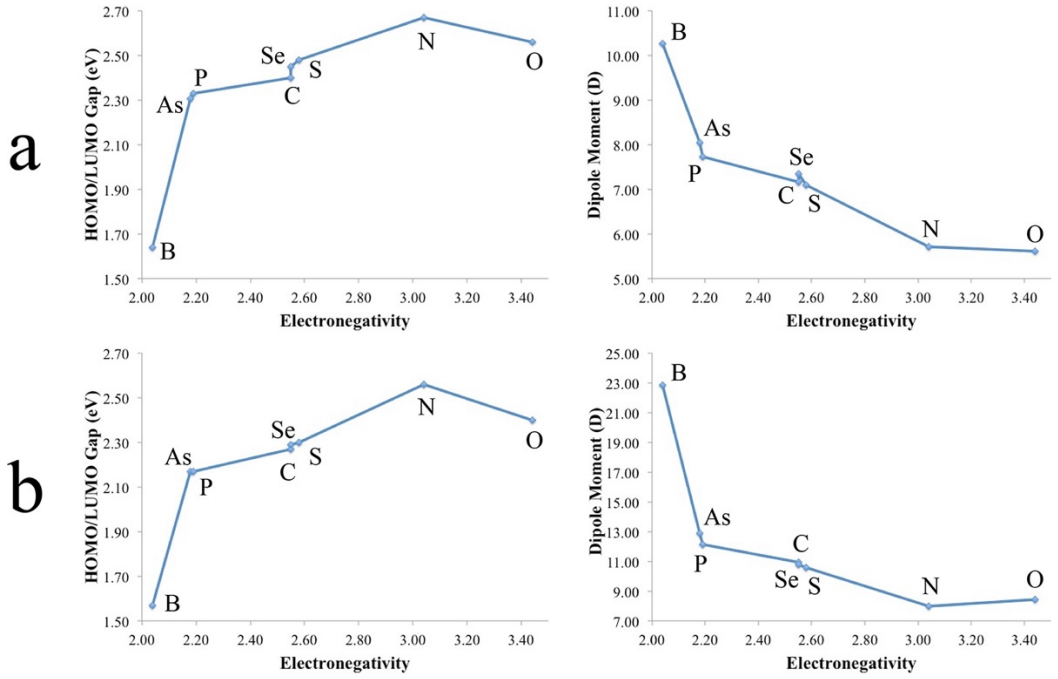

Figure 3.3. The HOMO/LUMO energy gap and dipole moment of each species plotted against the electronegativity of each substituted heteroatom in a) gas and b) ethanol solution.

and arsenic with the smallest at 2.17 eV. The chalcogens follow this trend as well, with the energy gap being the largest for oxygen at 2.40 eV and the smallest for selenium at 2.29 eV. However, when going along the second row of the periodic table nitrogen breaks the

trend. Boron has the smallest of 1.57 eV and oxygen had a gap of 2.40 eV, but nitrogen is 0.16 eV higher than oxygen. This deviation is most likely caused by the strong polar interaction between hydrogen and nitrogen (Figure 3.4). Unlike with carbon, boron or

Table 3.3. Electronegativity of each heteroatom with the corresponding HOMO/LUMO gap and dipole moment of each species. Electronegativity determined using the Pauling Scale.

		Gas Phase		Ethanol	
Dye	Electronegativity	Δ_{H-L} (eV)	μ (D)	Δ_{H-L} (eV)	μ (D)
B	2.04	1.64	10.27	1.57	22.83
As	2.18	2.31	8.05	2.17	12.87
P	2.19	2.33	7.73	2.17	12.12
C	2.55	2.40	7.16	2.27	10.92
Se	2.55	2.45	7.35	2.29	10.79
S	2.58	2.48	7.09	2.30	10.58
N	3.04	2.67	5.72	2.56	7.98
O	3.44	2.56	5.61	2.40	8.43

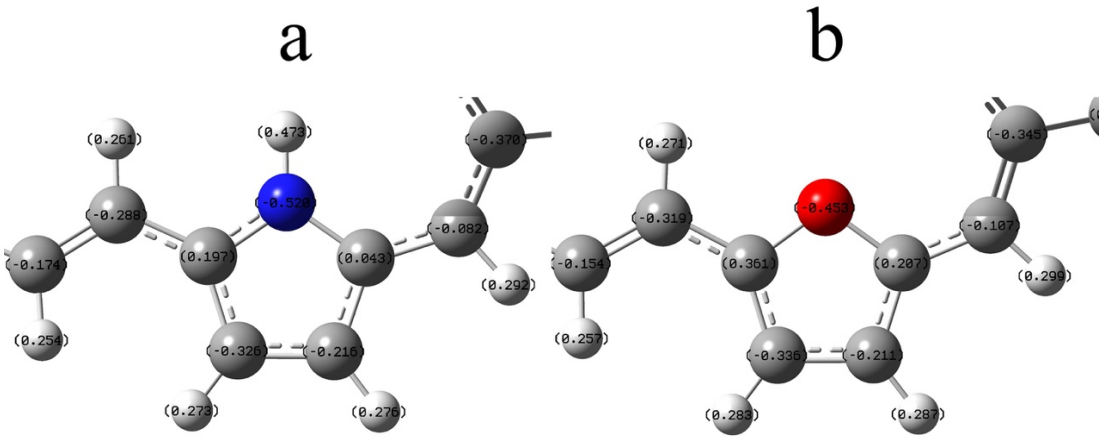

Figure 3.4. NBO charge analysis of the π-bridge after nitrogen and oxygen substitutions. Nitrogen has a negative charge of -0.520, while oxygen has a charge of -0.453.

phosphorus, when hydrogen is attached to nitrogen to fill the valence, the larger bond polarity contributes more to the charge on the heteroatom. This leads to a higher electron density around nitrogen than oxygen and increases the energy gap of that dye.

3.4.3. Absorption Spectra

Figure 3.5 displays the computed absorption spectra for all the D-π-A dyes in ethanol and gas phase. Our calculations show the same general appearance as the D5 experimental spectrum (Figure 3.2)[112] including some weak excitations at less than ~350 nm and a large peak red-shifted from these features. The most intense peak in the spectra (430 - 520 nm) corresponds primarily to transitions from HOMO to LUMO (Table 3.4). These excitations would be effective at moving electron density from donor to acceptor regions of the molecules. It can be noted that the third and fourth row elements exhibit wider, more red-shifted bands. The most unique spectrum is from the boron substitution, which has the smallest HOMO-LUMO gap. We see a broad peak at 942.5 nm, an intense peak at 446.0 nm, and another absorption at 337.4 nm. All other heteroaromatic substitutions did not have any peaks above ~520 nm, while the substitution of boron red-shifted the spectrum by a substantial amount. In this case, the broad feature at 942.5 nm is dominated by the HOMO to LUMO transition (Table 3.4). This broad peak is attributed to a delocalized density near B in the LUMO, and a diffuse transition moment from HOMO to LUMO. The energy gap for the boron species is the smallest among the tested dyes by 0.70 eV.

Although the spectral intensities for the B substituted ring are generally not as strong as the other dyes, there are two transitions that bring electrons to the acceptor portion of the dye. However, the longer wavelength feature has a notably decreased LHE compared

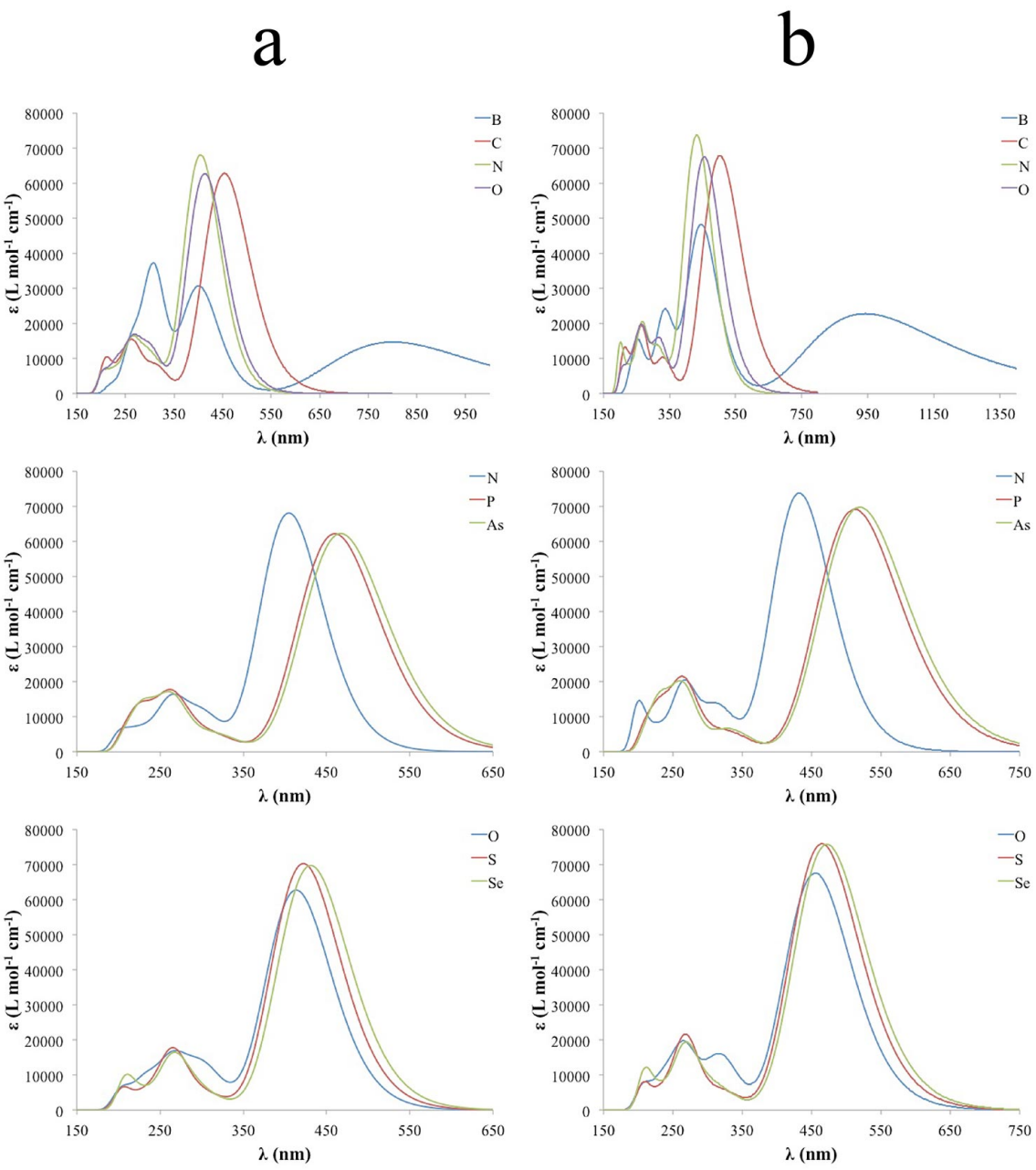

Figure 3.5. UV/Vis spectrum of the dye in a) gas and b) ethanol upon heteroatom substitutions of elements from row 2 of the periodic table, the pnictogens, and the chalcogens.

to other HOMO to LUMO transitions in the dyes (0.73 vs. ~0.98), and there is a dramatic dip in the AM1.5 solar spectral irradiance at ~950 nm. So while this spectral feature of the dye may ultimately be beneficial for harnessing NIR photons, we will concentrate on the global λ_{max} trends in the forthcoming analysis. This is reasonable because the boron peak

Table 3.4. The calculated absorption wavelength (λ_{max}), light harvesting efficiency (LHE), and the corresponding electronic transitions for each heteroatom substitution in ethanol. H = HOMO and L = LUMO.

Dye	λ_{max} (nm)	LHE	Assignment
B	942.5	0.726	H → L(80.4%) H-1 → L(12.9%) H-1 → L+2(2.6%)
	446.0	0.935	H-1 → L(58.9%) H → L(12.7%) H-2 → L(8.7%) H → L+1(4.9%) H → L+2(4.6%) H-1 → L+1(3.6%) H-9 → L(2.0%)
C	502.4	0.979	H → L(79.5%) H-1 → L(14.6%)
N	432.3	0.985	H → L(74.2%) H-1 → L(17.7%) H → L+1(3.3%)
O	455.2	0.979	H → L(74.7%) H-1 → L(17.5%) H → L+1(3.7%)
P	512.2	0.980	H → L(76.9%) H-1 → L(16.9%)
S	465.0	0.987	H → L(74.1%) H-1 → L(17.9%) H → L+1(3.8%)
As	519.6	0.981	H → L(78.8%) H-1 → L(15.15%)
Se	472.1	0.987	H-1 → L(17.8%) H → L+1(3.2%) H → L(74.7%)

at 446.0 nm gives a LHE of 0.935, which is comparable to the other substitutions and is only slightly blue-shifted from the original dye. Similarly, the transition at 446.0 nm puts electrons primarily in the LUMO and LUMO+1 like the others (Table 3.4), and these orbitals are also localized near the acceptor group of the dye (Figure 3.6). The HOMO for the boron species is more centralized in the pi-bridge than the donor portion of the dye, while the HOMO-1 has more density on the donor group phenyl rings. Compared to the transition at 942.5 nm, the band at 446.0 nm more closely represents the typical donor to

acceptor intramolecular charge transfer as seen in the other dyes in this study. Therefore, photovoltaic data obtained from the transition at 446.0 nm for the B species will be used to

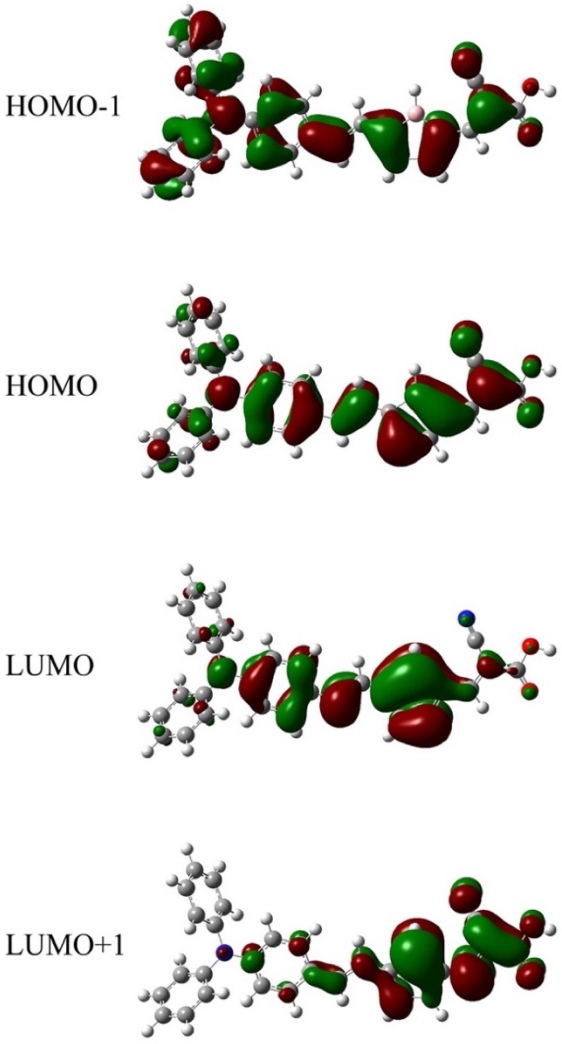

Figure 3.6. Molecular orbitals of boron substituted dye. The transition at 942.5nm involves localization of electrons in the LUMO, while the transition at 446.0nm localizes electrons primarily in the LUMO and LUMO+1.

compare with the other heteroatom substitutions. From this absorption data, we can now calculate other photovoltaic properties for each dye, based on the most intense spectral feature at ~500 nm.

3.4.4 Photovoltaic Data

Our approach toward predicting the photovoltaic performance of these dye molecules is to maximize the conversion efficiency, η, via increases in V_{OC} and J_{SC} (Eq. 1). For this analysis, the dipole moment will be used to represent relative variations in V_{OC}, and the combination of large LHE and large free energy of injection represents enhancements in J_{SC} at a given wavelength. As shown in Tables 3.5 and 3.6 (and Figure 3.3), we observe that as the electronegativity of the substituted heteroatom increases, by moving across a row or down a column of the periodic table, the dipole moment decreases. This varies slightly for oxygen in the ethanol solution (Table 3.6), by having a dipole moment 0.45 D higher than nitrogen. Being in close proximity to the acceptor region, the character of the heteroatom can notably alter the charge distribution of the dye. As the atom becomes more electronegative, it will hedge electron density migrating to the carboxylic group in the acceptor region of the dye by localizing electrons around itself, and thus decrease the dipole moment. The least electronegative heteroatom, boron, provides the largest dipole moment for the dye. Other substitutions decrease the dipole moment of the dye in accordance with atomic electronegativity trends (the O and N ordering is inverted as discussed above but they have comparable values). Therefore, a relative increase in V_{OC} is expected as the electronegativity of the heteroatom decreases.

Moving on to LHE and ΔG^{inject}, we observe more diffuse trends when going along the second row of the periodic table. The driving force generally increases from left to right, and λ_{max} fluctuates between 432 to 502 nm. LHE values are comparable for all except the B species (discussed previously). Table 3.5 shows clearer trends when moving down the chalcogens that suggest the dye properties become more favorable for photovoltaic

systems. λ_{max} red shifts and LHE as well as μ increase, while ΔG^{inject} decreases in magnitude slightly but still remains very favorable. The pnictogens follow a similar trend

Table 3.5. Calculated properties of heteroatom substituted dyes in gas phase. This includes the excitation energy (E_{EX}), oscillator strength (*f*), redox potential of the dye in the ground state (E^{dye}), driving force of injection (ΔG^{inject}), light harvesting efficiency at λ_{max} (LHE), maximum absorption wavelength (λ_{max}), and the dipole moment perpendicular to the semiconductor (μ).

Dye	E_{EX} (nm)	*f*	E^{dye} (eV)	ΔG^{inject} (eV)	LHE	λ_{max} (nm)	μ (D)
			Row 2				
B	3.09	0.75	5.07	-2.02	0.823	401.6	10.27
C	2.73	1.55	5.02	-1.71	0.972	453.8	7.16
N	3.06	1.68	5.00	-2.06	0.979	404.8	5.72
O	2.39	1.55	5.06	-1.33	0.972	413.5	5.61
			Chalcogen				
O	2.39	0.99	5.06	-1.33	0.898	519.3	5.61
S	2.94	1.74	5.11	-1.83	0.982	422.2	7.09
Se	2.88	1.50	5.10	-1.78	0.968	431.0	7.35
			Pnictogen				
N	3.06	1.68	5.00	-2.06	0.979	404.8	5.72
P	2.70	1.54	5.09	-1.60	0.971	460.0	7.73
As	2.65	1.54	5.09	-1.56	0.971	467.1	8.05

as the chalcogens, except the LHE value generally decreases moving down the column from N. However, there is a larger difference in the properties between the second and third row pnictogens when compared to the chalcogens, which can be attributed to the factors yielding the large band gap for the nitrogen species. Of all the elements being substituted that utilize additional hydrogens to fill valences, nitrogen forms the most polar bond with hydrogen, making it an electron density donor to nitrogen. The intramolecular effects of the polar bond in the π-bridge, coupled with enhanced solvent interactions, are likely the

origin of the differences in the spectroscopic and photovoltaic properties of the nitrogen species. For the fourth row elements, Natural Bond Order (NBO) analysis revealed that the d_{xy} electrons of the fourth row heteroatom, the d-orbital in the plane of the molecule, delocalize throughout the π-bridge system, thus increasing the ease of electron transfer through the π-bridge.

Table 3.6. Calculated properties of heteroatom substituted dyes in ethanol solution. This includes the excitation energy (E_{EX}), oscillator strength (*f*), redox potential of the dye in the ground state (E^{dye}), driving force of injection (ΔG^{inject}), light harvesting efficiency at λ_{max} (LHE), maximum absorption wavelength (λ_{max}), and the dipole moment perpendicular to the semiconductor (μ).

Dye	E_{EX} (nm)	*f*	E^{dye} (eV)	ΔG^{inject} (eV)	LHE	λ_{max} (nm)	μ (D)
			Row 2				
B	2.78	1.19	4.92	-0.40	0.935	446.0	22.83
C	2.47	1.68	4.86	-1.60	0.979	502.4	10.92
N	2.87	1.82	4.87	-2.00	0.985	432.3	7.98
O	2.72	1.67	4.93	-1.79	0.979	455.2	8.43
			Chalcogen				
O	2.72	1.67	4.93	-1.79	0.979	455.2	8.43
S	2.67	1.88	4.94	-1.72	0.987	465.0	10.58
Se	2.63	1.87	4.92	-1.71	0.987	472.1	10.79
			Pnictogen				
N	2.87	1.82	4.87	-2.00	0.985	432.3	7.98
P	2.42	1.71	4.92	-1.50	0.980	512.2	12.12
As	2.39	1.72	4.90	-1.49	0.981	519.6	12.87

This study has demonstrated that substituting other elements into the π-bridge of these D-π-A organic sensitizers can substantially change the photovoltaic properties. When comparing the effects from these substitutions, a number of factors should be considered in the overall assessment. For example, even though the boron species has the largest μ, it

has the smallest ΔG^{inject} and LHE, which would lead to the smallest J_{SC} of the dyes tested. Most of the factors that affect V_{OC} are tied to the surface properties and the redox electrolyte, while J_{SC} is a better measure of dye contributions and is weighted more heavily here. Nitrogen has the most favorable ΔG^{inject}, but the smallest dipole moment and λ_{max} values. Selenium could be a potentially better suited heteroatom than sulfur due to it having a slightly more red-shifted λ_{max} and a larger dipole, without sacrificing its LHE or injection driving force. If looking for a more abundant heteroatom, phosphorus is attractive due to it being the most red-shifted and having a large dipole moment, while the LHE is only slightly smaller compared to sulfur. Larger substituted heteroatoms had, on average, better photovoltaic properties and our results show introducing these heavier, less electronegative, heteroatoms into the π-bridge could improve photovoltaic efficiencies. Utilizing π-bridge systems with multiple heteroatoms could also yield interesting results.

3.4.5 Dyes on TiO_2 Surface

Once a dye is adsorbed to a surface the orbital densities and their locations will change. In order to confirm if electron injection occurs, each of the studied dyes were adsorbed to a $(TiO_2)_{16}$ surface. Smaller TiO_2 systems have been shown to be large enough to model electron injection, so we are comfortable with this TiO_2 size.[137-140] All of the surface calculations were done in the gas phase to reduce computation time.

A method commonly used to model if electron injection will occur is to adsorb a dye to the surface and inspect the HOMO and LUMO orbitals of the neutral ground state system. However, once an electron is moved, the wavefunction will change, and therefore, the molecular orbitals will slightly change, so this method is not depicting an accurate picture for electron injection. It has recently been found that by optimizing the reduced

system and inspecting the spin density difference between alpha and beta electrons, a more accurate representation of electron injection can be modeled and quantified.[27, 141] The difference in molecular orbitals between both methods can be seen in Figure 3.7 using the

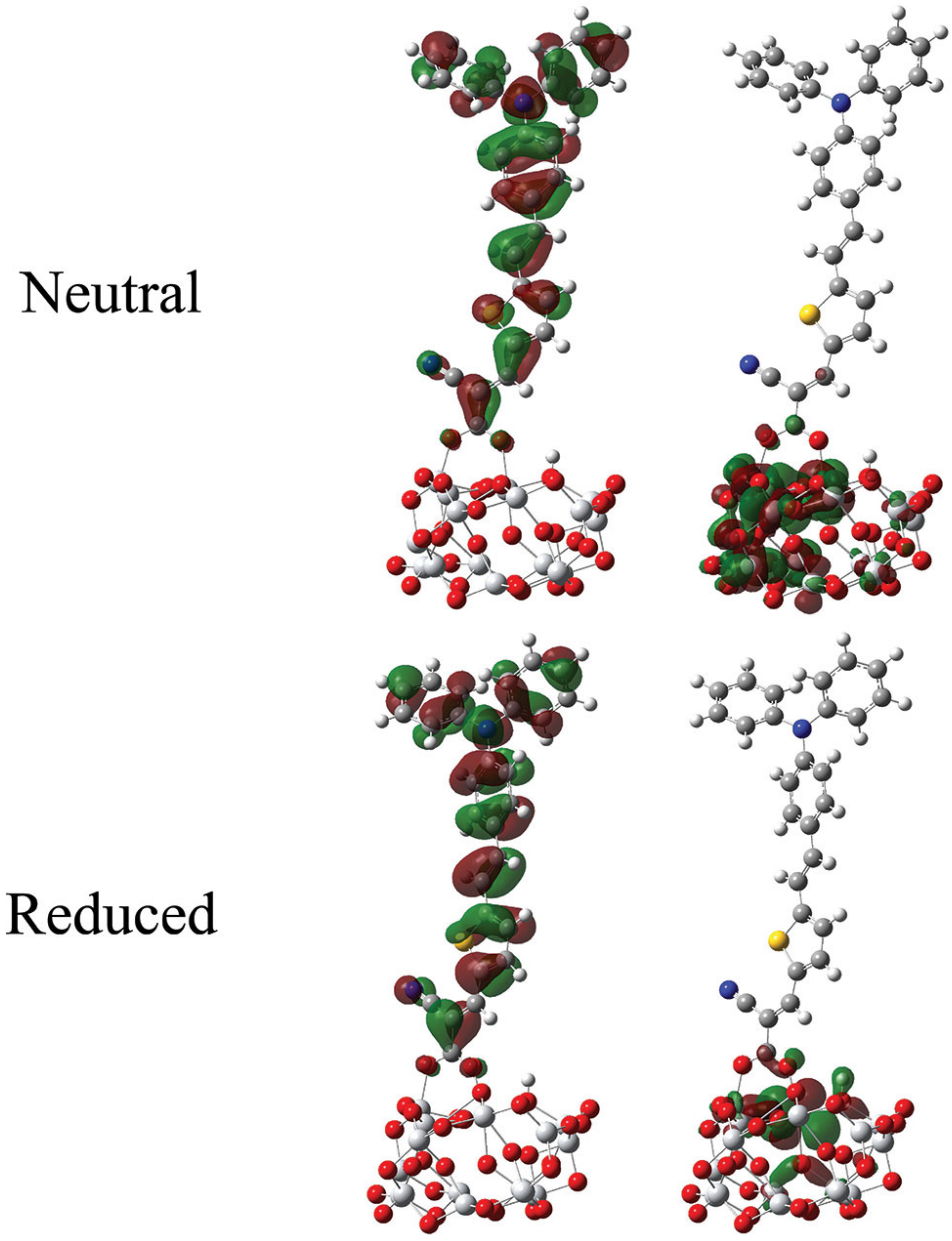

Figure 3.7. Representation of electron injection for the neutral and reduced species for the D5 organic dye on a $(TiO_2)_{16}$ surface. For the neutral system, the left and right signify the HOMO and LUMO orbitals. For the reduced system, the left and right signify the HOMO-1 and SOMO orbitals.

sulfur heteroatom in the π-bridge. Due to an electron being added to the system, this reduced system method involves inspecting the HOMO-1 and SOMO (single occupied molecular orbital) instead of the HOMO and LUMO used for the neutral state method. Even though there is little difference in the molecular orbital located on the dye molecule, the density in the surface is slightly different. Using the spin density difference between the dye and surface, a quantitative value for electron injection can be obtained. Table 3.7 shows the spin density difference between the $(TiO_2)_{16}$ surface and each dye molecule, while Figure 3.8 shows the SOMO for each dye system studied when adsorbed onto the $(TiO_2)_{16}$ surface. It is revealed that the suspicions from earlier of the boron substituted dye not injecting into the surface were confirmed, as there was a negligible amount of density in the surface. It appears that all heteroatom substituted dye molecules, except boron, had electrons injections similar to the classical sulfur substituted system, having ~1% less density in the surface. These results are consistent with the approximation made earlier using the LHE values to approximate injection efficiency.

Table 3.7. Mulliken spin density difference between the surface and dye molecule and the totals to signify it correctly adds up to 100%.

Dye	Surface Density (%)	Dye Density (%)	Total (%)
B	0.96	99.04	100.00
C	98.80	1.20	100.00
N	98.90	1.10	100.00
O	98.81	1.19	100.00
P	98.80	1.20	100.00
S	99.51	0.49	100.00
As	98.73	1.27	100.00
Se	98.80	1.20	100.00

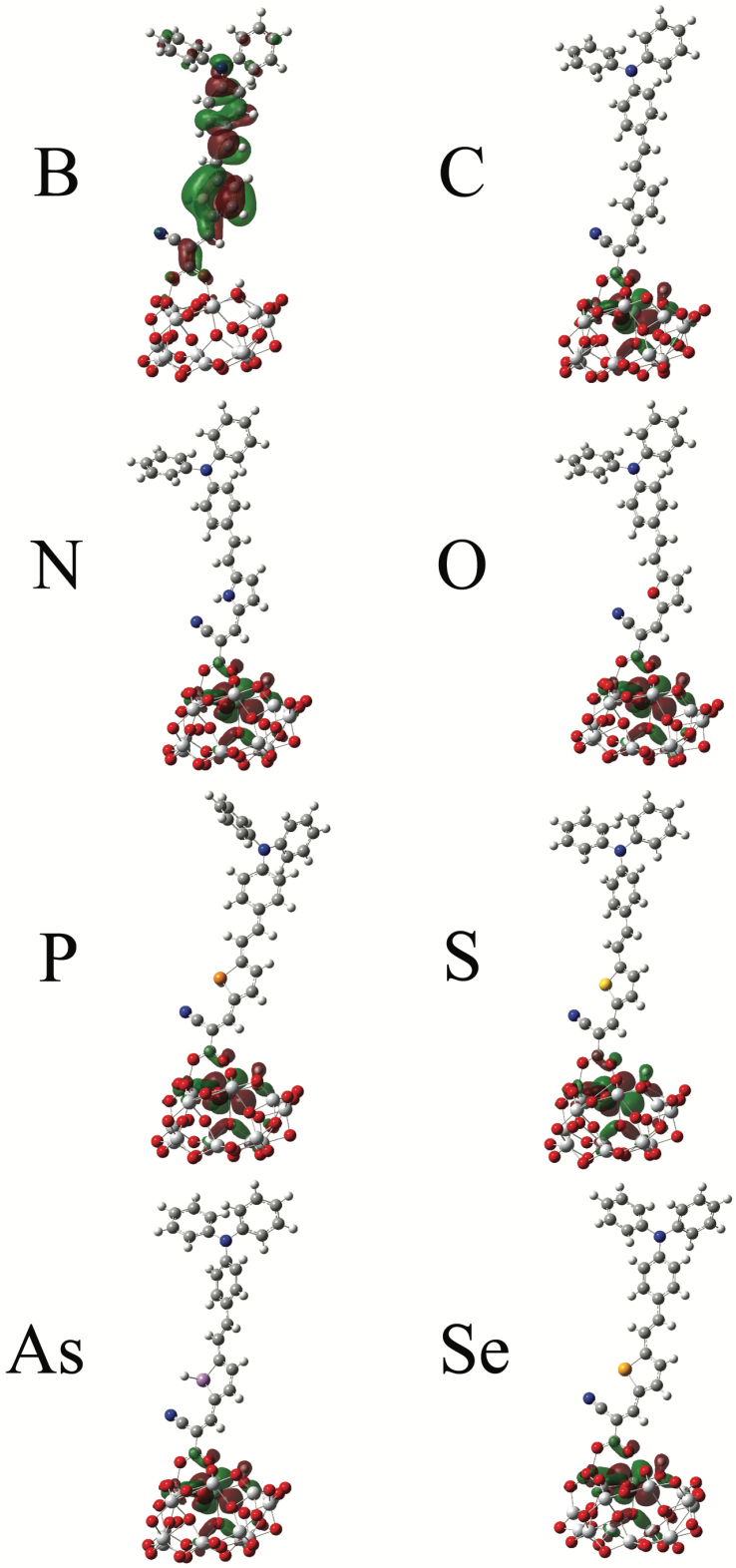

Figure 3.8. The SOMO for the reduced system of each of the studied dye molecules adsorbed on a $(TiO_2)_{16}$ surface.

3.5 Conclusion

Substituting different heteroatoms for the sulfur in the thiophene linker varied the properties of the sensitizer. In all cases the energy gap decreased, except for the substitution of oxygen or nitrogen, the two most electronegative atoms in our study. Electron injection into TiO_2 was found to be favorable for all substituted systems except boron. However, the substitution of boron provided the most dramatic results, by increasing the λ_{max} from less than 530 nm to 942.5 nm. This is attributed to a much smaller gap of the boron-substituted dye. The oscillator strengths are weaker, and the LUMO orbitals are not heavily localized on the acceptor portion of the dye, but the transition in the NIR could be further optimized to access the potential of that region of the solar spectrum. Even though the creation of dyes that use arsenic is not practical, this study has shown that large heteroatoms have a positive effect on the photovoltaic properties. Other third or fourth row elements may further improve the photovoltaic properties of these organic dyes. Future studies should examine dyes that utilize boron to enhance absorption in the NIR and improve its electron injection into TiO_2, potentially as a co-sensitizer, and to further understand the chemical phenomena associated with its unique spectrum.

3.6 Acknowledgements

This work is supported by the Chemical Sciences, Geosciences, and Biosciences Division, Office of Basic Energy Sciences, Office of Science, U. S. Department of Energy under Award Number DE-SC0010212.

CHAPTER FOUR

Photovoltaic and Charge Transfer Analysis of Perylene Diimide Dimer Systems

Portions of this chapter are in review at the *Journal of Photochemistry and Photobiology A: Chemistry* as: Smith, A. G.; Shuford, K. L., Photovoltaic and Charge Transfer Analysis of Perylene Diimide Dimer Systems

4.1 Abstract

The dimerization of perylene diimide (PDI) with a bridge separating each monomer has been of interest recently due to notable increases in device efficiencies. We aim to further investigate the impact this bridge has on the photovoltaic and charge transfer properties of an organic photovoltaic using electronic structure methods. Calculations were performed on a variety of heteroatom substituted bridge units in both fused and unfused PDI dimers to directly compare with the previously studied thiophene bridge unit. The systems consist of bridged PDI dimers as an acceptor, coupled with a known polymer donor. Using Marcus theory, the rates of intermolecular charge recombination (k_{CR}) and charge transfer (k_{CT}) were calculated using the Gibbs free energies, reorganization energy and electronic coupling for each system. Fused systems exhibit a k_{CT}/k_{CR} ratio up to 10^6 times higher than unfused systems, decreased reorganization energy, and had more favorable Gibbs free energies. NICS analysis was also done on the bridge units to investigate possible connections between aromaticity and photovoltaic properties. Oxygen, sulfur, selenium and nitrogen were determined to be aromatic for both fused and unfused systems, while silicon, arsenic, phosphorus and carbon were a mix between non- and anti-aromatic. Larger heteroatom substitutions, like silicon and phosphorus, have improved

photovoltaic and Marcus theory parameters, and show potential to perform better than typical thiophene linkers.

4.2 Introduction

Organic photovoltaics (OSCs) are among a new generation of solar cell technologies. These devices have grown in popularity due to their low-cost, flexibility, and simple synthetic process.[142-144] Power conversion efficiencies (PCEs) are a primary focus for OSC research. Recently, efficiencies over 14% have been reached for single junction cells.[57-58] Thus far, the most efficient OSCs utilize a bulk-heterojunction (BHJ), which is a blend of donor and acceptor materials throughout the active layer. Most OSCs have been designed around a fullerene acceptor, which debuted in OSC BHJs in 1995,[32, 145-146] due to efficient charge separation and the ability to transport electrons in three dimensions. However, fullerenes have many shortcomings, including difficulty in tuning the electronic properties, high cost of production, and questionable long-term stability.[54, 147] This has led to OSCs made with non-fullerene acceptors to become a subject of interest. Non-fullerene replacements, such as perylene diimide (PDI),[17] have improved stability and easily tuned molecular energy levels and absorption spectra, while also having a significantly lower production cost.[64] PDI systems suffer from low efficiencies due to aggregation of PDI and phase separation from the donor polymer due to strong π-π stacking.[148] Nonplanar PDI molecules were developed to combat this issue by the dimerization of PDI. This has been done with, and without, a bridge unit and have been studied previously.[64, 149-153]

A fused PDI dimer bridged by an ethylene group was synthesized, which improved charge separation and transfer in BHJ OSCs.[154] This led to the idea of substituting ring structures to act as bridges. This was done using a single bond connected to the bay region

of each PDI, or using two bonds and effectively fusing the units together with the bridge. Typically, the ring system was benzene, but thiophene has gained increased interest. Substituting different chalcogens into the fused bridge unit to modulate the electronic and geometric properties was achieved and produced a PCE of 6.72% for the sulfur substituted system.[155] A majority of bridge units that have been investigated consist of chalcogen rings, most often thiophene, and conjugated carbon systems.[155-156] To our knowledge, no studies have investigated the properties of pnictogen-ring species, particularly five membered rings, as bridge units for PDI dimers, and few have directly compared the properties between fused and unfused systems.[155] Details regarding the synthesis of the fused and unfused PDI dimers using chalcogens in the bridge unit have been described by Zhong et al.[155] This study aims to thoroughly investigate these pnictogen-ring species as bridge units for these PDI dimers and compare them to the more common chalcogen and carbon-ring systems.

Typically, the donor molecule is a conjugated polymer system. Recently, polymers have been extensively researched to optimize the photovoltaic properties.[157] This includes optimizing molecular energy levels to match a wide variety of acceptors, broadening and red-shifting the absorption band, and increasing hole mobility.[158] One subunit shown to improve charge transport efficiencies in polymers is benzo[1,2-b:4,5-b']dithiophene (BDT), which is easily tunable, features high hole mobility and can be readily synthesized. The substitution of 2-alkylthienyl to BDT has helped bring OSC efficiencies to new heights, being featured in many of the highest performing polymers.[159] One example is PBDT-TS1 (Figure 4.1), which is a proven polymer used in high PCE OSC's and will be used as the donor molecule for this study.[160]

Theoretical calculations play an important role in the field of organic semiconductors and OSC devices by providing a guideline for the rational synthesis, thus avoiding expensive trial-and-error attempts. The use of computational methods allows one to rapidly screen novel molecules and determine the viability in an OSC device. Throughout the years computational techniques have deepened the understanding of the mechanisms involved in determining device efficiency and has been at the forefront in the development of novel donor and acceptor molecules.[116, 161-163]

Using an ab initio approach to directly calculate the PCE ($=V_{OC}J_{SC}FF$ / Pin) of an OSC is a difficult task. The main factors that contribute to PCE are the short-circuit current density (J_{SC}), open-circuit voltage (V_{OC}) and fill factor (FF). There are routes for improving the contributions to PCE that ab initio methods can readily provide. These include increasing the energy gap between the highest occupied molecular orbital (HOMO) of the donor and lowest occupied molecular orbital (LUMO) of the acceptor to increase V_{OC}, and decreasing the band gap of the donor molecule to more closely match the solar spectrum and boost J_{SC}. Furthermore, the LUMO energy difference between donor and acceptor ΔE_{L-L}, denoted as the energetic driving force, should be greater than 0.3 eV to overcome columbic attraction and allow efficient charge separation.[144] There are two main processes at the D/A interface, intermolecular charge transfer (CT) and intermolecular charge recombination (CR). To improve J_{SC}, FF, and to increase the effective exciton dissociation, the rate of charge transfer (k_{CT}) should be as fast as possible. Also, the rate of charge recombination (k_{CR}) should be kept at a minimum. This can be readily analyzed using the ratio of the transfer rates for each system (k_{CT}/k_{CR}).

This study aims to provide a comprehensive ab initio analysis of the electronic and optical properties of PDI dimers, both fused and unfused, with 5-membered ring systems acting as bridge units. These rings will have one site substituted with various heteroatoms, which include the pnictogens, chalcogens, carbon and silicon as shown in Figure 4.1. Firstly, the ground state energies and UV spectra will be calculated for both the fused and unfused PDI dimers, from which the photovoltaic properties will be calculated. A charge transfer complex will be built using PDI and PBDT-TS1 to calculate the electronic coupling. The electronic coupling, reorganization energy and free energies will be combined to provide a picture for charge transfer and recombination rates via Marcus theory.

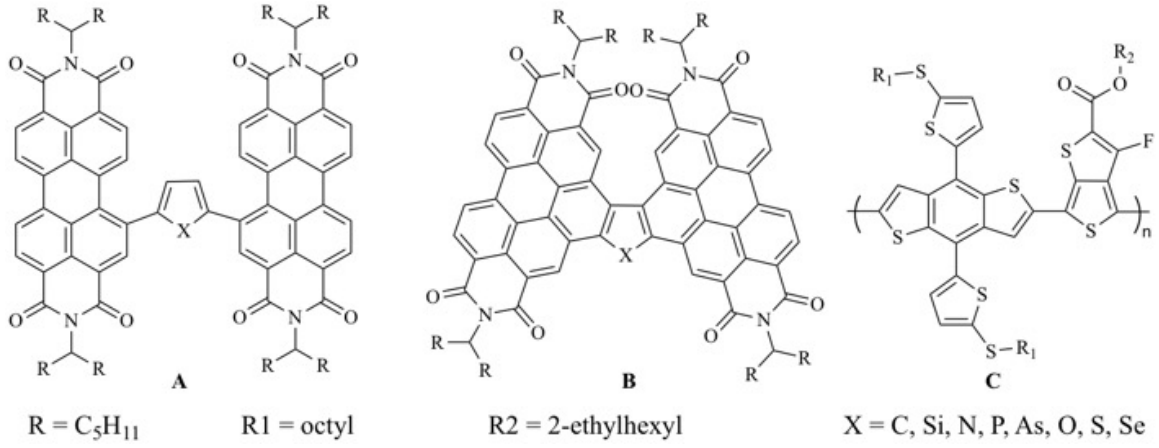

Figure 4.1. Chemical structures of studied systems: A) unfused PDI B) fused PDI and C) PBDT-TS1 donor polymer.

4.3 Methods

All optimization and time-dependent calculations are done using DFT and the 6-31G(d) Pople basis set, which has been shown to yield reliable results for evaluating the photovoltaic properties of OSC systems.[164] To determine the most appropriate functional

for this system, both ground and excited state energies were run using several DFT functionals including B3LYP, HSE06, PBE0, ωB97xD and CAM-B3LYP. All geometry and time dependent calculations were done in gas phase using the Gaussian09 software package.[119] Geometries from Gaussian09 were then used by the electron transfer module in NWChem[165] for the calculation of the electronic coupling (V_{AB}) using both the 6-31G(d) and 6-31+G(d) basis sets. This was done in order to determine the necessity of diffuse functions when calculating the electronic coupling. The carbon chains branching off the imide ends of PDI, shown in Figure 4.1, impact the solubility and active layer morphology but have little impact on the electronic structure.[166-167] These are replaced by a methyl group to ease computational expense.

In determining k_{CT} and k_{CR}, the Marcus rate equation was employed:[95]

$$k = \sqrt{\frac{4\pi^3}{h^2 \lambda k_b T}} |V_{AB}|^2 \exp\left(-\frac{(\Delta G + \lambda)^2}{4\lambda k_b T}\right) \quad (4.1)$$

ere ΔG is the Gibbs free energy change, λ is the reorganization energy and V_{AB} is the electronic coupling between the donor and acceptor. T is the temperature, which is set to 298 K, while k_b and h are the Boltzmann and Planck constants, respectively. The ΔG of charge recombination and charge transfer are expressed as ΔG_{CR} and $\Delta G_{CT,}$ respectively. ΔG is calculated as:[168]

$$\Delta G = E_{IP}(D) - E_{EA}(A) \quad (4.2)$$

where $E_{IP}(D)$ is the ionization potential of the donor, and $E_{EA}(A)$ is the electron affinity of the acceptor. These free energy changes are commonly estimated as the difference in orbital energies,[168] thus for charge recombination, ΔG_{CR} is taken as the donor HOMO energy minus the acceptor LUMO. By employing the Rehm-Weller equation, ΔG_{CT} can be calculated as:[168-169]

$$\Delta G_{CT} = -\Delta G_{CR} - \Delta E_{0\text{-}0} - E_b \quad (4.3)$$

where $\Delta E_{0\text{-}0}$ is the donor's lowest excited state energy (i.e., the excitation energy, E_{exc}, from the donor HOMO to S1). The exciton binding energy, E_b, incorporates the electron-hole Coulomb attraction and can be estimated as the difference between the electronic and optical band gaps.[35, 170] Another important parameter is $\Delta E_{L\text{-}L}$, the energy difference between the LUMO's of the donor and acceptor. A $\Delta E_{L\text{-}L}$ of at approximately 0.3 eV is considered adequate for efficient electron injection to occur.[171-172] These energies are visualized in Figure 4.2.

The total reorganization energy, λ_{tot}, is the energy required to reorganize the nuclei from the reactant to product geometries without electron transfer occurring and is the summation of internal (λ_{int}) and external (λ_{ext}) reorganization energies. The latter involves the effect of the surrounding medium, i.e. solvent, while the former pertains to the geometries of the donor and acceptor and can be evaluated as:[170]

$$\lambda_{int} = E(A^-) - E(A) + E(D) - E\left(D^+\right) \quad (4.4)$$

where E(A) and E(A^-) are the energies of the neutral acceptor at the ground-state and anionic geometries, respectively. E(D) and E(D^+) are the energies of the cation donor at the neutral and cation geometries, respectively. The λ_{ext} is difficult to accurately calculate, but Troisi et al. reported that estimating λ_{ext} within a realistic range would only effect the rate by a single order of magnitude.[166] Song et al. determined that for large systems λ_{ext} can be approximated as being equal to λ_{int} and found results that closely follow experimental values using this assumption. This would make λ_{tot}:[170, 173]

$$\lambda_{tot} = \lambda_{int} + \lambda_{ext} = 2\lambda_{int} \quad (4.5)$$

and from now on λ_{tot} will be referred to simply as λ.

Calculating V_{AB} between two molecules in a system has been proven to be an arduous task. The functional used makes a significant difference, especially the amount of Hartree-Fock exchange involved;[174] however, the trends tend to remain the same regardless, as long as the method and functional are kept constant.[175] There are a variety of methods to calculate V_{AB}, including generalized Mulliken-Hush (GMH), fragment charge difference

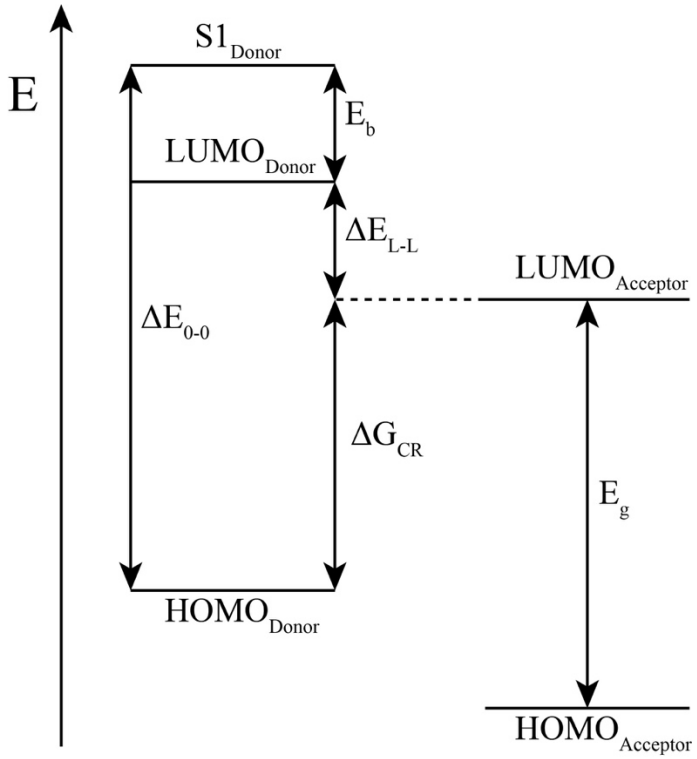

Figure 4.2. Donor and acceptor energy diagram

(FCD), and what is known as the direct coupling method (DC). For this study the DC method is used, for it is known to yield reliable results, and has a low computational cost.[175-177] The NWChem software package includes an electron transfer module, which utilizes Hartree-Fock to compute V_{AB} using the DC method via a 2-state method developed by Farazdel et al.:[178]

$$V_{AB} = \left(1 - S_{AB}^2\right)^{-1} \left[H_{AB} - \frac{1}{2} S_{AB}(H_{AA} + H_{BB})\right] \quad (4.6)$$

Where S_{AB} is the overlap integral, H_{AB} the interaction energy, and H_{AA} and H_{BB} the energies of reactant and product dimer states, respectively.

V_{OC} is an important parameter in calculating PCE of an OSC, and can be estimated by:[179]

$$V_{OC} = \frac{1}{e} \left(|E_{HOMO}(D)| - |E_{LUMO}(A)|\right) - 0.3 \text{ V} \quad (4.7)$$

where $E_{HOMO}(D)$ and $E_{LUMO}(A)$ are the HOMO and LUMO energies of the donor and acceptor, respectively, and e is the elementary charge. The subtraction of 0.3 V is an empirical factor used to more closely represent experimental results. It stems from energy losses during charge transport to the electrodes and various interface effects.[157] This empirical factor should not be confused with the $\Delta E_{L\text{-}L}$ difference of at least 0.3 eV mentioned previously.

4.4 Results and Discussion

4.4.1 Establishing PDI Benchmarks

Even though there have been studies conducted on testing bridge groups between PDI units,[64] to our knowledge there has not been an ab initio study that extensively tested similar bridges that only vary by a single atom, or directly compare fused and unfused systems. Using computational techniques, we can test the effects a particular heteroatom can have on a delocalized system. To ensure accurate analysis of the PDI systems, several DFT functionals were tested on the ground state of the sulfur substituted system, both fused and unfused. The molecular orbital energies are shown in Table 4.1, with experimental values representing the energies of the system as a thin-film.

The long-range corrected CAM-B3YLP and ωB97xD functionals performed the worst, predicting electronic gaps 2.58 eV and 3.65 eV larger than experiment for the fused system, and 2.56 eV and 3.62 eV larger for the unfused system, respectively. The hybrid functionals performed the best, but PBE0 could not accurately estimate the HOMO or LUMO energy, resulting in the electronic gap being off by ~33% for both fused and unfused systems. B3LYP accurately calculated the HOMO energy being off by only 2.3% and 1.3% for fused and unfused systems. However, the LUMO calculation was off by 8.5% and 11.5%, respectively. Even though B3LYP was more accurate in calculating the HOMO

Table 4.1. Functional test on the geometry optimization of PDI systems. E_g signifies the electronic gap between the HOMO and LUMO energy, while ΔE_g is the difference between E_g and the experimental gap. Experimental data is from Ref. [155].

Functional	Unfused				Fused			
	HOMO (eV)	LUMO (eV)	E_g (eV)	ΔE_g (eV)	HOMO (eV)	LUMO (eV)	E_g (eV)	ΔE_g (eV)
Experiment	-5.95	-4.02	1.93	-	-5.98	-3.77	2.21	-
B3LYP	-5.87	-3.56	2.31	0.38	-6.12	-3.45	2.67	0.46
CAM-B3LYP	-7.03	-2.54	4.49	2.56	-7.23	-2.44	4.79	2.58
PBE0	-6.11	-3.53	2.58	0.65	-6.38	-3.43	2.95	0.74
HSE06	-5.75	-3.87	1.89	-0.04	-6.03	-3.75	2.28	0.07
ωB97xD	-7.60	-2.05	5.55	3.62	-7.81	-1.95	5.86	3.65

energy for the unfused system compared to HSE06, it still had a worse estimation of the LUMO and electronic gap energies. HSE06 gave both HOMO and LUMO energies within 1% for fused systems and 3.8% for unfused systems, resulting in calculated electronic gaps being only 0.04 eV and 0.07 eV off from experiment for the unfused and fused system, respectively. It is important to note that for the calculation of photovoltaic properties, the

HOMO energy of the acceptor unit is not as pivotal to get correct as the LUMO energy. This is due to the LUMO energy being involved for the calculation of ΔE_{L-L}, ΔG_{CR} and V_{OC}. Thus for our purposes, HSE06 out-performed the other functionals, including the popular B3LYP, in both fused and unfused systems.

A functional test was also done on the time-dependent calculations (Table 4.2). The B3LYP, HSE06, PBE0, ωB97xD and CAM-B3LYP functionals were again tested on the sulfur substituted system, but this time to test accuracy of maximum absorption, λ_{max}, and excitation energy of the S_1 state, E_{exc}. It can be seen in Table 4.2 that similar trends can be

Table 4.2. Functional test on the time dependent density functional theory calculations. λ_{max} is the wavelength at the maximum absorbance and E_{exc} is the energy difference between the ground and first excited state (S_1). The "Δ" columns show the difference between tested and experimental values.

Functional	Unfused				Fused			
	λ_{max} (nm)	$\Delta\lambda_{max}$ (nm)	E_{exc} (eV)	ΔE_{exc} (eV)	λ_{max} (nm)	$\Delta\lambda_{max}$ (nm)	E_{exc} (eV)	ΔE_{exc} (eV)
Experiment	533	-	1.95	-	474	-	2.22	-
B3LYP	514	-19	1.95	0.00	468	-6	2.34	0.12
CAM-B3LYP	456	-77	2.46	0.51	406	-68	2.87	0.65
PBE0	502	-31	2.06	0.11	456	-18	2.47	0.25
HSE06	508	-25	1.91	-0.04	460	-14	2.29	0.07
ωB97xD	454	-79	2.51	0.56	398	-76	2.92	0.70

observed compared to the preceding optimization test, with CAM-B3YLP and ωB97xD functionals giving the least accurate results, B3LYP and HSE06 being the most accurate, and PBE0 being somewhere between these two groups. Unlike for the molecular orbital energies, B3LYP and HSE06 gave almost identical results for λ_{max} and E_{exc}. For the

unfused system, B3LYP was slightly more accurate, while for the fused system, B3LYP had a more accurate λ_{max}, and HSE06 resulted in a more accurate E_{exc}. Due to their results being so close, the HSE06 functional was chosen for further calculations to keep the functional consistent throughout ground and excited state calculations.

4.4.2 Excited State Calculations

Even though the primary goal is to have an excited donor state donate an electron to the acceptor, it is also important to improve absorption capabilities of the acceptor unit. Having a strong and complimentary absorption with the donor molecule can increase the photocurrent of the OSC, for without this, the predominant mechanism to generate photocurrent is a p-type excitation,[180] leading to electron transfer. An absorption band complimentary to the donor molecule would allow additional photocurrent from n-type excitations, leading to hole transfer from the acceptor to donor.[180-182] Table 4.3 shows the excitation energy to the S_1 state, E_{exc}, and the wavelength of the strongest peak, λ_{max}, calculated using the HSE06 functional. The finer details of the absorption spectra for the fused and unfused systems can be viewed when on a single axis (Figure 4.3). Band peaks are marked in Figure 4.3 to indicate which LUMO orbital is involved in the transition. The absorption spectra of each system on their own axis are shown in Figure 4.4. The excitation energy generally increased for all systems when moving down each column of the periodic table, except for the progression from phosphorus to arsenic, and the fused chalcogen systems. The fused chalcogens exhibit the opposite trend, with E_{exc} and λ_{max} decreasing when moving down the column. For both E_{exc} and λ_{max}, the pnictogen and carbon group substitutions had similar percent differences between fused and unfused moieties. For both groups the E_{exc} was ~25% larger in fused systems, and λ_{max} was ~14% smaller. For the

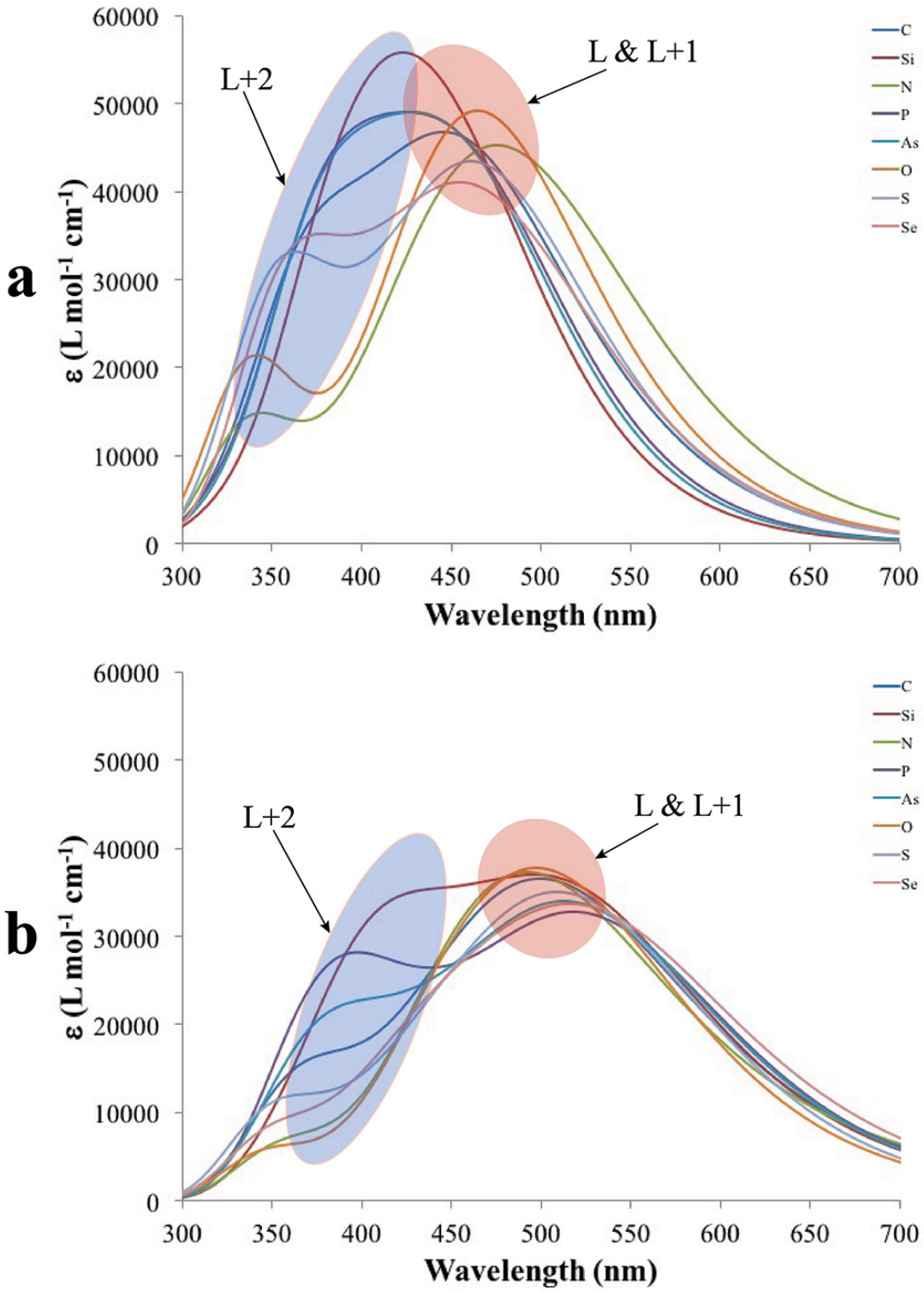

Figure 4.3. Absorption spectra for a) fused and b) unfused species. The blue region signifies the transitions to the LUMO+2 orbital, and the red region indicates the transitions to the LUMO and LUMO+1 orbitals.

chalcogens, however, these differences were smaller, being ~19% larger and ~10% smaller for E_{exc} and λ_{max}, respectively.

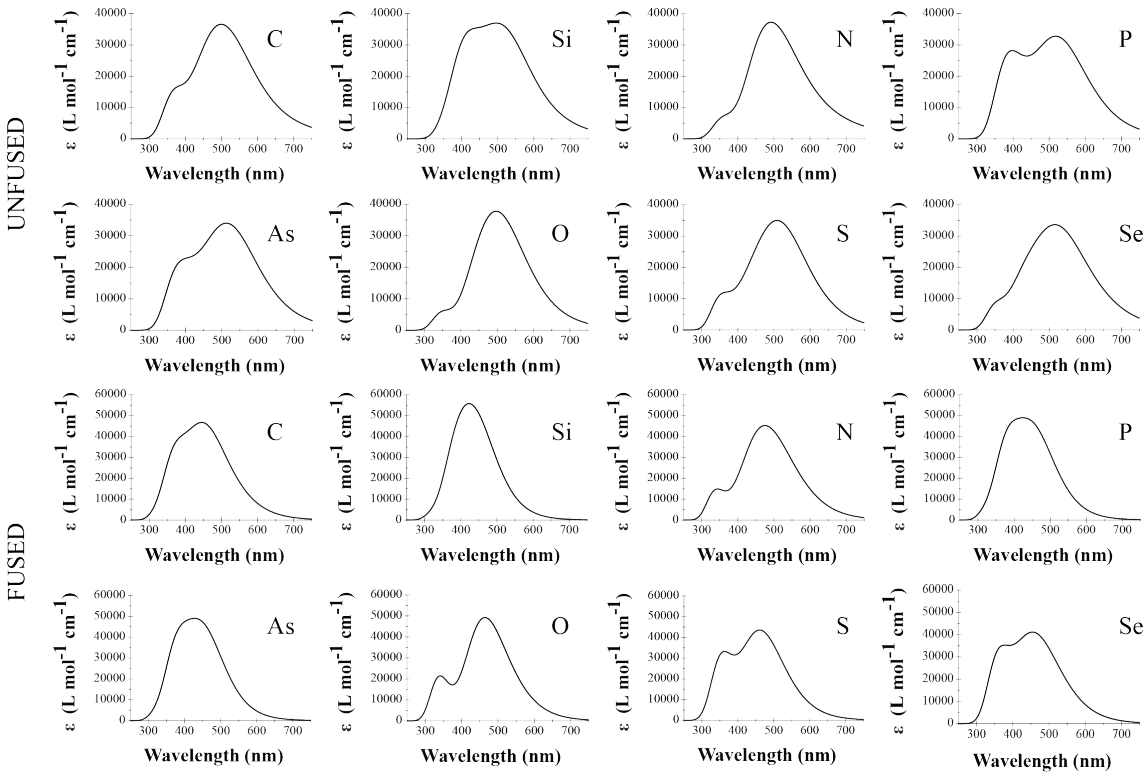

Figure 4.4. Absorption spectra of all heteroatom substituted species.

Table 4.3. The S_1 excitation energy and wavelength of the largest peak for PDI systems.

	Unfused		Fused	
System	E_{exc} (eV)	λ_{max} (nm)	E_{exc} (eV)	λ_{max} (nm)
C	1.77	500	2.33	446
Si	1.87	496	2.39	422
N	1.69	492	2.22	476
P	1.88	518	2.37	424
As	1.87	512	2.37	428
O	1.85	498	2.33	464
S	1.91	508	2.29	460
Se	1.92	516	2.26	454

The absorption spectra all exhibit a large red-shifted peak and smaller blue-shifted peak, sometimes seen more as a shoulder, seen in Figure 4.3. Transition assignments for each peak are shown in Table 4.4 and Table 4.5, for the unfused and fused systems,

Table 4.4. Electronic transitions corresponding to oscillator strengths for the large red-shifted peak and smaller blue-shifted peak for unfused systems. Transitions are ordered from highest to lowest percent composition. The blue-shifted peak is denoted as "Blue Peak" and "Red Peak" is the red-shifted peak.

System	Blue Peak	Red Peak
C	H → L+2, H → L+3	H-1 → L+1, H-1 → L
Si	H → L+2, H-2 → L+1	H-1 → L+1, H-1 → L
N	H → L+2, H-2 → L+1	H-1 → L+1, H-1 → L
P	H → L+2, H-2 → L	H-1 → L+1, H-1 → L
As	H → L+2, H-2 → L	H-1 → L+1, H → L+1
O	H → L+2, H-2 → L+1	H-1 → L+1, H-1 → L
S	H → L+2, H-2 → L+1	H-1 → L+1, H-1 → L
Se	H → L+2, H-2 → L+2	H-1 → L+1, H-1 → L

Table 4.5. Electronic transitions corresponding to oscillator strengths for the large red-shifted peak and smaller blue-shifted peak for fused systems. Transitions are ordered from highest to lowest percent composition. The blue-shifted peak is denoted as "Blue Peak" and "Red Peak" is the red-shifted peak.

System	Blue Peak	Red Peak
C	H → L+2, H-3 → L+1	H-1 → L, H-1 → L+1
Si	H → L+2, H-2 → L	H-2 → L+1, H-1 → L+1
N	H-1 → L+2, H-9 → L	H-1 → L+1, H → L
P	H → L+2, H-3 → L+1	H-1 → L, H → L+1
As	H-3 → L+1, H-1 → L+2	H-2 → L+1, H-1 → L+1
O	H → L+2, H-4 → L+1	H → L+2, H-1 → L
S	H-1 → L+2, H-2 → L	H-2 → L, H-1 → L+1
Se	H-1 → L+2, H-2 → L	H-2 → L, H-1 → L+1

respectively. The most red-shifted peak for each fused and unfused species consists of multiple transitions, predominately to the LUMO+1. The smaller blue-shifted peak is dominated by transitions to the LUMO+2, coming as no surprise seeing as a transition to the LUMO+2 requires a larger amount of energy. All non-chalcogen substitutions led to slightly more blue-shifted spectra; however, they have a broadened absorption spectrum compared to chalcogen systems, which could prove beneficial. They could compliment the more red-shifted donor molecule spectrum instead of competing for the same energies of the solar spectrum.

4.4.3 Molecular Orbital Analysis

Table 4.6 shows the molecular orbital energy levels and electronic gaps of the fused and unfused systems after heteroatom substitution. For unfused systems, the HOMO

Table 4.6. Molecular orbital energy levels and electronic gap of PDI systems.

	Unfused			Fused		
System	HOMO (eV)	LUMO (eV)	E_g (eV)	HOMO (eV)	LUMO (eV)	E_g (eV)
C	-5.63	-3.87	1.75	-5.98	-3.70	2.28
Si	-5.69	-3.86	1.83	-6.06	-3.68	2.37
N	-5.58	-3.87	1.70	-5.90	-3.71	2.18
P	-5.69	-3.85	1.85	-6.05	-3.72	2.34
As	-5.74	-3.90	1.84	-6.05	-3.70	2.35
O	-5.71	-3.86	1.86	-6.07	-3.78	2.29
S	-5.75	-3.87	1.89	-6.03	-3.75	2.28
Se	-5.77	-3.86	1.90	-5.99	-3.73	2.26

energy decreased and the LUMO remained relatively constant when moving down each column of the periodic table. This resulted in an increase in the electronic gap when moving down the column of the periodic table, matching the trend with the excitation energy. For

the fused systems, a similar trend in the change of the HOMO energy can be seen; however, the chalcogens reverse the trend. Both the HOMO and LUMO energies increased, which led to a decrease in the electronic gap when moving down the chalcogens. Also, when the electronic gap or HOMO energy is compared alongside the Pauling Electronegativity Scale,[135-136] the fused systems follow a linear trend, that as the electronegativity increases, the electronic gap decreases and HOMO level increases (Figure 4.5). This trend, however, does not also apply to the unfused systems.

The molecular orbital densities for sulfur substituted fused and unfused systems are shown in Figure 4.6 and are representative for the other systems in most cases. The HOMO orbitals for all systems are fairly similar, which explains why there is little variance in their energies. In fused systems, the LUMO and LUMO+1 are similar to one another, featuring delocalization throughout the PDI units with some electron density on the bridge. Unfused species shared the same relationship, however, there was an uneven amount of delocalization between the PDI units, with one PDI having a larger density than the other and was flipped between the LUMO and LUMO+1. The LUMO+2 orbitals are the only ones with a noticeable variance between systems, which can all be viewed in Figure 4.7. For the unfused systems, the LUMO+2 features a variety of densities, which explain the variations in the blue-shifted peak of the absorption spectrum (Figure 4.3). These vary from having substantial density on the bridge unit (Si, P, As), being localized to the bridge and one of the PDI units (C), or having no density on the bridge at all (N, O, S, Se). If you observe the strength of the blue-shifted peaks, it can be seen that the largest ones are silicon, phosphorus and arsenic, which had the largest LUMO+2 electron density on the bridge unit. Carbon had some density on the bridge unit and a strength right below arsenic. The

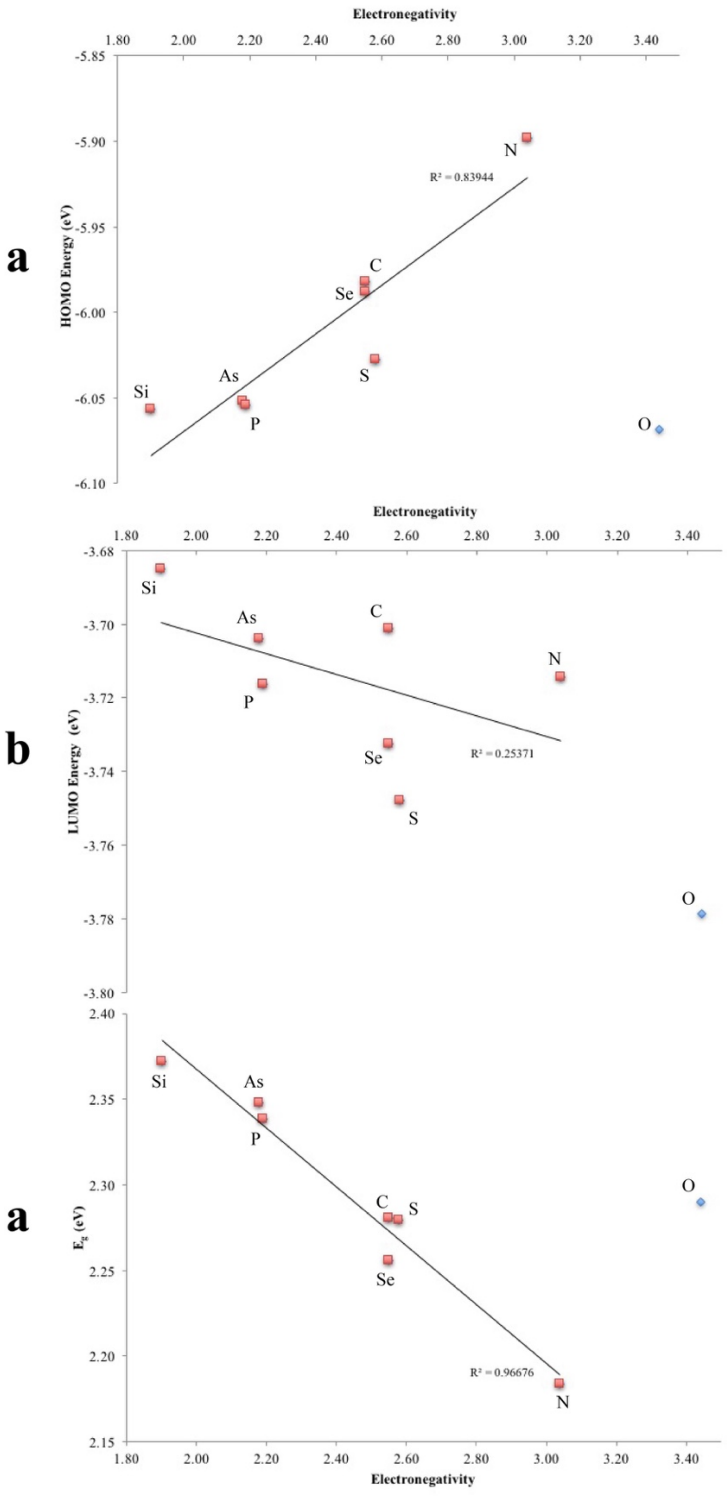

Figure 4.5. Electronegativity vs a) HOMO energy and b) LUMO energy and c) HOMO/LUMO gap (E_g) of fused PDI systems. The last data point (blue diamond) is oxygen and has been determined to be an outlier and left out of trend line calculation.

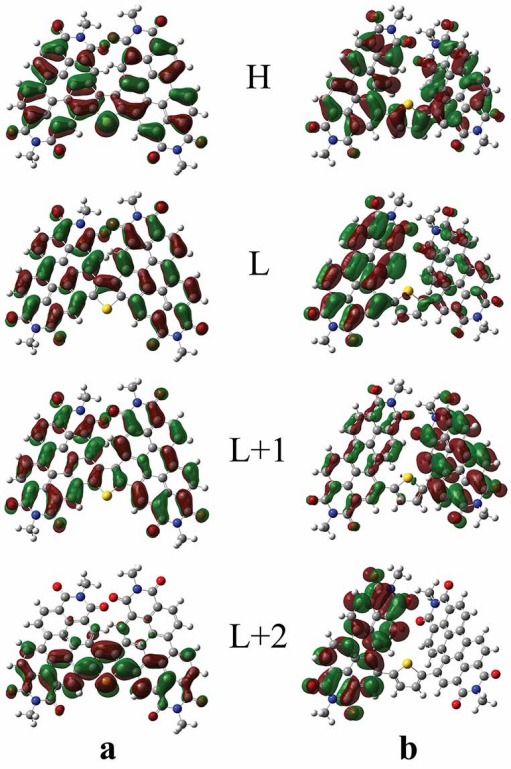

Figure 4.6. Molecular orbitals of sulfur substituted fused (left) and unfused (right) species.

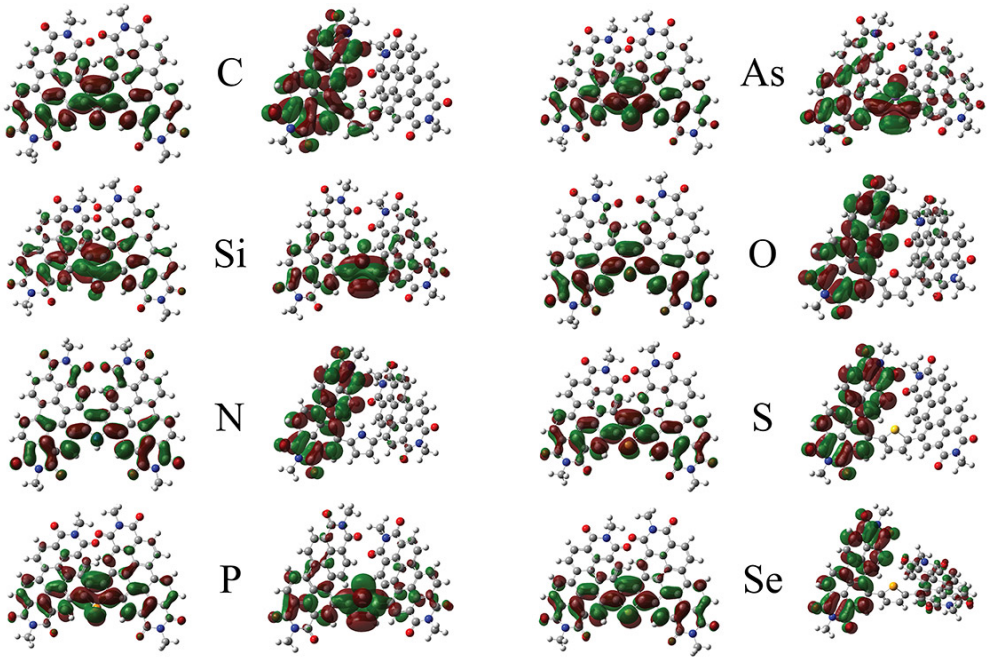

Figure 4.7. LUMO+2 orbitals for fused (left) and unfused (right) PDI systems.

smallest peaks belong to nitrogen, oxygen, sulfur and selenium, the cases where there was no density on the bridge. The LUMO+2 is heavily localized in and around the bridge unit in all fused systems, however, unlike for the unfused systems, there appears to be no trend to explain the variations in strength of the blue-shifted peak. These groupings continue when observing the LUMO+2 energies (Table 4.7). The group with the highest density on

Table 4.7. LUMO+1 (L+1) and LUMO+2 (L+2) energies for fused and unfused PDI systems, followed by the difference in energy with the HOMO.

	Unfused				Fused			
System	L+1 (eV)	L+2 (eV)	ΔE_{H-L+1} (eV)	ΔE_{H-L+2} (eV)	L+1 (eV)	L+2 (eV)	ΔE_{H-L+1} (eV)	ΔE_{H-L+2} (eV)
C	-3.70	-2.24	1.92	3.39	-3.53	-2.64	2.45	3.34
Si	-3.71	-2.61	1.98	3.08	-3.59	-2.91	2.47	3.15
N	-3.73	-2.25	1.85	3.33	-3.57	-2.23	2.33	3.66
P	-3.71	-2.42	1.98	3.27	-3.60	-2.81	2.45	3.24
As	-3.74	-2.46	2.01	3.28	-3.59	-2.80	2.46	3.25
O	-3.74	-2.22	1.97	3.49	-3.60	-2.36	2.47	3.71
S	-3.74	-2.25	2.01	3.50	-3.63	-2.56	2.39	3.47
Se	-3.81	-2.24	1.95	3.52	-3.63	-2.60	2.36	3.39

the bridge unit all had the lowest-lying energies, and the group with no density had the highest energy levels. All of the non-chalcogen substitutions, except nitrogen, had this larger blue-shifted band, broadening the overall absorption spectrum. In the cases that a blue-shifted peak is not readily seen, it is due to stronger, more redshifted transitions to the LUMO+2, bringing it closer to the red-shifted peak, and less small oscillator strength transitions involving the deep HOMO electrons.

4.4.4 Polymer Energies

The molecular orbitals of polymers can be difficult to accurately calculate using ab initio methods since polymers can be hundreds of units long. However, reasonable approximations can be made by only calculating an oligomer a few units long. Shown in Table 4.8 are the molecular orbital energies and electronic gap, along with the experimental values in thin film, of the PBDT-TS1

Table 4.8. PBDT-TS1 oligomer HOMO/LUMO energy levels and electronic gap, along with the calculated differences compared to experimental value.

Chain Length	HOMO (eV)	ΔHOMO (eV)	LUMO (eV)	ΔLUMO (eV)	E_g (eV)	ΔE_g (eV)
Experiment	-5.29	-	-3.40	-	1.89	-
n=1	-5.15	0.14	-2.40	1.00	2.74	0.85
n=2	-4.94	0.35	-2.90	0.50	2.04	0.15
n=3	-4.89	0.40	-3.12	0.28	1.78	-0.11
n=4	-4.83	0.46	-3.17	0.23	1.66	-0.23
n=5	-4.85	0.44	-3.22	0.18	1.63	-0.26

polymer (Figure 4.1).[183] Unit lengths of n=1-5 were optimized using the HSE06 functional and 6-31G(d) basis set. The HOMO of the n=1 system was the most accurate, while the LUMO is slowly converging to the experimental value as n increases. The electronic gap goes from being over-estimated, to under-estimated between chain lengths of two and three units due to the HOMO diverging from the experimental value. Since there was not one oligomer length that was accurate for calculating both the HOMO and LUMO energies, the n=1 polymer will be used for modeling the D/A interface with the PDI dimers due to having the most accurate HOMO level. For calculations involving the binding energy (Eq.

3), a value of -0.12 eV was used. This value comes from the difference between the electronic and optical gaps, as determined from calculations on the n=2 polymer that had an excitation energy of 2.16 eV and HOMO-LUMO gap of 2.04 eV. When the LUMO energy level is needed for calculation of $\Delta E_{L\text{-}L}$, the experimental value of -3.40 eV will be used.

4.4.5 D/A interface

The D/A interface was assembled by placing one side of the PDI dimer parallel to the donor and up 4.0 Å in the z-direction as shown in Figure 4.8. This distance has been shown to be a reliable starting distance for the D/A interface.[142] Shown in Table 4.9. is the difference in energy between the LUMO of the donor and LUMO of acceptor, $\Delta E_{L\text{-}L}$, and

Table 4.9. Difference between the LUMO of donor and acceptor, $\Delta E_{L\text{-}L}$, and the V_{OC} of investigated systems.

	Unfused		Fused	
System	$\Delta E_{L\text{-}L}$ (eV)	Voc (eV)	$\Delta E_{L\text{-}L}$ (eV)	Voc (eV)
C	0.47	0.98	0.30	1.15
Si	0.46	0.99	0.28	1.17
N	0.47	0.98	0.31	1.14
P	0.45	1.00	0.32	1.13
As	0.50	0.95	0.30	1.15
O	0.46	0.99	0.38	1.07
S	0.47	0.98	0.35	1.10
Se	0.46	0.99	0.33	1.12

the V_{OC} for all systems. A $\Delta E_{L\text{-}L}$ of at least 0.3 eV is considered adequate to promote efficient exciton dissociation. All unfused systems had an $\Delta E_{L\text{-}L}$ greater than 0.45 eV, while the fused systems were a lot closer to the 0.3 eV marker, with silicon actually being lower

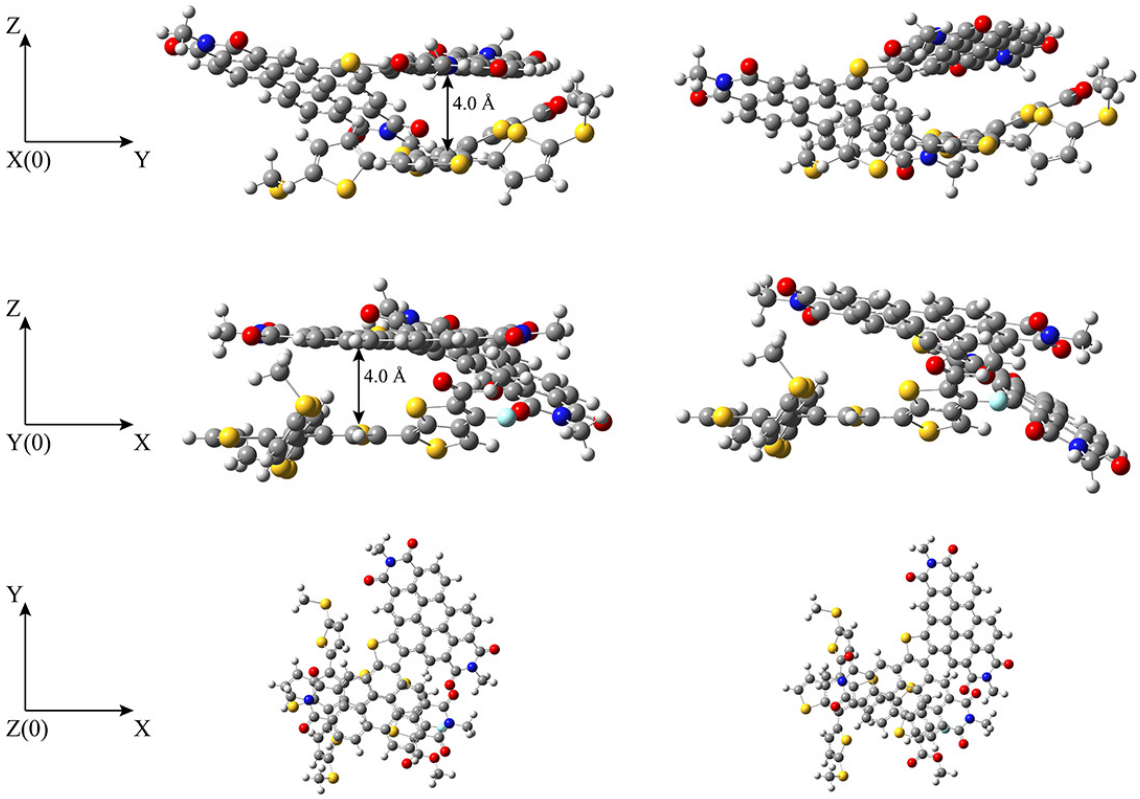

Figure 4.8. Orientation of the charge transfer complex along the x, y and z-directions. The PDI dimer is situated above the center of the donor polymer by 4.0 Å. For each view, the (0) designates the perspective.

at 0.28 eV. For V_{OC}, the calculated value for the unfused and fused sulfur substituted system were larger than experimental values using a similar donor polymer (PTB7-Th), with values of 0.88 and 0.94 eV, respectively.[155] Also, similar unfused PDI dimers that use the sulfur substituted bridge have V_{OC} values of ~0.88 eV when paired with the PBDT-TS1 polymer.[184-185] The results in Table 4.9 show V_{OC} values >0.1 eV larger than what was seen in experiment for similar D-A systems using an unfused PDI dimer. This shows that pairing these PDI dimers with PBDT-TS1 rather than PTB7-Th could lead to larger V_{OC} values. When comparing the fused and unfused systems, it is readily seen that the fused

systems had significantly larger V_{OC} values, with the largest being 1.17 eV for silicon. The largest for the unfused systems was phosphorus at 1.00 eV.

4.4.6 Photovoltaic Properties and Marcus Parameters

Table 4.10 shows ΔG_{CT}, ΔG_{CR}, and λ for both the fused and unfused systems. According to Marcus theory, as $|\Delta G|$ and λ get closer together the rate increases, the maximum rate being when they are equal. Once their values cross, the Marcus inverted region is reached, and as $|\Delta G|$ gets further from λ, the rate will exponentially decrease. For all systems, $|\Delta G_{CT}|$ was closer to λ than $|\Delta G_{CR}|$, showing favorable charge transfer energies. The fused systems exhibit improved ΔG_{CR} and ΔG_{CT} compared to the unfused systems, having absolute values further and closer to λ, respectively. It can be easily seen that there is not much variance in λ amongst the fused and unfused systems, but it can be noted that it is consistently lower in the fused cases.

Table 4.10: Photovoltaic variables for investigated systems: Gibbs free energy of charge recombination (ΔG_{CR}) and charge transfer (ΔG_{CT}), and reorganization energy (λ).

	Unfused			Fused		
System	ΔG_{CR} (eV)	ΔG_{CT} (eV)	λ (eV)	ΔG_{CR} (eV)	ΔG_{CT} (eV)	λ (eV)
C	-1.28	-0.76	0.40	-1.45	-0.59	0.37
Si	-1.29	-0.75	0.39	-1.47	-0.57	0.37
N	-1.28	-0.76	0.41	-1.44	-0.60	0.37
P	-1.30	-0.74	0.39	-1.43	-0.61	0.37
As	-1.25	-0.79	0.40	-1.45	-0.59	0.37
O	-1.29	-0.75	0.39	-1.37	-0.67	0.37
S	-1.28	-0.76	0.39	-1.40	-0.64	0.37
Se	-1.29	-0.75	0.41	-1.42	-0.62	0.37

Electronic couplings were calculated using both the pre- and post-optimized systems to determine if there is a significant difference between the electronic couplings and resulting rate constants. Table 4.11 shows the electronic coupling values for the pre-optimized systems and compares the difference between the 6-31G(d) and 6-31+G(d) basis sets, while Table 4.12 presents the post-optimization values. It is readily observed that in

Table 4.11. Comparison between the 6-31G(d) and 6-31+G(d) basis sets for calculation of the electronic coupling (V_{AB}) for the unfused (UF) and fused (F) systems in a pre-optimized state. The percent difference between each is also shown.

System	6-31G(d)		6-31+G(d)		% Difference	
	UF V_{AB} (eV)	F V_{AB} (eV)	UF V_{AB} (eV)	F V_{AB} (eV)	UF	F
C	5.99E-04	1.39E-03	7.24E-04	1.97E-02	18.90%	173.76%
Si	1.21E-03	1.20E-02	1.90E-03	8.65E-03	44.81%	32.43%
N	3.12E-04	1.83E-03	3.97E-04	9.11E-03	23.98%	133.25%
P	5.03E-04	5.28E-03	8.16E-04	1.06E-03	47.46%	133.07%
As	1.26E-03	2.19E-02	2.40E-03	1.28E-04	62.26%	197.68%
O	1.13E-03	1.83E-03	2.08E-03	9.11E-03	59.51%	133.25%
S	6.99E-04	1.16E-02	1.38E-03	1.29E-02	65.71%	10.78%
Se	3.62E-03	1.11E-02	4.67E-03	1.58E-02	25.38%	34.92%

the pre-optimized state, the electronic coupling for fused systems had a much greater change for each case except for silicon, sulfur, and selenium. The other fused systems saw their electronic couplings double upon adding diffuse functions. However, all are within an order of magnitude of each other, except for the fused arsenic system, which increased by two orders of magnitude upon adding diffuse functions. For the post-optimization state, there was more uniformity between the basis sets compared to the pre-optimized states, and all systems changed by no more than a single order of magnitude. When moving down

each periodic group, except for the chalcogens, in unfused systems, V_{AB} tends to increase. A common theme between both pre- and post-optimized systems is that the electronic coupling increases upon adding diffuse functions.

Table 4.12. Comparison between the 6-31G(d) and 6-31+G(d) basis sets for calculation of the electronic coupling (V_{AB}) for the unfused (UF) and fused (F) systems in a post-optimized state. The percent difference between each is also shown.

	6-31G(d)		6-31+G(d)		% Difference	
System	UF V_{AB} (eV)	F V_{AB} (eV)	UF V_{AB} (eV)	F V_{AB} (eV)	UF	F
C	2.88E-04	9.49E-03	6.90E-05	1.32E-02	122.69%	32.61%
Si	1.11E-03	1.70E-03	1.75E-03	3.16E-04	44.28%	137.36%
N	6.15E-04	3.77E-03	2.99E-04	1.86E-03	69.15%	67.83%
P	6.94E-04	8.35E-04	9.73E-04	1.90E-03	33.47%	77.79%
As	1.09E-03	1.17E-02	1.58E-03	1.53E-02	37.30%	26.77%
O	2.78E-03	3.78E-03	5.15E-03	1.85E-03	59.70%	68.59%
S	1.17E-04	3.44E-03	7.52E-04	3.85E-03	146.14%	11.19%
Se	6.11E-04	1.27E-04	4.92E-03	2.90E-04	155.84%	78.18%

Tables 4.13 and 4.14 show the corresponding transfer rates for charge recombination (k_{CR}), charge transfer(k_{CT}), and the charge transfer ratio (k_{CT}/k_{CR}) for the pre-optimized systems at the 6-31G(d) and 6-31+G(d), respectively. Tables 4.15 and 4.16 show the same information, but for the post-optimized systems. The main trait noticed is that no matter what basis set is used, or if it is in the pre- or post-optimized state, the k_{CT}/k_{CR} ratio remains the same. This is due to the free energies and reorganization energies remaining the same, and only V_{AB} is being altered. This leads to increases or decreases to the V_{AB} but since k_{CT} and k_{CR} change together, the ratio remains constant. For future studies, this phenomenon could be used to save computation time and only use the pre-

Table 4.13. The rate of charge recombination (k_{CR}), charge transfer (k_{CT}), and charge transfer ratio (k_{CT}/k_{CR}) for the pre-optimized systems using the 6-31G(d) basis set.

	Unfused			Fused		
System	k_{CR} (s^{-1})	k_{CT} (s^{-1})	k_{CT} / k_{CR}	k_{CR} (s^{-1})	k_{CT} (s^{-1})	k_{CT} / k_{CR}
C	1.06E+02	4.40E+08	4.14E+06	3.02E-03	1.46E+10	4.83E+12
Si	6.82E+01	1.40E+09	2.05E+07	1.23E-01	1.35E+12	1.10E+13
N	3.86E+01	1.22E+08	3.15E+06	1.46E-02	2.24E+10	1.54E+12
P	5.91E+00	3.39E+08	5.75E+07	1.09E-01	1.79E+11	1.64E+12
As	1.78E+03	1.11E+09	6.24E+05	9.50E-01	3.58E+12	3.76E+12
O	5.19E+01	1.34E+09	2.58E+07	3.01E-01	8.54E+09	2.84E+10
S	3.83E+01	5.01E+08	1.31E+07	3.46E+00	5.79E+11	1.68E+11
Se	3.58E+03	1.99E+10	5.55E+06	1.20E+00	6.41E+11	5.35E+11

Table 4.14. The rate of charge recombination (k_{CR}), charge transfer (k_{CT}), and charge transfer ratio (k_{CT}/k_{CR}) for the pre-optimized systems using the 6-31+G(d) basis set.

	Unfused			Fused		
System	k_{CR} (s^{-1})	k_{CT} (s^{-1})	k_{CT} / k_{CR}	k_{CR} (s^{-1})	k_{CT} (s^{-1})	k_{CT} / k_{CR}
C	1.55E+02	6.42E+08	4.14E+06	6.13E-01	2.96E+12	4.83E+12
Si	1.70E+02	3.49E+09	2.05E+07	6.38E-02	7.02E+11	1.10E+13
N	6.25E+01	1.97E+08	3.15E+06	3.63E-01	5.58E+11	1.54E+12
P	1.55E+01	8.93E+08	5.75E+07	4.39E-03	7.21E+09	1.64E+12
As	6.44E+03	4.02E+09	6.24E+05	3.23E-05	1.22E+08	3.76E+12
O	1.77E+02	4.57E+09	2.58E+07	7.51E+00	2.13E+11	2.84E+10
S	1.50E+02	1.96E+09	1.31E+07	4.29E+00	7.18E+11	1.68E+11
Se	5.97E+03	3.31E+10	5.55E+06	2.42E+00	1.30E+12	5.35E+11

Table 4.15. The rate of charge recombination (k_{CR}), charge transfer (k_{CT}), and charge transfer ratio (k_{CT}/k_{CR}) for the post-optimized systems using the 6-31G(d) basis set.

	Unfused			Fused		
System	k_{CR} (s^{-1})	k_{CT} (s^{-1})	k_{CT} / k_{CR}	k_{CR} (s^{-1})	k_{CT} (s^{-1})	k_{CT} / k_{CR}
C	2.45E+01	1.02E+08	4.14E+06	1.42E-01	6.86E+11	4.83E+12
Si	5.80E+01	1.19E+09	2.05E+07	2.47E-03	2.72E+10	1.10E+13
N	1.50E+02	4.72E+08	3.15E+06	6.20E-02	9.52E+10	1.54E+12
P	1.12E+01	6.46E+08	5.75E+07	2.72E-03	4.47E+09	1.64E+12
As	1.32E+03	8.23E+08	6.24E+05	2.69E-01	1.01E+12	3.76E+12
O	3.17E+02	8.18E+09	2.58E+07	1.29E+00	3.66E+10	2.84E+10
S	1.07E+00	1.40E+07	1.31E+07	3.03E-01	5.08E+10	1.68E+11
Se	1.02E+02	5.68E+08	5.55E+06	1.57E-04	8.40E+07	5.35E+11

Table 4.16. The rate of charge recombination (k_{CR}), charge transfer (k_{CT}), and charge transfer ratio (k_{CT}/k_{CR}) for the post-optimized systems using the 6-31+G(d) basis set.

	Unfused			Fused		
System	k_{CR} (s^{-1})	k_{CT} (s^{-1})	k_{CT} / k_{CR}	k_{CR} (s^{-1})	k_{CT} (s^{-1})	k_{CT} / k_{CR}
C	1.41E+00	5.84E+06	4.14E+06	2.74E-01	1.32E+12	4.83E+12
Si	1.43E+02	2.93E+09	2.05E+07	8.51E-05	9.37E+08	1.10E+13
N	3.54E+01	1.12E+08	3.15E+06	1.51E-02	2.32E+10	1.54E+12
P	2.21E+01	1.27E+09	5.75E+07	1.41E-02	2.31E+10	1.64E+12
As	2.81E+03	1.75E+09	6.24E+05	4.61E-01	1.74E+12	3.76E+12
O	1.09E+03	2.80E+10	2.58E+07	3.09E-01	8.75E+09	2.84E+10
S	4.43E+01	5.80E+08	1.31E+07	3.80E-01	6.36E+10	1.68E+11
Se	6.64E+03	3.68E+10	5.55E+06	8.18E-04	4.38E+08	5.35E+11

optimized D-A system. For the rest of this section, however, the post-optimized D-A system using the 6-31+G(d) basis set will be what is referenced (Table 4.16).

When directly comparing the fused systems with their unfused counterparts, fused systems experience a larger V_{AB} and k_{CT} with the donor, except for the selenium, oxygen, and silicon substitutions. Also, each fused system exhibited a slower k_{CR} compared to its unfused counterpart. This led to fused systems exhibiting a massive increase in the k_{CT}/k_{CR} ratio, being 10^6 times higher on average than the unfused counterparts, potentially leading to major improvements in J_{SC}, FF and exciton dissociation efficiency.

In fused systems, all the pnictogen and carbon group substitutions had increased k_{CT}/k_{CR} compared to chalcogens, often resulting from slower rates of charge recombination. When moving down the periodic group, the rate of charge recombination tends to increase in unfused species, except when progressing from nitrogen to phosphorus and oxygen to sulfur. Also, when moving down each column for the unfused systems, except for the chalcogens, the charge transfer rate tends to increase. A fairly common trend between both kinds of systems was that the k_{CT}/k_{CR} ratio increased when moving down each periodic group. However, there some exceptions to this for unfused cases. The chalcogen substitutions, and the progression from phosphorus to arsenic, which all show decreases in the k_{CT}/k_{CR} ratio.

The arsenic substituted systems experienced the largest improvement when going from an unfused to fused state, with the charge recombination rate decreasing by ~10^4 and k_{CT}/k_{CR} ratio increasing by ~10^7. Silicon had one of the largest k_{CT}/k_{CR} ratios in both the fused and unfused species, the most favorable ΔG_{CR} and ΔG_{CT} values, with phosphorus not far behind. Silicon and phosphorus could prove to be a more suitable heteroatom than the more common sulfur due to having higher V_{OC}, slower rate of charge recombination and larger k_{CT}/k_{CR} ratio in both systems. Carbon provided improved photovoltaic parameters

in fused systems compared to the chalcogens by having slower and faster charge recombination and charge transfer rates, respectively. Benzene has been tested as a bridge unit in the past,[142, 152, 156] but the 5-membered carbon ring, cyclopentadiene, should be further investigated.

4.4.7 NICS Analysis

An important task of the bridge unit is to provide a channel for the electrons between the two PDI units. One method that can be used to measure this is a nucleus-independent chemical shifts (NICS) analysis, which was first introduced by Schleyer et al. in 1996.[186] This analysis involves the measurement of aromaticity of ring systems, and is widely used in the literature.[187-190] The process involves simulating the NMR spectrum of the molecule, and measuring the NMR shielding tensor of a ghost atom within the ring system of interest. There are two NICS measurements that are most accepted, the first being $NICS(0)_{iso}$ which places the ghost atom within the plane of the ring and uses the negative of the isotropic shield tensor. The other is $NICS(1)_{zz}$, which has the ghost atom situated 1.0 Å above the plane of the ring, and uses the negative of the shield tensor for the specific direction the ghost atom is from the plane, which is usually the z-direction. The $NICS(1)_{zz}$ is a common measurement to use due to it measuring the shielding created by π-electrons in the ring. The larger the shielding, the more π-density there is in the ring, and therefore, greater aromaticity. The value of 1.0 Å was found, on average, to be the distance for the max shielding for ring systems. A system is considered aromatic if the negative of the shield tensor is a negative number, non-aromatic if it's close to zero, and anti-aromatic if it's positive. All calculations were done at the GIAO-B3LYP/6-311+G(d,p) computational level using Gaussian09.[119] The bridge unit is then aligned along the x and y-axes so the

face of the ring is in the z-direction. A property of ghost atoms is that they will not interact with other atoms, so the $NICS(0)_{iso}$ and $NICS(1)_{zz}$ can be measured simultaneously, as illustrated in Figure 4.9.

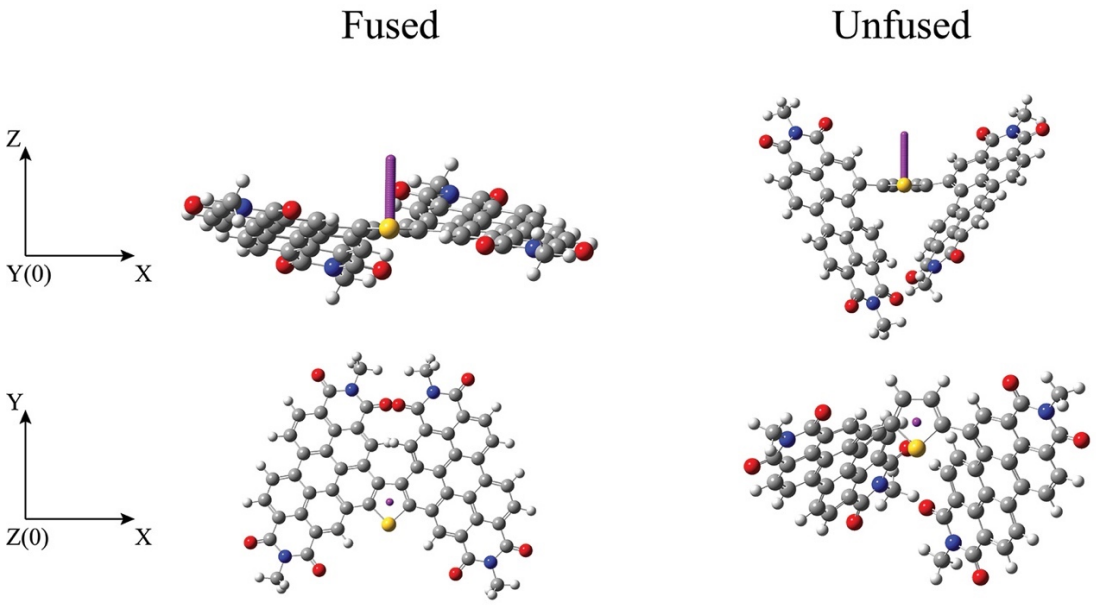

Figure 4.9. Placement of ghost atoms (purple) for the fused and unfused systems. The top views look down the y-axis and show the distance increase for the ghost atoms in the z-direction. Bottom views look down the z-axis.

The distance of 1.0 Å has been mainly determined using systems like benzene, in other words, ring systems entirely made of carbon. The ring systems investigated here utilize heteroatoms larger than carbon, and so it is prudent to scan several distances to determine which one provides the maximum $NICS_{zz}$ value. Table 4.17 shows this data in a tabular form for fused systems between 0.0-3.0 Å above the ring of the bridge unit in increments of 0.1 Å. The graphical version of this data is shown in Figure 4.10. Tabular $NICS_{zz}$ data for unfused PDI systems is in Table 4.18, while the graphical representation is shown in Figure 4.11.

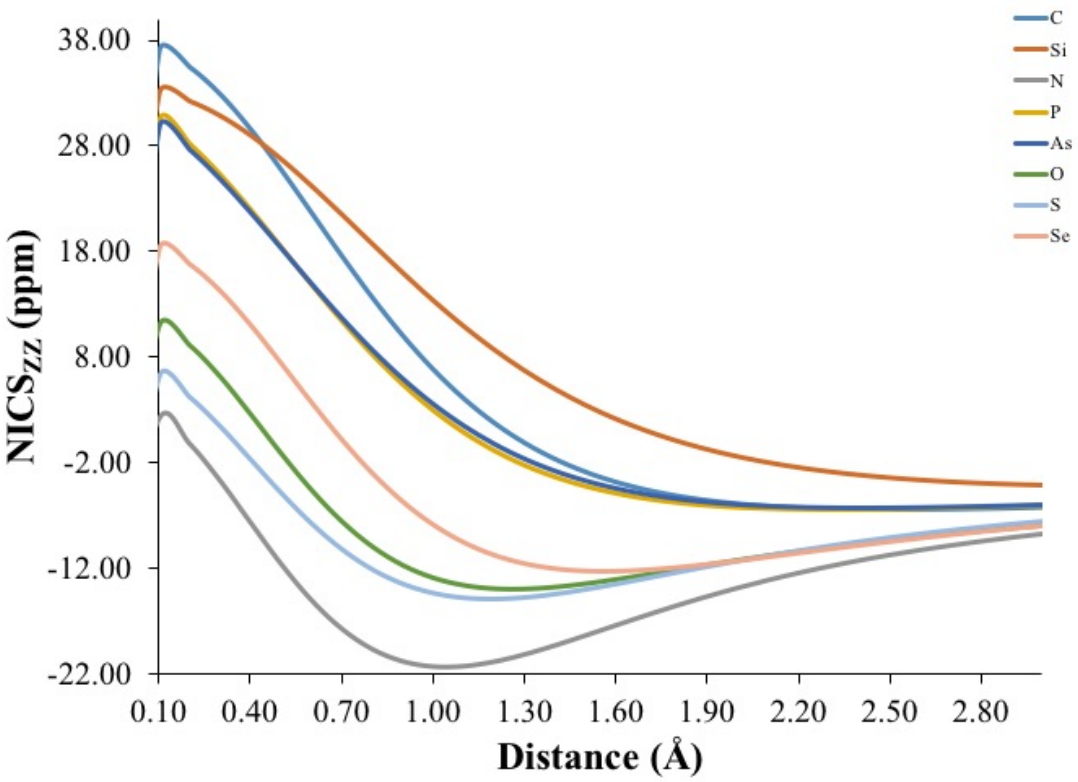

Figure 4.10. The change in the $NICS_{zz}$ value in fused PDI systems as the distance of the ghost atom from the plane of the ring increases from 0.00 Å to 3.00 Å.

There is a clear separation between the aromatic and non- or anti-aromatic systems. Oxygen, nitrogen, sulfur, and selenium are clearly aromatic, while carbon, silicon, phosphorus and arsenic are split. Phosphorus and arsenic are very close to zero at 1.00 Å, 2.90 and 3.58 ppm, respectively, and even closer at 1.10 Å, being at 0.81 and 1.53, respectively. Carbon and silicon seem to be anti-aromatic, with the former of the two being closer to non-aromatic, with values of 6.87 and 13.35 ppm, respectively. For the aromatic systems, nitrogen was the most aromatic by a wide margin, and all the chalcogen species resulted in aromatic ring systems. Also, for aromatic systems except selenium, the maximum $NICS_{zz}$ value was at approximately 1.00 Å mark mentioned earlier. Oxygen, nitrogen and sulfur had maximum $NICS_{zz}$ values at 1.30 Å, 1.00 Å and 1.20 Å,

Table 4.17. $NICS_{zz}$ values for fused PDI systems. Distance represents how far in angstroms the ghost atom is located from the plane of the ring. Values are in ppm.

Distance (Å)	C	Si	N	P	As	O	S	Se
0.00	37.78	36.95	3.41	30.48	37.58	11.85	12.68	18.37
0.10	37.21	36.85	2.55	30.72	37.17	11.07	12.05	17.77
0.20	35.56	36.13	0.14	30.01	35.81	8.87	10.23	16.00
0.30	32.94	34.82	-3.39	28.40	33.61	5.63	7.46	13.27
0.40	29.57	32.95	-7.47	26.02	30.71	1.83	4.07	9.86
0.50	25.69	30.60	-11.54	23.06	27.29	-2.03	0.44	6.11
0.60	21.55	27.88	-15.14	19.73	23.56	-5.58	-3.10	2.35
0.70	17.41	24.91	-18.00	16.24	19.70	-8.57	-6.29	-1.19
0.80	13.45	21.81	-20.03	12.79	15.91	-10.90	-8.97	-4.32
0.90	9.83	18.72	-21.25	9.54	12.31	-12.57	-11.08	-6.93
1.00	6.63	15.74	-21.77	6.59	9.02	-13.66	-12.62	-9.01
1.10	3.88	12.95	-21.74	4.01	6.10	-14.26	-13.65	-10.56
1.20	1.59	10.40	-21.31	1.80	3.57	-14.48	-14.23	-11.65
1.30	-0.30	8.12	-20.59	-0.04	1.42	-14.42	-14.47	-12.35
1.40	-1.81	6.11	-19.71	-1.54	-0.35	-14.16	-14.43	-12.72
1.50	-3.02	4.36	-18.74	-2.73	-1.80	-13.78	-14.21	-12.85
1.60	-3.96	2.86	-17.74	-3.68	-2.96	-13.33	-13.85	-12.79
1.70	-4.68	1.58	-16.76	-4.41	-3.89	-12.84	-13.41	-12.59
1.80	-5.23	0.49	-15.81	-4.97	-4.60	-12.34	-12.92	-12.30
1.90	-5.65	-0.42	-14.92	-5.38	-5.16	-11.85	-12.42	-11.96
2.00	-5.95	-1.19	-14.10	-5.68	-5.57	-11.38	-11.91	-11.58
2.10	-6.17	-1.83	-13.34	-5.89	-5.88	-10.93	-11.41	-11.18
2.20	-6.31	-2.36	-12.64	-6.03	-6.10	-10.52	-10.94	-10.78
2.30	-6.40	-2.80	-12.00	-6.12	-6.24	-10.12	-10.48	-10.38
2.40	-6.45	-3.16	-11.43	-6.16	-6.33	-9.76	-10.05	-10.00
2.50	-6.47	-3.45	-10.90	-6.17	-6.38	-9.42	-9.65	-9.63
2.60	-6.45	-3.69	-10.42	-6.15	-6.40	-9.10	-9.28	-9.28
2.70	-6.42	-3.88	-9.98	-6.11	-6.38	-8.81	-8.93	-8.95
2.80	-6.37	-4.03	-9.58	-6.06	-6.35	-8.53	-8.60	-8.64
2.90	-6.31	-4.15	-9.21	-6.00	-6.30	-8.27	-8.30	-8.35
3.00	-6.24	-4.24	-8.87	-5.93	-6.23	-8.03	-8.02	-8.07

Table 4.18. $NICS_{zz}$ values for unfused PDI systems. Distance represents how far in angstroms the ghost atom is located from the plane of the ring. Values are in ppm.

Distance (Å)	C	Si	N	P	As	O	S	Se
0.00	19.44	21.48	0.13	12.48	21.85	-0.13	-0.44	3.89
0.10	18.64	21.27	-0.93	12.41	21.80	-0.38	-0.88	3.35
0.20	16.90	20.46	-3.18	11.53	20.90	-2.00	-2.29	1.80
0.30	14.39	19.11	-6.26	9.94	19.22	-4.69	-4.49	-0.56
0.40	11.38	17.32	-9.73	7.79	16.91	-8.01	-7.17	-3.43
0.50	8.13	15.20	-13.14	5.30	14.17	-11.47	-10.01	-6.52
0.60	4.90	12.87	-16.15	2.66	11.21	-14.63	-12.72	-9.53
0.70	1.90	10.49	-18.52	0.09	8.23	-17.21	-15.07	-12.23
0.80	-0.74	8.16	-20.15	-2.28	5.39	-19.05	-16.92	-14.46
0.90	-2.92	5.99	-21.06	-4.33	2.80	-20.14	-18.22	-16.15
1.00	-4.64	4.03	-21.32	-6.01	0.56	-20.55	-18.97	-17.30
1.10	-5.91	2.33	-21.05	-7.30	-1.33	-20.39	-19.24	-17.93
1.20	-6.79	0.89	-20.38	-8.24	-2.84	-19.79	-19.09	-18.13
1.30	-7.33	-0.29	-19.43	-8.85	-4.02	-18.90	-18.63	-17.96
1.40	-7.61	-1.24	-18.30	-9.19	-4.90	-17.80	-17.93	-17.52
1.50	-7.69	-1.99	-17.09	-9.31	-5.52	-16.61	-17.08	-16.88
1.60	-7.62	-2.57	-15.85	-9.27	-5.93	-15.38	-16.13	-16.10
1.70	-7.44	-3.00	-14.63	-9.10	-6.17	-14.16	-15.15	-15.25
1.80	-7.19	-3.31	-13.47	-8.84	-6.28	-13.00	-14.15	-14.35
1.90	-6.90	-3.53	-12.37	-8.52	-6.29	-11.91	-13.18	-13.45
2.00	-6.59	-3.67	-11.35	-8.16	-6.22	-10.89	-12.25	-12.57
2.10	-6.26	-3.76	-10.42	-7.78	-6.10	-9.97	-11.37	-11.72
2.20	-5.95	-3.79	-9.58	-7.40	-5.94	-9.13	-10.55	-10.92
2.30	-5.64	-3.79	-8.81	-7.03	-5.75	-8.38	-9.79	-10.16
2.40	-5.34	-3.77	-8.13	-6.66	-5.55	-7.70	-9.09	-9.46
2.50	-5.06	-3.72	-7.51	-6.31	-5.34	-7.10	-8.45	-8.81
2.60	-4.80	-3.66	-6.96	-5.98	-5.13	-6.56	-7.87	-8.21
2.70	-4.56	-3.59	-6.47	-5.67	-4.93	-6.08	-7.34	-7.66
2.80	-4.34	-3.51	-6.03	-5.38	-4.73	-5.65	-6.86	-7.16
2.90	-4.14	-3.43	-5.63	-5.10	-4.54	-5.28	-6.42	-6.70
3.00	-3.95	-3.35	-5.28	-4.85	-4.35	-4.94	-6.03	-6.29

respectively, while selenium had a maximum value at 1.60 Å. One observed trend is that as the heteroatom tends to get larger, such as moving down the chalcogen column from oxygen to selenium, the distance needed for the maximum $NICS_{zz}$ value get larger.

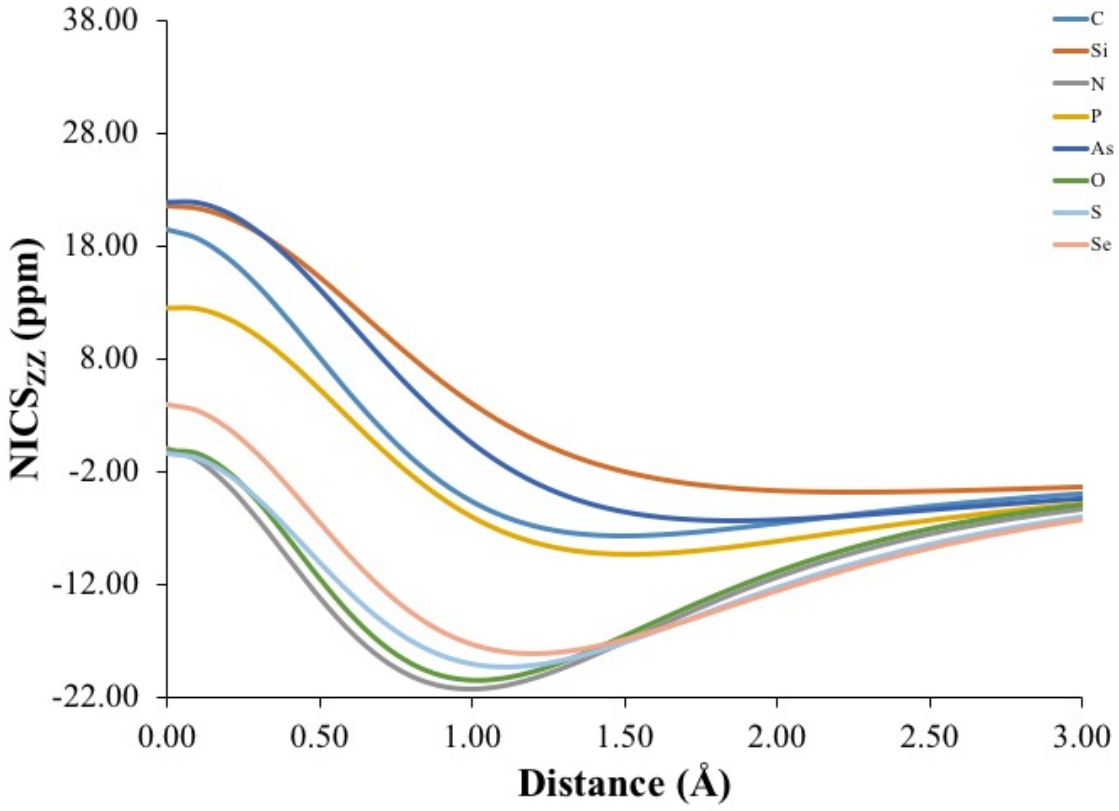

Figure 4.11. The change in the $NICS_{zz}$ value in unfused PDI systems as the distance of the ghost atom from the plane of the ring increases from 0.00 Å to 3.00 Å.

The unfused systems had similar results with oxygen, nitrogen, sulfur and selenium being clearly aromatic, and the others being split between non- and anti-aromatic. One difference in these classifications is arsenic and carbon flipped positions, with carbon now being closer to phosphorus and being slightly non-aromatic. Also, the aromatic species have larger $NICS_{zz}$ values compared to the fused systems. Much like for the fused systems, the 1.00 Å distance was close to the max for each aromatic ring, however, this time

selenium is not considered an outlier. Oxygen, nitrogen and sulfur had maximum $NICS_{zz}$ values at distances of 1.00, 1.00, and 1.10, respectively, while for selenium the max $NICS_{zz}$ was at a distance of 1.20 Å. Due to both fused and unfused systems having maximum $NICS_{zz}$ values around the 1.00 Å distance, and shallow sloped minima in their peaks, the conventional $NICS(1)_{zz}$ should be referenced for future work.

Up until now all values have been the $NICS_{zz}$, but the isotropic value ($NICS(0)_{iso}$) is also considered a valuable NICS value, so Table 4.19 displays the isotropic and $NICS(1)_{zz}$ values for each system. It is important to note that isotropic values are generally smaller than the ZZ values, however the same principles apply when assessing the aromaticity. The isotropic values maintained the same aromatic classifications that were revealed in the $NICS_{zz}$ analysis, however the unfused arsenic system seemed more aromatic, and the fused phosphorus system is more non-aromatic than anti-aromatic. In relation to the photovoltaic data for each of these systems, it appears that the aromaticity of the bridge unit has no effect on the electron transfer rates or k_{CT}/k_{CR} ratio.

Table 4.19. NICS data for unfused and fused PDI systems. $NICS(0)_{iso}$ uses the isotropic shielding value, and $NICS(1)_{zz}$ uses the z-direction shielding. Values are in ppm.

	Unfused		Fused	
System	$NICS(0)_{iso}$	$NICS(1)_{ZZ}$	$NICS(0)_{iso}$	$NICS(1)_{ZZ}$
C	-1.17	-4.64	3.48	6.63
Si	1.91	4.03	5.07	15.74
N	-9.89	-21.32	-10.24	-21.77
P	-3.98	-6.01	0.50	6.59
As	-2.36	0.56	2.46	9.02
O	-8.88	-20.55	-7.00	-13.66
S	-11.56	-18.97	-8.44	-12.62
Se	-11.53	-17.30	-6.93	-9.01

4.5 Conclusion

Firstly, this study determined that the HSE06 functional accurately calculates the ground and excited state energies of PDI dimers. It vastly outperformed B3LYP in determination of the LUMO and E_g energies. This study has demonstrated that for almost all measured variables, the fused systems outperformed their unfused counterparts. Silicon is most likely the heteroatom substitution to provide the best PCE. This is due to having a higher V_{OC}, stronger and more broad absorption peak, and providing one of the fastest charge transfer rates for both fused and unfused systems. Silicon also has one of the largest k_{CT}/k_{CR} ratios for both systems, proving it could effectively perform exciton dissociation. Compared to the previously studied fused chalcogen systems, all other fused system substitutions resulted in increased V_{OC} due to an increase in the LUMO energy, while still maintaining acceptable ΔE_{L-L} values. They also, on average, feature slower rates of recombination, and, in most cases, faster rates of charge transfer. This led to larger k_{CT}/k_{CR} ratios, showing these other substitutions could provide larger J_{SC} and FF values. More specifically, this study illuminates the potential other large atoms, such as silicon and phosphorus, have as heteroatom substitutions in PDI dimers. It was also found that their was no trend between the aromaticity of the bridge unit, and the photovoltaic properties. Future studies should test these PDI systems with other donor molecules to see if the trends continue as the donor molecule changes, and also, investigate multi-substituted heterocyclic structures and learn if these trends can be enhanced by increasing the number of heteroatoms. Another area to further investigate would be to compare the NICS values of the bridge systems with and without being bonded between two PDI units and observe the change in the NICS values.

4.6 Acknowledgements

This work is supported by the Chemical Sciences, Geosciences, and Biosciences Division, Office of Basic Energy Sciences, Office of Science, U. S. Department of Energy under Award Number DE-SC0010212.

CHAPTER FIVE

Photovoltaic Properties of Multi-Heteroatom Substituted Perylene Diimide Systems

5.1 Abstract

The dimerization of perylene diimde (PDI) with a bridge unit has been of increased interest due to its improved photovoltaic properties over the traditional monomer PDI. Previous work has studied the difference between fused and unfused PDI dimers, and how substituting a different heteroatom into the bridge unit changes the photovoltaic properties. It was then hypothesized that the introduction of multiple heteroatoms could further change these properties. This study investigated the effects of substituting two heteroatoms, one chalcogen and one pnictogen, into the PDI bay-region by the creation of a five-membered ring. Three different bridge units were also tested, starting with thiophene and then also testing both a phosphorus and silicon substituted five-membered ring. The most stable orientation of each PDI unit to the bridge unit was determined to be consistent for each chalcogen, except selenium. The S+P and S+As heteroatom combinations were non-planar for each bridge system, while the Se+P combination in the thiophene bridge, and O+N combination for the phosphorus and silicon-bridged systems, were also non-planar. There were HOMO energy fluctuations, while the LUMO remained relatively constant, leading to a consistent decrease in the band gap when moving down the pnictogen column, and an increase when the heteroatom of the bridge unit increased in atomic number. There was also broadening of the absorption spectra as atomic number of the bridge heteroatom decreased. All combinations using oxygen for the silicon-bridged system had very broad

absorption bands, almost covering the entire visible light spectrum. For the charge transfer properties, the main trend observed was the k_{CT}/k_{CR} ratio, which increased by a minimum of about 10^4, and in one case 10^8. This is mostly attributed to the ΔG, and therefore, the HOMO/LUMO energies. Overall, the S+P and S+As heteroatom combinations exhibited the most promise for photovoltaic applications.

5.2 Introduction

Among the newest generation of solar cells, organic solar cells (OSC) have emerged and have become popular because of their unique advantages for specific applications. OSC's can be created using solution processing of low-cost, environmentally friendly materials, and are also flexible, lightweight, and semi-transparent.[52] Also, time needed to recover the energy used to fabricate the device, known as energy payback time, is substantially shorter than conventional silicon-based solar devices.[191] Power conversion efficiency (PCE) is the main measurement to determine the viability of a solar cell, and is the primary focus of OSC research. The largest efficiency achieved for an OSC was achieved in 2018 utilizing a tandem OSC, which utilizes two active layers, and achieved an efficiency of 15%.[66]

The most efficient OSC devices utilize a bulk-heterojunction (BHJ), which is a blend of donor and acceptor materials throughout the active layer. Most OSCs have been designed around a fullerene acceptor, which debuted in 1995, due to efficient charge separation and the ability to transport electrons in three dimensions.[32, 145-146] However, fullerenes have many shortcomings, including difficulty in tuning the electronic properties, high cost of production, and questionable long-term stability.[54, 147] Non-fullerene replacements, such as perylene diimide (PDI),[17] have improved stability and easily tuned

molecular energy levels and absorption spectra, while also having a significantly lower production cost.[64] Early on, OSCs using PDI suffered from low efficiencies due to aggregation of PDI molecules, and phase separation from the donor polymer due to strong π-π stacking.[148] Nonplanar PDI molecules were developed to combat this issue by the dimerization of PDI either with, or without, a bridge unit.[64, 149-153] These dimerized PDI systems have had much success as acceptors in OSCs.

Lately, the most efficient OSCs utilize a polymer as the donor molecule, which has led to them being extensively researched in order optimize their photovoltaic properties.[157] This research has been primarily focused on optimizing molecular energy levels to match a wide variety of acceptors, broadening and red-shifting the absorption band, and increasing hole mobility.[158] One of the polymers seen in high efficiency cells is PBDT-TS1, and will be used as the donor molecule for this study.[160] This polymer is based on a benzo[1,2-b:4,5-b']dithiophene (BDT) backbone. The BDT unit gained traction due to it being easily tunable, it features high hole mobility, and can be readily synthesized. The substitution of 2-alkylthienyl to BDT improved the photovoltaic efficiencies, and eventually led to the PBDT-TS1 polymer.[159]

The use of theoretical calculations has played important role in the field of photovoltaics. Throughout the years computational techniques have deepened the understanding of the underlying mechanisms involved that determine device efficiency. Also, theoretical publications have been at the forefront in the development of novel donor and acceptor molecules.[116, 161-163] For example, using theory can provide a guideline for the design of dye molecules, leading to a rational synthesis and thus avoiding expensive trial-

and-error attempts. Also, using computational methods allows one to rapidly screen dye molecules and gauge their potential in an OSC.

Unfortunately, a purely ab initio approach cannot be used to accurately calculate the PCE (=$V_{OC}J_{SC}FF$ / Pin) of an OSC. There are, however, approximations that can be made to gauge how the main factors that contribute to PCE (i.e. short-circuit current density (J_{SC}), open-circuit voltage (V_{OC}) and fill factor (FF)) are affected by results from ab initio studies. One approximation for the V_{OC} is the energy gap between the highest occupied molecular orbital (HOMO) of the donor and lowest occupied molecular orbital (LUMO) of the acceptor. As the energy gap between these orbitals increases, so does the V_{OC}. Another approximation is by tuning the band gap of the donor molecule to more closely match the solar spectrum and boost J_{SC}. Also, the energetic driving force ($\Delta E_{L\text{-}L}$), which is the LUMO energy difference between donor and acceptor should be greater than 0.3 eV to overcome coulombic attraction and allow efficient charge separation.[144] The two main processes at the D/A interface are intermolecular charge transfer (CT) and charge recombination (CR). To increase the effective exciton dissociation, and also improve J_{SC} and FF, the rate of charge transfer (k_{CT}) should be as high, while keeping the rate of charge recombination (k_{CR}) at a minimum. This can be analyzed using a ratio between the charge transfer and charge recombination rates for each system (k_{CT}/k_{CR}).

The aim of this study is to investigate the role that multiple heteroatoms can play in the photovoltaic properties of PDI dyes. The PDI dimers used here are a hybrid between the fused and unfused systems studied previously in Chapter Four. A thiophene ring was used as the bridge unit for all the initial calculations, and then silicon and phosphorus substituted 5-membered rings were used for further comparisons. These other two ring

systems were chosen due to their positive characteristics observed in Chapter Four, and also to compare heteroatoms along the 3rd row of the periodic table. Another 5-membered ring, this time fused to each PDI unit, was substituted with a pair of different heteroatoms, with one always being a chalcogen and the other a pnictogen. Figure 5.1 shows the chemical structure of the PDI dimer being studied. From left to right it shows the cis-pnictogen (cis-Pn), trans, and cis-chalcogen (cis-Ch) orientations. The X=N and Y=S system has already been characterized by Shi et al.,[192] but to our knowledge, none of the other combinations have been studied.

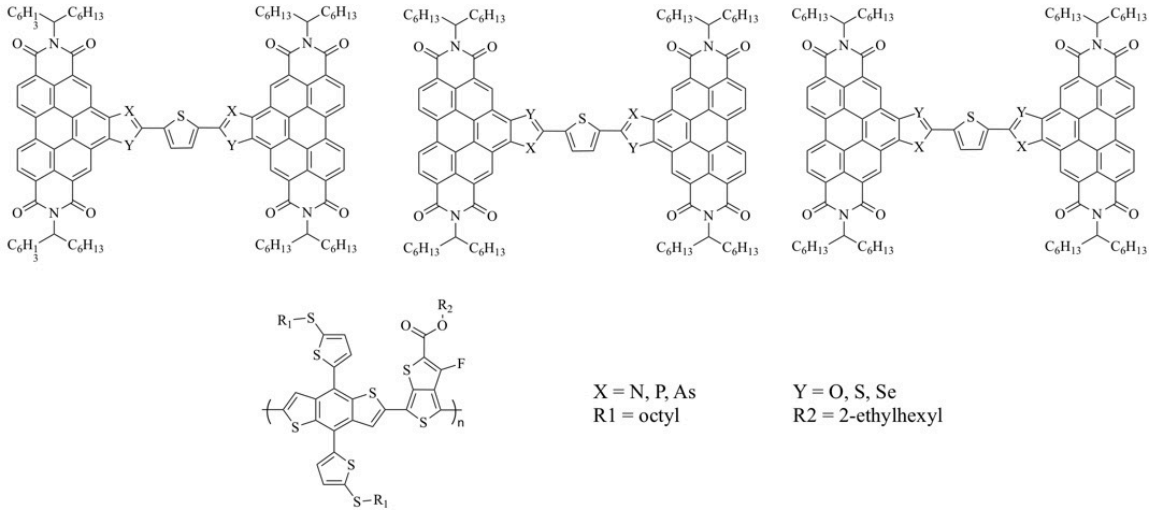

Figure 5.1. Chemical structures of the multi-heteroatom PDI structures and the n=1 PBDT-TS1 donor polymer.

First, the ground state energies will be calculated for each possible orientation shown in Figure 5.1 to determine the most stable orientation. Next, the molecular orbital energies and UV spectra will be calculated, from which the photovoltaic properties will be determined. A charge transfer complex will then be built using these hybrid PDI dimers and PBDT-TS1 to calculate the electronic coupling. The free energies of charge transfer

and charge recombination, along with the reorganization energy, will be calculated to provide a picture for charge transfer and recombination rates via Marcus theory.

5.3 Methods

All optimization and time-dependent calculations are done using density functional theory (DFT) and utilized the 6-31G(d) Pople basis set which has been shown to yield reliable results for evaluating the photovoltaic properties of OSC systems.[164] Even though similar systems were tested in Chapter Four, the functionals were again tested to verify the most accurate one is being utilized. This was done by using the B3LYP, HSE06, PBE0, ωB97xD and CAM-B3LYP functionals to calculate the ground state and time-dependent properties. After these functional tests, the HSE06 functional was determined to be the most accurate and will be used for the optimization and excited state calculations. All geometry and time dependent calculations were done in gas phase using the Gaussian09 software package.[119] Geometries from Gaussian09 were used in the electron transfer module of NWChem for calculation of the electronic coupling (V_{AB}) using the 6-31+G(d) basis set.[165] The carbon chains branching off the imide ends of PDI, shown in Figure 5.1, are replaced by a methyl group to ease computational expense. The carbon chains impact the solubility and active layer morphology but have little impact on the electronic structure.[166-167]

In determining k_{CT} and k_{CR}, the Marcus rate equation was employed:[95]

$$k = \sqrt{\frac{4\pi^3}{h^2 \lambda k_b T}} |V_{AB}|^2 \exp\left(-\frac{(\Delta G + \lambda)^2}{4\lambda k_b T}\right) \quad (5.1)$$

where ΔG is the Gibbs free energy change, λ is the reorganization energy and V_{AB} is the

electronic coupling between the donor and acceptor. T is the temperature, which is set to 298 K, while k_b and h are the Boltzmann and Planck constants, respectively.

The ΔG of charge recombination and charge transfer are expressed as ΔG_{CR} and ΔG_{CT}, respectively. ΔG is calculated as:[168]

$$\Delta G = E_{IP}(D) - E_{EA}(A) \quad (5.2)$$

where $E_{IP}(D)$ is the ionization potential of the donor, and $E_{EA}(A)$ is the electron affinity of the acceptor. These free energy changes are commonly estimated as the difference in orbital energies,[168] thus for charge recombination, ΔG_{CR} is taken as the donor HOMO energy minus the acceptor LUMO. By employing the Rehm-Weller equation, ΔG_{CT} can be calculated as:[168-169]

$$\Delta G_{CT} = -\Delta G_{CR} - \Delta E_{0\text{-}0} - E_b \quad (5.3)$$

where $\Delta E_{0\text{-}0}$ is the donor's lowest excited state energy (i.e., the excitation energy, E_{exc}, from the donor HOMO to S1). The exciton binding energy, E_b, incorporates the electron-hole Coulomb attraction and can be estimated as the difference between the electronic and optical band gaps.[35, 170] Another important parameter is $\Delta E_{L\text{-}L}$, the energy difference between the LUMO's of the donor and acceptor. A value of ~0.3 eV is considered sufficient for efficient electron injection to occur.[171-172] All of these energies related to the HOMO and LUMO orbitals of the donor and acceptor are visualized in Figure 5.2.

The reorganization energy (λ) is the energy required to reorganize the nuclei from the reactant to product geometries without electron transfer occurring and is approximated using an adiabatic process:[193]

$$\lambda = \left(E_0^* - E_*\right) + \left(E_*^0 - E_0\right) \quad (5.4)$$

Where E_0^* is energy of the ion in the neutral geometry, E_* is the ion in the ionic geometry, E_*^0 is the neutral molecule in its ionic geometry, and E_0 is the neutral molecule in its neutral geometry. The λ for both the acceptor and donor molecules are calculated and added together to get a total λ for the charge transfer calculations.

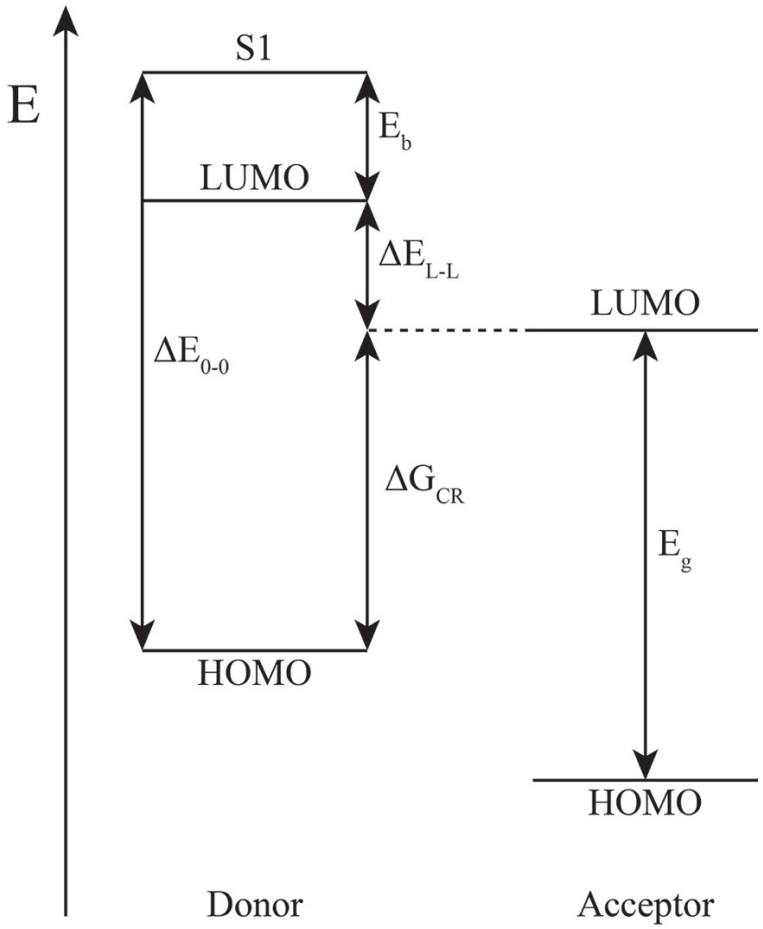

Figure 5.2. Donor and acceptor energy diagram

V_{OC} is an important parameter in calculating PCE of an OSC, and can be estimated by:[179]

$$V_{OC} = \frac{1}{e} \left(|E_{HOMO}(D)| - |E_{LUMO}(A)|\right) - 0.3\ V \qquad (5.6)$$

where $E_{HOMO}(D)$ and $E_{LUMO}(A)$ are the HOMO and LUMO energies of the donor and acceptor, respectively, and e is the elementary charge. The subtraction of 0.3 V is an empirical factor used to more closely represent experimental results, and stems from energy losses during charge transport to the electrodes and various interface effects.[157] This empirical factor should not be confused with the $\Delta E_{L\text{-}L}$ difference of at least 0.3 eV mentioned previously.

When calculating V_{AB} between two molecules in a system, the functional used makes a significant difference, especially the amount of Hartree-Fock exchange involved.[174] However, the trends tend to remain the same regardless, so different systems can be compared as long as the method and functional are kept constant.[175] One of the methods used to calculate the V_{AB} is known as the direct coupling method (DC), known to yield reliable results, and has a low computational cost.[175-177] The NWChem software package includes an electron transfer module, which utilizes Hartree-Fock to compute V_{AB} using the DC method via a 2-state method developed by Farazdel et al.:[178]

$$V_{AB} = \left(1 - S_{AB}^{2}\right)^{-1} \left[H_{AB} - \frac{1}{2} S_{AB}(H_{AA} + H_{BB})\right] \tag{5.5}$$

Where S_{AB} is the overlap integral, H_{AB} the interaction energy, and H_{AA} and H_{BB} the energies of reactant and product dimer states, respectively.

5.4 Results and Discussion

5.4.1 Determination of Most Stable Orientation

There are three possible orientations for the PDI dimer system and can all be related to the sulfur in the thiophene bridge: with both pnictogens, one pnictogen and one chalcogen, or both chalcogens on the same side as the sulfur atom. Keep in mind this is a

single bond between the bridge and each PDI unit, so this can freely rotate between the three orientations. To further understand the most stable orientation for every pnictogen-chalcogen combination, each orientation was optimized. Also, using the fact that it's a single bond linking the bridge and PDI together, we took the trans-orientation and rotated each PDI unit 180°, shown in Figure 5.3.

Using the total energy of each system, the most stable orientation for each combination can be deduced. Table 5.1 shows the ΔE between the most stable orientation and the other two possibilities in kcal/mol for the optimized systems. The cis columns represent that particular atom being cis to the sulfur in thiophene, and trans signifies that one pnictogen and one chalcogen are cis to the thiophene sulfur.

Table 5.1. ΔE between each orientation with the more stable version for each pnictogen-chalcogen combination. Each system utilizes a thiophene bridge between the PDI units. The dash (-) represents which orientation was the most stable.

Ch + Pn	Cis-Ch (kcal/mol)	Cis-Pn (kcal/mol)	Trans (kcal/mol)
O + N	0.482	0.001	-
O + P	0.102	0.636	-
O + As	0.458	0.152	-
S + N	2.095	-	0.709
S + P	0.409	-	0.141
S + As	1.386	-	0.812
Se + N	1.244	-	0.057
Se + P	-	0.454	0.311
Se + As	-	0.220	0.001

For each chalcogen, except for selenium, the most stable orientation was consistent for each pnictogen combination, with the trans system most stable for oxygen,

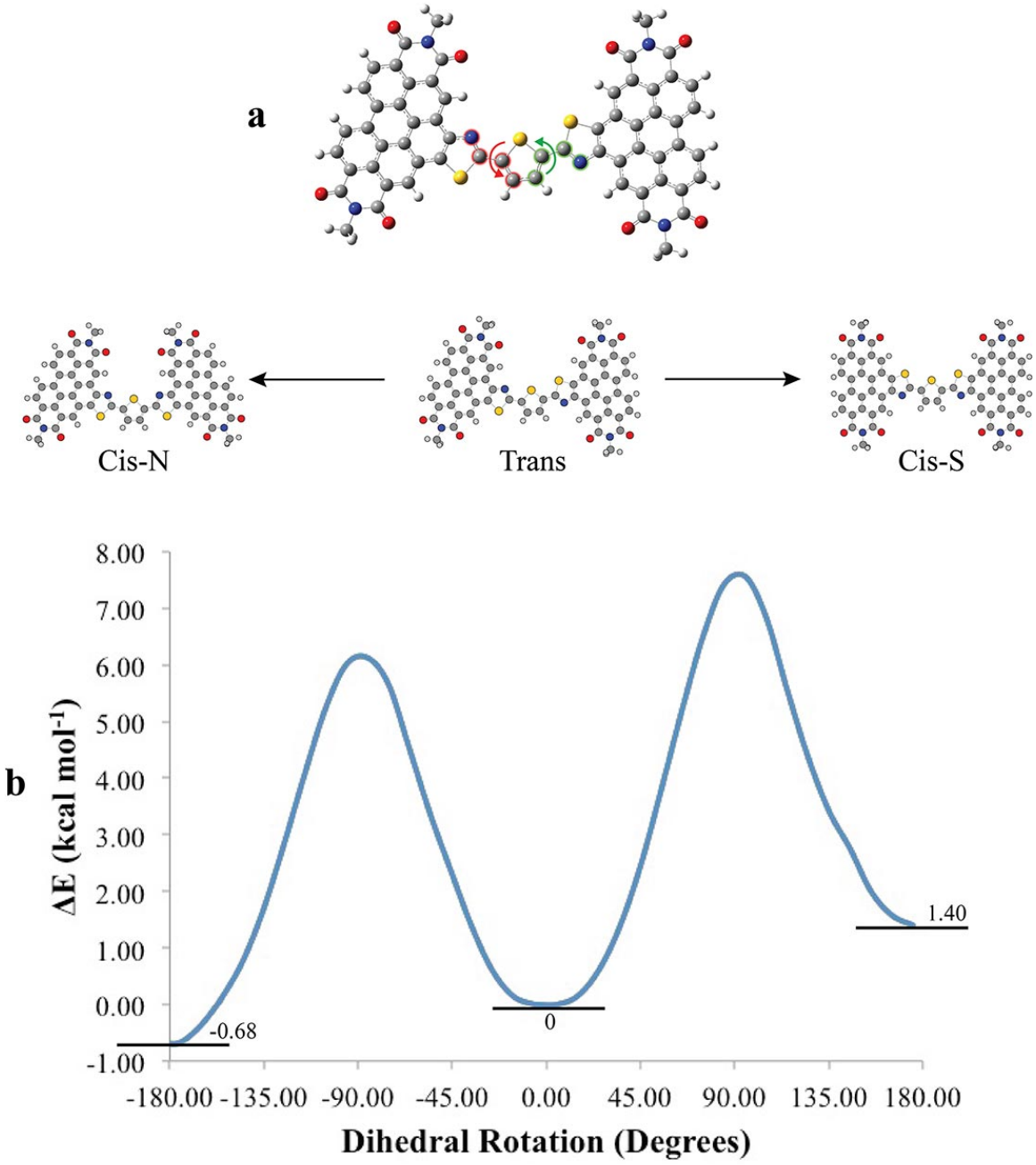

Figure 5.3. Dihedral angles rotated 180° starting from the trans orientation with a) showing the bond and atoms involved in the dihedral and b) illustrating the ΔE in kcal/mol from the trans orientation every 10° around the dihedral. Above the minima are the geometries for the corresponding orientation.

and cis-Pn for sulfur. The selenium systems were split, with cis-Pn being the most stable for the nitrogen system, while the cis-Ch configuration was more stable for phosphorus and arsenic. Shi et al. determined that the cis-Pn orientation was the most stable for the S+N system, and that the cis-Ch and trans orientations were 2.23 kcal/mol and 0.95 kcal/mol higher in energy, respectively. This is consistent with our results, and the small differences in energy are most likely due to their study using B3LYP, and ours HSE06. Keep in mind that in all these cases, except for S+N, S+As and Se+N, the ΔE are less than 1.0 kcal/mol, and even the largest ΔE of 2.095 kcal/mol is not a large energy hurdle between orientations. Also, between the trans and cis-Pn orientations for O+N, and the trans and cis-Ch orientations for Se+As, there is only a 0.001 kcal/mol difference. Nearly identical results are acquired when using the scan function in Gaussian09. The PDI unit is rotated around the single bond linking it to the bridge unit. Figure 5.3 illustrates this rotation around the bond, which is done by rotation of the dihedral between the PDI and bridge unit by 10° increments up to 180°, starting from the trans orientation. Values are plotted together to form a whole picture of the energy between each orientation. This system displays clear minima for the total energy, and that these resulting energies are close to the optimized values found in Table 5.1.

5.4.2 Molecular Orbital Analysis

Table 5.2 shows the HOMO and LUMO energies for each system, while Figure 5.4 illustrates the molecular orbitals for each orientation of the S+N orientations and also shows the molecular orbitals for each heteroatom combination. Throughout all the combinations and possible orientations, the LUMO remained somewhat constant. All possible combinations led to a max difference of ~0.05 eV between orientations. It seems

that the orientation is a larger factor than the heteroatom combination in determining the LUMO energy. This is shown by the cis-Ch staying relatively constant, but cis-Pn was consistently fluctuating. Even though the heteroatoms range from oxygen and nitrogen to selenium and arsenic, the LUMO energy for the cis-Ch orientation was -3.74 eV for a majority of the combinations, and only varied by a maximum of 0.02 eV. To a lesser extent, this same trend can be observed for the trans orientation. The value still hovered around -3.74 eV, but had a larger range of values than the cis-Ch systems, ranging from -3.71 eV to -3.76 eV. cis-Pn saw the largest variations, with a maximum difference of 0.10 eV between the O+P and Se+N combinations.

Table 5.2. HOMO and LUMO molecular orbital energies for each heteroatom combination and their respective orientations. The asterisk (*) represents which orientation was the most stable for that combination, which was determined from Table 5.1 above.

Ch + Pn	HOMO			LUMO		
	Cis-Ch (eV)	Cis-Pn (eV)	Trans (eV)	Cis-Ch (eV)	Cis-Pn (eV)	Trans (eV)
O + N	-5.94	-5.95	-5.95*	-3.74	-3.73	-3.74*
O + P	-5.60	-5.66	-5.62*	-3.74	-3.77	-3.76*
O + As	-5.47	-5.54	-5.49*	-3.72	-3.76	-3.75*
S + N	-5.94	-5.92*	-5.93	-3.74	-3.70*	-3.72
S + P	-5.67	-5.69*	-5.67	-3.74	-3.75*	-3.74
S + As	-5.51	-5.55*	-5.53	-3.74	-3.74*	-3.74
Se + N	-5.92	-5.90*	-5.91	-3.72	-3.67*	-3.71
Se + P	-5.66*	-5.67	-5.66	-3.74*	-3.72	-3.73
Se + As	-5.49*	-5.51	-5.47	-3.73*	-3.74	-3.74

This large range of LUMO energies could be a result of the increased electronegativity of the pnictogen atom being closer to the bridge unit's sulfur atom. When

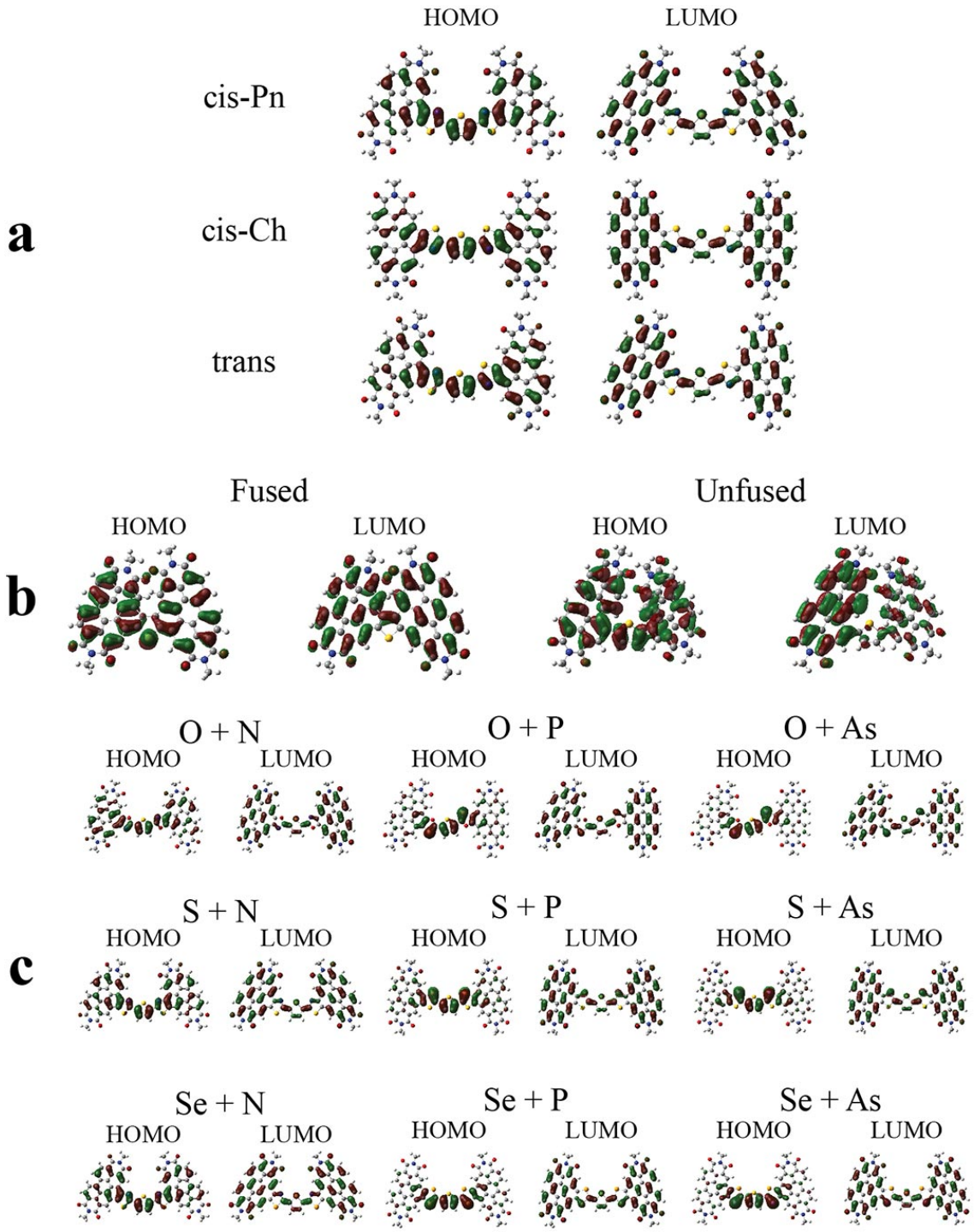

Figure 5.4. HOMO and LUMO orbitals for a) the S+N combination at each orientation; b) each heteroatom combination at the most stable orientation; c) the thiophene bridged fused and unfused PDI dimers for comparison.

moving down the column from nitrogen all the way to arsenic, the LUMO energy became more negative than the original energy for the combination involving nitrogen. When the pnictogen is held constant and the chalcogen is changed, the opposite trend is observed, with the LUMO becoming less negative. This same trend is not observed for the cis-Ch series, and would not be expected for the trans systems since each heteroatom is cis to the thiophene sulfur atom. It can also be observed that the most stable orientation for each system had no effect on the LUMO energy.

Much like the LUMO energies, the HOMO energy levels had little variation between orientations. However, the O+P and O+As combinations had a maximum energy difference of 0.06 eV and 0.07 eV, respectively, between the cis-Ch to cis-Pn orientations. All the other combinations varied by <0.03 eV between orientations. The HOMO energy levels saw more significant changes between heteroatom combinations. Unlike the cis-Ch orientation for the LUMO energies staying relatively constant, the HOMO energies were constantly changing, with a maximum difference of 0.43 eV. In every heteroatom combination and orientation, as the pnictogen atom got larger, the HOMO was energy was raised significantly, becoming less negative. The same trend occurred, to a much lesser extent, when nitrogen was held constant, and the chalcogen was changed. For phosphorus, the opposite is observed, where the HOMO energy became more negative than the oxygen system when moving down the chalcogen column.

With the HOMO undergoing large changes in energy, and the LUMO remaining relatively constant, the band gap also decreases as the pnictogen gets larger, shown by Table 5.3. Even though the HOMO energy of the acceptor molecule doesn't have much of a role for charge transfer between the donor and acceptor, its increase is directly affecting

the band gap. This consistent change in the band gap shows promise in the idea of tailoring PDI dimers to have complimentary energies with a variety of donor molecules.

Table 5.3. The HOMO-LUMO energy gap (E_g) for each heteroatom combination and orientation. The asterisk (*) represents which orientation was the most stable for that combination, which was determined from Table 5.1.

Ch + Pn	Cis-Ch (eV)	Cis-Pn (eV)	Trans (eV)
O + N	2.20	2.22	2.21*
O + P	1.86	1.89	1.87*
O + As	1.75	1.77	1.74*
S + N	2.20	2.23*	2.21
S + P	1.93	1.94*	1.93
S + As	1.77	1.81*	1.79
Se + N	2.20	2.22*	2.20
Se + P	1.92*	1.94	1.93
Se + As	1.75*	1.77	1.73

There is little difference in the electron delocalization between the various heteroatom combinations, even though the molecular orbital energies, and therefore, the band gaps, are changing. This shows that the energies can be customized to a particular donor molecule, while still retaining the delocalization normally found in dimerized PDI systems. Compared to the previously studied fused and unfused PDI dimers, these multiple heteroatom species maintain the positive characteristics, while also improving on other properties. Figure 5.4b shows the molecular orbitals for thiophene fused and unfused systems for comparison, and Figure 5.4c shows all the heteroatom combinations studied here with the thiophene bridge. The HOMO orbitals for all the heteroatom systems, except the ones with nitrogen, tend to be localized around the bridge region, however, this is not an issue, since it is the LUMO orbital that participates in the electron transfer event with

the donor molecule. Compared to the unfused systems (Figure 5.4b), which these new PDI dimers closely resemble, the LUMO is delocalized more evenly between each PDI unit, which is increasing the area which an electron can be injected. Also, the LUMO orbitals appear to be symmetrical between the two PDI units, unlike the unfused systems which can have more density on one unit than the other.

5.4.3 Absorption Spectra

Even though the total energies for each orientation are relatively close to each other, the UV/Vis spectrum should be calculated to identify possible differences. Table 5.4 shows the λ_{max} values for each combination, organizing them by both constant chalcogen, and constant pnictogen. Figure 5.5a shows the UV/Vis spectra of all the heteroatom

Table 5.4. The λ_{max} values for each combined heteroatom species with a thiophene bridge, organized by when the chalcogen or pnictogen is held constant. λ_{max} signifies the wavelength at the global maximum, and $\Delta\lambda_{max}$ shows the change in wavelength between that combination and the heteroatom at the top of its respective column.

Constant Chalcogen			Constant Pnictogen		
Ch + Pn	λ_{max} (nm)	$\Delta\lambda_{max}$ (nm)	Pn + Ch	λ_{max} (nm)	$\Delta\lambda_{max}$ (nm)
O + N	434	-	N + O	434	-
O + P	476	42	N + S	450	16
O + As	490	56	N + Se	454	20
S + N	450	-	P + O	476	-
S + P	490	40	P + S	490	14
S + As	508	58	P + Se	518	42
Se + N	454	-	As + O	490	-
Se + P	518	64	As + S	508	18
Se + As	526	72	As + Se	526	36

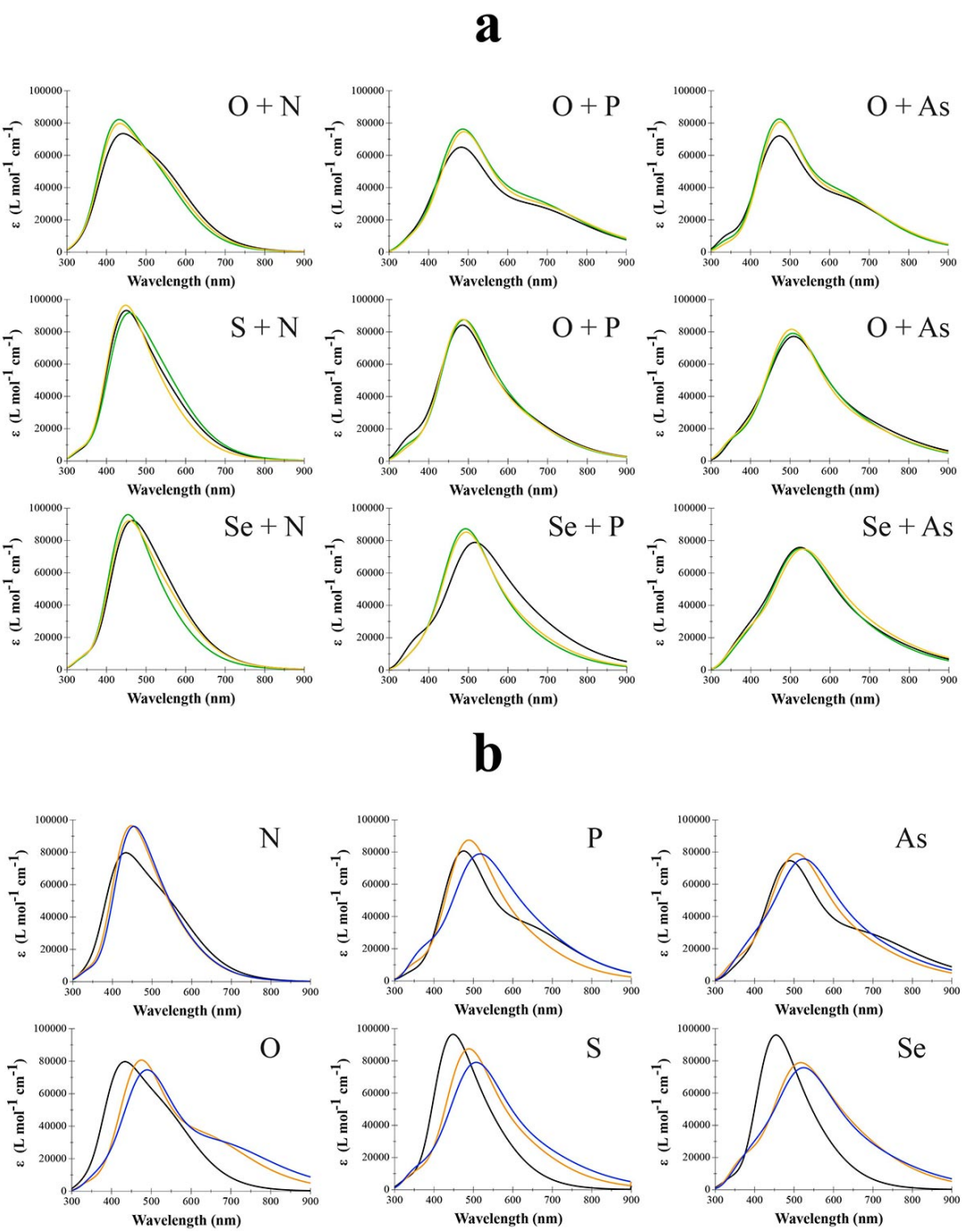

Figure 5.5. UV/Vis spectra for a) each orientation of all heteroatom combinations where the black, green and gold lines represent the cis-Ch, cis-Pn, and trans orientations, respectively. Panel b) the most stable orientation when holding the specified atom constant, where the black, orange and blue lines represent the second, third and fourth row heteroatoms, respectively.

combinations in each possible orientation, and Figure 5.5b combines the spectra for the most stable orientations to observe trends within the chalcogens or pnictogens.

In all of the sulfur and selenium combinations, the change in orientation made little difference in the UV/Vis absorbance, except the selenium and phosphorus showed a slight difference in the cis-Ch orientation. For all the systems using oxygen, the cis-Ch orientation resulted in the lower absorbance band compared to the other possibilities, much like the selenium and phosphorus combination. Even with these few exceptions, the absorbance spectra for all systems are close enough to consider negligible differences. It is clear throughout the total energies, molecular orbital energies, and UV/Vis spectra, that the orientation has little effect on the electronic and optical properties of the dye. From now on, data for the most stable orientation will be used for future calculations.

The strongest absorptions in Figure 5.5b are from nitrogen combined with either sulfur or selenium, which both have extinction coefficients of ~100,000 L mol^{-1} cm^{-1}, ~25% larger than most other combinations. The only other combination that exceeded an extinction coefficient of 80,000 L mol^{-1} cm^{-1} was the S+P combination. For each of the pnictogens, the combination with sulfur had the largest absorption, except for the N+Se combination, which had a nearly identical absorption to the N+S combination. In the constant chalcogen cases, the absorption trends downward when moving down the pnictogens. The only exception is that the O+P combination exhibits increased absorption compared to the O+N combination. Further inspection reveals that even though only a few cases have a much higher extinction coefficient, there is significant red-shift occurring. For both the chalcogens and pnictogens, the UV/Vis spectra red-shifted when moving down each column.

There was a much larger red-shift between the second and third row elements, except when going from sulfur to selenium when paired with phosphorus or arsenic. Also, the pnictogens appear to have a larger effect on the red-shifting of λ_{max}. The smallest red-shift while keeping the chalcogen constant was 40 nm, which was only 2 nm off from the maximum when the pnictogen remained constant. By utilizing elements from the third row of the periodic table, the λ_{max} can be red-shifted upwards of 50 nm. This also shows that by utilizing different heteroatom combinations, the absorption spectrum of an acceptor dye can be tuned to be complimentary to a donor molecule, thus increasing solar cell efficiency.

Figure 5.6 shows the S+N, O+P, and also the fused and unfused PDI dimers bridged by thiophene studied in Chapter Four. It is readily observed that these multi-substituted

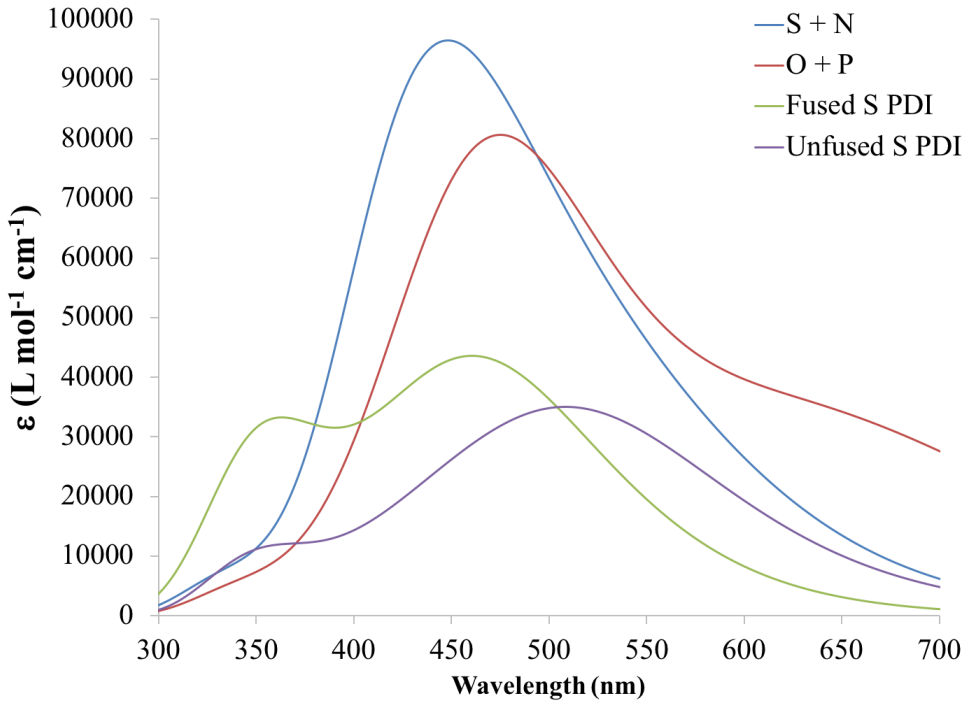

Figure 5.6. UV/Vis spectra of the S+N (blue) and O+P (red) heteroatom combinations bridged by thiophene, along with the fused (green) and unfused (purple) PDI systems also bridged by thiophene.

heteroatom species also exhibit significantly stronger UV/Vis absorptions compared to the previously studied fused and unfused PDI dimers. These combined heteroatom systems have much larger extinction coefficients, showing that they can be more adept absorbers in the visible region. The main contributor to the broadness of the absorption spectra of these multi-substituted systems, is a strong HOMO to LUMO transition. This is unlike the fused and unfused species previously studied, which were dominated by transitions originating from, or ending at, the HOMO-1 or LUMO+1, respectively.

Throughout every combination, whether the chalcogen or pnictogen is held constant, as the heteroatoms increased in size, the λ_{max} red-shifted. Figure 5.7 plots the atomic size of each heteroatom combination with the corresponding λ_{max}, showing a positive correlation with a R^2=0.67939.

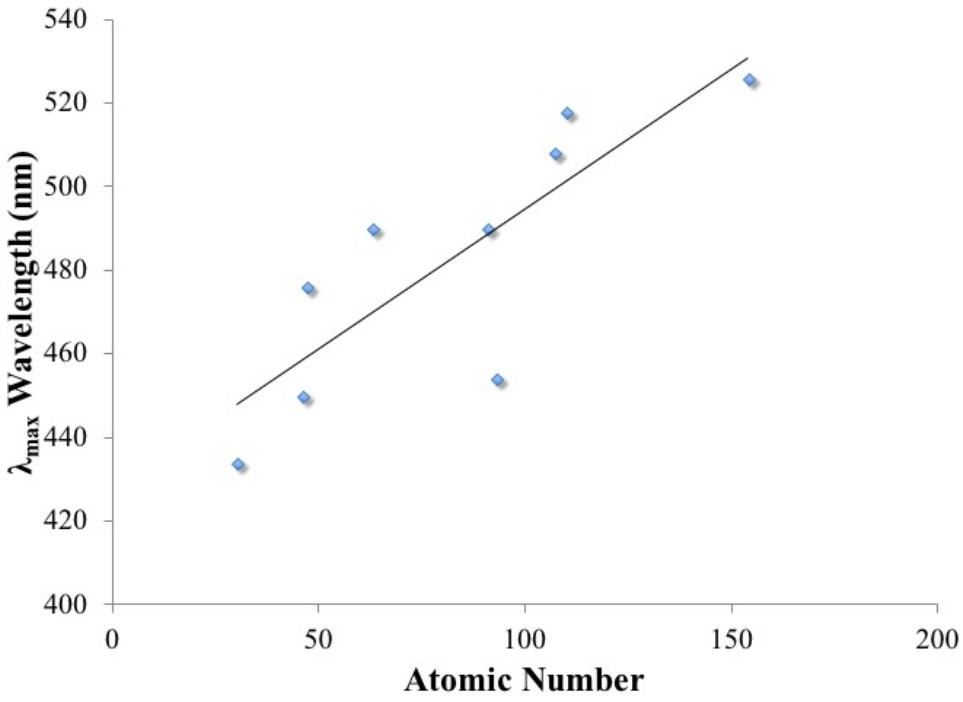

Figure 5.7. Atomic number of the combined heteroatoms plotted against their corresponding λ_{max} wavelength. The R^2 value for the trendline is 0.67939.

5.4.4 Planarity Measurements

The planarity of PDI has been an issue affecting solar efficiencies, which is due to the π-π stacking between PDI units. This led to the use of PDI dimers because of their tendency to break this planarity, but still retain the molecular orbital delocalization. The dihedral angles between the bridge unit and PDI units are shown in Table 5.5. Most systems

Table 5.5. Dihedral angles between the thiophene bridge and each PDI unit for all heteroatom combinations and orientations. The dashes (-) signify the system was planar. Units are in degrees (°).

Ch + Pn	Cis-Ch (°)	Cis-Pn (°)	Trans (°)
O + N	-	-	-*
O + P	7.92 / 7.92	-	-*
O + As	-6.32 / -6.32	-	-*
S + N	-	-*	-4.77 / -5.64
S + P	-	12.75 / 12.72*	-
S + As	15.41 / 15.41	10.83 / 10.69*	19.15 / -13.65
Se + N	-5.46 / -5.45	-*	-
Se + P	4.40 / -4.73*	-	18.79 / -20.05
Se + As	-*	-	-

had completely planar PDI units, while all the S+As orientations had dihedrals >10°. The two systems with the largest UV/Vis absorptions, S+N and Se+N, only had a small amount of distortion in their planarity, and it was not for their most stable orientation. Due to the small energy differences between states, it can be assumed that any of the orientations are possible, however, the dihedrals are small for the orientations with distortion. Due to their planarity, it is reasonable to assume they will be plagued by the same problems with other planar PDI systems.

The only systems where the most stable orientation had distortion in the planarity are the S+P, S+As and Se+P combinations. For the O+N and Se+As systems, all of the orientations were planar, while five other combinations only had one nonplanar orientation. The S+P and S+As systems both had dihedrals >10° for their most stable orientation, while Se+P had the largest dihedral of -20.05°, however, it wasn't for its most stable orientation. It can also be seen that there is no correlation between the planarity of the system and its stability. These three systems exhibit decreased band gaps, red-shifted absorption spectra, and greater distortions in their planarity compared to the already synthesized S+N system. These three systems also have negligible change in the LUMO energy compared to S+N, so similar donor molecules can be paired with the dye, and the V_{OC} will be relatively unchanged, even though other properties have been improved.

5.4.5 Changing the Bridge Unit

The next step was to change the bridge unit for these systems. In previous work, our results gave evidence that utilizing bridge groups with phosphorus or silicon could improve OSC efficiencies. The insights gained from Chapter Four on fused and unfused PDI dimers were then applied to these multiple heteroatom structures, so instead of thiophene, phosphorus and silicon five-membered rings will be tested as the bridge unit.

5.4.5.1 Determination of most stable orientation. Each PDI dimer using the new bridge unit were optimized at each of the three possible orientations, similar to the thiophene bridge. Table 5.6 shows the most stable orientation for each system. Much like for the thiophene bridge, the oxygen and sulfur systems are consistent on which orientation is the most stable, however, this time both were determined to be most stable at the cis-Pn

Table 5.6. ΔE between each orientation with the more stable version for each pnictogen-chalcogen combination using a silicon or phosphorus substituted bridge. The dash (-) represents which orientation was the most stable.

	Si			P		
Ch + Pn	Cis-Ch (kcal/mol)	Cis-Pn (kcal/mol)	Trans (kcal/mol)	Cis-Ch (kcal/mol)	Cis-Pn (kcal/mol)	Trans (kcal/mol)
O + N	1.325	-	0.821	0.803	-	0.337
O + P	1.327	-	0.672	0.595	-	0.199
O + As	3.274	-	1.563	2.000	-	0.885
S + N	3.459	-	1.427	2.526	-	1.041
S + P	2.947	-	1.498	1.111	-	0.611
S + As	5.928	-	3.090	3.122	-	1.572
Se + N	1.660	-	0.461	1.024	-	0.114
Se + P	-	0.159	0.001	-	1.228	0.519
Se + As	2.727	-	1.273	0.488	-	0.140

orientation. Also, for the selenium systems, there were two combinations most stable in the cis-Pn orientation, and one more stable in the cis-Ch orientation, which is the opposite of the thiophene bridged systems. One thing to note is that there were only three instances where the ΔE>1.000 for the thiophene bridged systems, while the phosphorus and silicon bridged systems had eight and thirteen instances, respectively. Even though these are still fairly small values, it shows that these systems may be much more decisive in staying at their most energetically stable orientation.

5.4.5.2. Molecular orbital energies. It was shown in Table 5.2 that there was a negligible difference in molecular orbital energies between orientations, so the HOMO and LUMO energies are presented for the most stable orientations in Table 5.7. The same trends occur as the thiophene bridged system, where the HOMO energy increases as the pnictogen atom increased in size, and the LUMO remained largely unchanged. It is important to note

Table 5.7. HOMO and LUMO energies for the most stable orientation of each heteroatom combination when using a five-membered ring with a phosphorus or silicon heteroatom. For comparison, the thiophene bridge data is also displayed and is referred to as "S" in this case.

	Si		P		S	
Ch + Pn	HOMO (eV)	LUMO (eV)	HOMO (eV)	LUMO (eV)	HOMO (eV)	LUMO (eV)
O + N	-5.90	-3.83	-5.92	-3.78	-5.95	-3.74
O + P	-5.57	-3.85	-5.60	-3.81	-5.62	-3.76
O + As	-5.43	-3.85	-5.47	-3.81	-5.49	-3.75
S + N	-5.87	-3.79	-5.88	-3.74	-5.92	-3.70
S + P	-5.60	-3.81	-5.63	-3.76	-5.69	-3.75
S + As	-5.46	-3.81	-5.50	-3.76	-5.55	-3.74
Se + N	-5.86	-3.79	-5.86	-3.73	-5.90	-3.67
Se + P	-5.55	-3.84	-5.62	-3.76	-5.66	-3.74
Se + As	-5.42	-3.80	-5.46	-3.75	-5.49	-3.73

that all the combinations except Se+P were most stable in the cis-Pn orientation, which had the most fluctuation in the thiophene bridged systems. Therefore, this is still consistent with the thiophene system, and changing the bridge unit between PDI units does not change these HOMO/LUMO trends. It should also be noted that the silicon and phosphorus-bridged systems have delocalized systems similar to the thiophene-bridged PDI systems. It can be assumed that no matter what bridge unit is used, the molecular orbital delocalization and energy trends will remain.

Table 5.8 shows the band gap (E_g) for each heteroatom combination when using the phosphorus or silicon ring bridge, while also displaying the band gap for the thiophene system for comparison. Each of these elements are in the same row of the periodic table,

Table 5.8. A comparison of the electronic band gap (E_g) for each heteroatom combination between different bridge units. The thiophene bridge is referred to as "S" in this case.

Ch + Pn	Si (eV)	P (eV)	S (eV)
O + N	2.07	2.14	2.21
O + P	1.72	1.79	1.87
O + As	1.59	1.66	1.74
S + N	2.08	2.14	2.23
S + P	1.78	1.87	1.94
S + As	1.64	1.73	1.81
Se + N	2.07	2.13	2.22
Se + P	1.71	1.87	1.92
Se + As	1.61	1.71	1.75

and are ordered 14, 15 and 16, for silicon, phosphorus and sulfur respectively. The columns in Table 5.8 are ordered in this way as well, and a clear trend is observed. When moving across the third row of the periodic table, the band gap consistently increases for every heteroatom combination. The largest change in E_g was for the Se+P combination, which resulted in a 0.21 eV increase when going from the silicon to thiophene bridge. The increase in E_g when moving from the silicon to phosphorus bridge for the Se+P system was 0.16 eV, and only one other combination had a total increase in E_g larger than 0.16 eV. The average total increase between all heteroatom combinations was 0.16 eV, with the average increase from silicon to phosphorus, and phosphorus to thiophene, being 0.09 eV and 0.07 eV, respectively. When comparing Table 5.7 to Table 5.8, it is seen that the change in band gap is due to both an increasing LUMO level, and decreasing HOMO level when moving along the third row of the periodic table.

5.4.5.3. Planarity of the system. After investigating the dihedrals for the most stable orientations of the silicon and phosphorus bridged systems (Table 5.9), it was found that most of the systems were planar, and that it was fairly consistent between the phosphorus

Table 5.9. Dihedral angles for the silicon and phosphorus bridged systems in their most stable orientation. Angle is measured between the bridge and PDI units illustrated in Figure 5.3a. Units are in degrees (°).

Ch + Pn	Si (°)	P (°)
O + N	-2.28 / -2.28	7.60 / 1.08
O + P	-	-
O + As	-	-
S + N	-	5.88 / -5.87
S + P	5.78 / 5.80	18.69 / -18.71
S + As	3.98 / 3.97	17.18 / -16.53
Se + N	-	-
Se + P	-	-
Se + As	-	-

and silicon bridged species. More specifically, all the systems utilizing selenium were planar for each orientation, and the only combinations where the most stable orientation was not planar were O+N, S+P and S+As. The S+N system was not planar only for the phosphorus bridged system.

5.4.5.4. Absorption spectra. Figure 5.8 shows the UV/Vis spectra of the PDI dimers utilizing these phosphorus and silicon ring bridges. The spectra for the sulfur systems are also shown for a direct comparison. To no surprise, the same trends observed for the thiophene systems are observed here for the phosphorus and silicon-bridged systems as

well. However, the peaks are not as strong for the phosphorus and silicon-bridged systems, especially for the strong S+N and Se+N peaks seen for the thiophene-bridged systems.

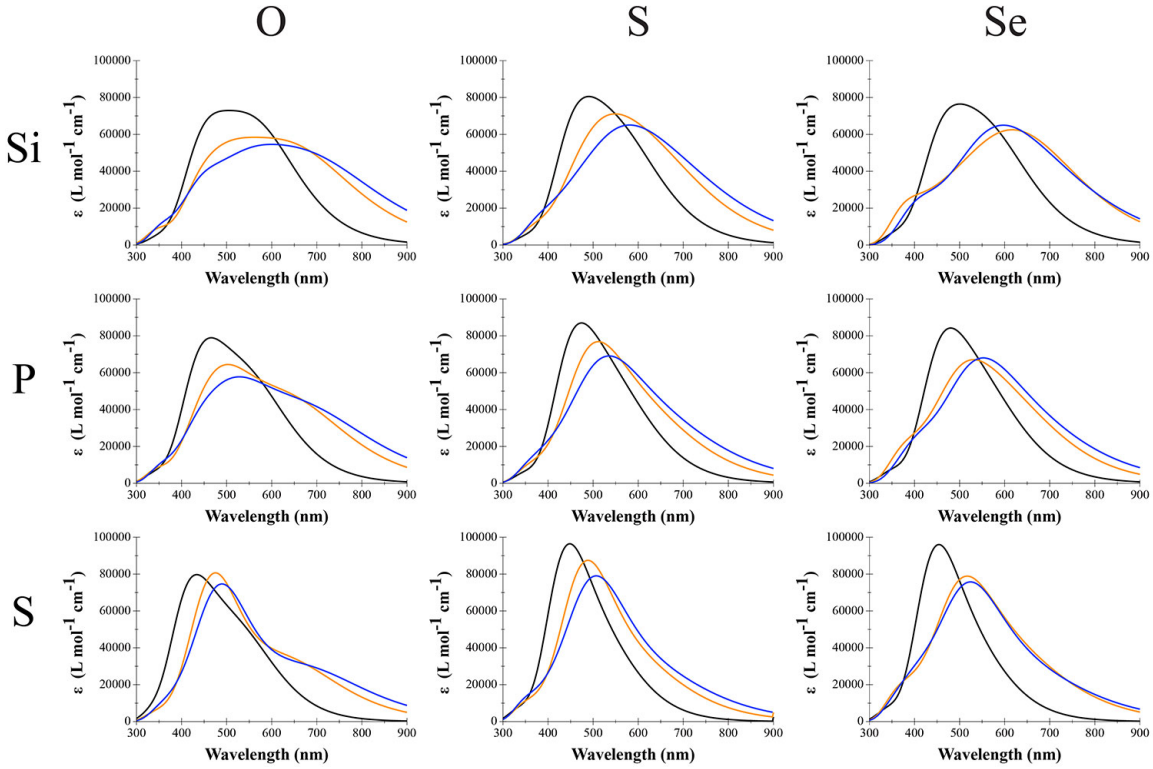

Figure 5.8. UV/Vis spectra for silicon, phosphorus and thiophene bridged systems. The thiophene bridge is referred to as "S" in this case.

Table 5.10 shows the λ_{max} values for each heteroatom combination. Another clear trend can be observed when moving along the third row of the periodic table. When moving from silicon, to phosphorus, to sulfur, λ_{max} decreases by a significant amount. The largest difference is 112 nm for the O+As heteroatom combination when going from silicon to sulfur as the bridge unit. The only other case where the decrease is more than 88 nm is the Se+P combination which involves a decrease in the λ_{max} by 100 nm.

Table 5.10. The λ_{max} values for each combined heteroatom species with each bridge unit studied. The "S" signifies thiophene. λ_{max} is the wavelength at the global maximum, and $\Delta\lambda_{max}$ shows the change in wavelength between that combination and the heteroatom at the top of its respective column.

	Si		P		S	
Ch + Pn	λ_{max} (nm)	$\Delta\lambda_{max}$ (nm)	λ_{max} (nm)	$\Delta\lambda_{max}$ (nm)	λ_{max} (nm)	$\Delta\lambda_{max}$ (nm)
O + N	506	-	466	-	434	-
O + P	564	58	504	38	476	42
O + As	602	96	530	64	490	56
S + N	492	-	476	-	450	-
S + P	550	58	512	36	490	40
S + As	582	90	536	60	508	58
Se + N	502	-	482	-	454	-
Se + P	618	116	532	50	518	64
Se + As	598	96	554	72	526	72

Both the phosphorus and silicon bridge systems exhibit more broad UV/Vis spectra compared to sulfur, especially for the combinations using oxygen. For the oxygen combinations with the silicon bridge, they all have broad and flat peaks. For the O+N combination, it is maintained for ~100 nm between 450-550 nm. The O+P and O+As combinations are even more broad, holding a relatively consistent intensity for ~200 nm, between the range of 500-700 nm. The same characteristics apply to the phosphorus bridged oxygen combinations, but to not as large of a degree. Even though the O+P and O+As systems are planar, the O+N system does contain some distortion, so the broad absorption will add credence to its potential in an actual solar cell. All the combinations involving sulfur, except for the silicon bridged S+N, have broad absorptions and non-planar systems, which shows promise toward their solar cell capability.

5.4.6 D/A Interface and Charge Transfer Properties

The LUMO energies of these PDI dyes are in the same range as the fused and unfused systems studied in Chapter 4, therefore the same donor molecule, the PBDT-TS1 polymer (Figure 5.1), will be used for charge transfer calculations. It was determined in the previous study that even though the electronic coupling values and subsequent transfer rates are susceptible to whether the system was in a pre- or post-optimized state, the k_{CT}/k_{CR} ratio remained the same. Therefore, to save computational cost, the transfer rates were calculated using only the pre-optimized D-A states shown in Figure 5.9. Also, it was shown that increasing the polymer chain length from n=1-3 did not significantly change results, so the n=1 chain length of the PBDT-TS1 polymer will be used for the electronic coupling calculations.

Table 5.11 shows the LUMO-LUMO gap (ΔE_{L-L}) and open-circuit voltage (V_{OC}) values for each heteroatom combination and bridge unit. For all but two systems, the ΔE_{L-L} values are greater than the approximate 0.30 eV driving force threshold. The two outliers are the S+N and Se+N systems combined with the thiophene-bridge, which have ΔE_{L-L} values of 0.30 eV and 0.27 eV, respectively. The silicon and phosphorus bridged systems both have cases where the ΔE_{L-L}>0.40 eV, however, these LUMO-LUMO gaps are coming at the price of the V_{OC}. Much like the molecular orbital energies, which these values are based off, there is a clear trend in the V_{OC} and ΔE_{L-L} when moving along the 3rd row of the periodic table from silicon to sulfur. For every heteroatom combination, the V_{OC} increased,

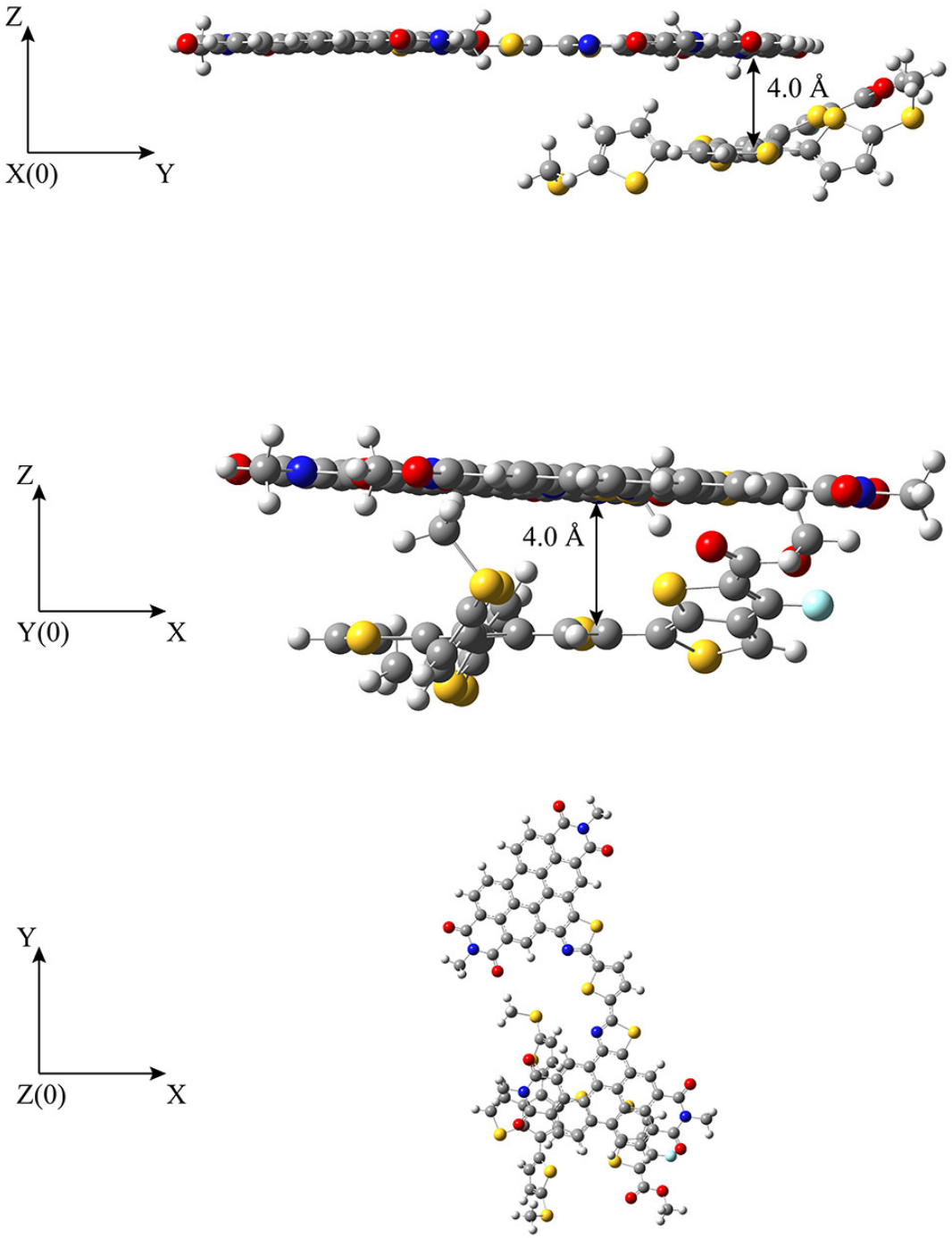

Figure 5.9. Donor-Acceptor orientation in the x, y and z-directions. Alongside each view is an axis, with the (0) designating the perspective.

Table 5.11. LUMO-LUMO gap ($\Delta E_{L\text{-}L}$) and open-circuit voltage (V_{OC}) for each heteroatom combination and bridge unit.

	Si		P		S	
Ch + Pn	$\Delta E_{L\text{-}L}$ (eV)	V_{OC} (eV)	$\Delta E_{L\text{-}L}$ (eV)	V_{OC} (eV)	$\Delta E_{L\text{-}L}$ (eV)	V_{OC} (eV)
O + N	0.43	1.02	0.38	1.07	0.34	1.11
O + P	0.45	1.00	0.41	1.04	0.36	1.09
O + As	0.45	1.00	0.41	1.04	0.35	1.10
S + N	0.39	1.06	0.34	1.11	0.30	1.15
S + P	0.41	1.04	0.36	1.09	0.35	1.10
S + As	0.41	1.04	0.36	1.09	0.34	1.11
Se + N	0.39	1.06	0.33	1.12	0.27	1.18
Se + P	0.44	1.01	0.36	1.09	0.34	1.11
Se + As	0.40	1.05	0.35	1.10	0.33	1.12

and $\Delta E_{L\text{-}L}$ decreased, when going from silicon to phosphorus, and again from phosphorus to sulfur.

Gibbs energies of charge transfer and recombination, reorganization energy, as well as the electronic coupling and transfer rates for the thiophene bridged systems are shown in Table 5.12. The silicon and phosphorus bridged systems are shown in Table 5.13 and Table 5.14, respectively. For all systems, ΔG_{CT} is more favorable than ΔG_{CR}, and reorganization energies are fairly constant throughout all heteroatom combinations and bridge units. The reorganization energy is between 0.33-0.37 eV for all systems except the Se+As combination with the thiophene bridge, which is 0.27 eV.

For the thiophene-bridged systems whose heteroatom combinations involve sulfur or selenium, the coupling energy and rate of charge recombination increases when moving down the pnictogen column. The silicon-bridged systems whose heteroatom combinations

Table 5.12. Photovoltaic and Marcus variables for the thiophene-bridged multi-heteroatom PDI systems: Gibbs free energy of charge recombination (ΔG_{CR}) and charge transfer (ΔG_{CT}), reorganization energy (λ), electronic coupling (V_{AB}), rate of charge recombination (k_{CR}), charge transfer (k_{CT}), and k_{CT}/k_{CR} ratio.

Ch + Pn	ΔG_{CR} (eV)	ΔG_{CT} (eV)	λ (eV)	V_{AB} (eV)	k_{CR} (s^{-1})	k_{CT} (s^{-1})	k_{CT} / k_{CR}
O + N	-1.41	-0.63	0.33	7.57E-03	1.98E-03	1.29E+11	6.52E+13
O + P	-1.39	-0.65	0.33	2.67E-04	6.08E-06	9.86E+07	1.62E+13
O + As	-1.40	-0.64	0.33	1.20E-03	6.11E-05	2.27E+09	3.72E+13
S + N	-1.45	-0.59	0.33	2.00E-05	1.48E-09	1.75E+06	1.18E+15
S + P	-1.40	-0.64	0.33	5.13E-04	1.21E-05	4.44E+08	3.66E+13
S + As	-1.41	-0.63	0.33	8.78E-04	2.02E-05	1.34E+09	6.62E+13
Se + N	-1.48	-0.56	0.33	1.35E-04	1.79E-08	1.14E+08	6.40E+15
Se + P	-1.41	-0.63	0.34	1.92E-03	2.86E-04	9.21E+09	3.23E+13
Se + As	-1.42	-0.62	0.27	2.04E-03	5.97E-10	1.65E+09	2.76E+18

involve selenium also saw an increase in the electronic coupling when moving down the pnictogen column. The phosphorus-bridged systems whose heteroatom combinations involve sulfur saw increases in the electronic coupling, rate of charge recombination, and rate of charge transfer when moving down the pnictogen column. However, the electronic coupling trend for the phosphorus-bridged systems is miniscule compared to the change seen in the thiophene and silicon-bridged systems.

To improve solar cell properties like: J_{SC}, FF, and exciton dissociation, the rate of charge transfer should be high, and rate of charge recombination kept at a minimum. To quantify this relation, the ratio of the transfer rates (k_{CT}/k_{CR}), can be used. All the systems exhibited fast rates of charge transfer, and slow rates of recombination, resulting in all

Table 5.13. Photovoltaic and Marcus variables for the silicon-bridged multi-heteroatom PDI systems: Gibbs free energy of charge recombination (ΔG_{CR}) and charge transfer (ΔG_{CT}), reorganization energy (λ), electronic coupling (V_{AB}), rate of charge recombination (k_{CR}), charge transfer (k_{CT}), and k_{CT}/k_{CR} ratio.

Ch + Pn	ΔG_{CR} (eV)	ΔG_{CT} (eV)	λ (eV)	V_{AB} (eV)	k_{CR} (s^{-1})	k_{CT} (s^{-1})	k_{CT} / k_{CR}
O + N	-1.32	-0.72	0.36	6.50E-04	1.36E-01	3.56E+08	2.61E+09
O + P	-1.30	-0.74	0.35	6.72E-04	1.22E-01	1.77E+08	1.45E+09
O + As	-1.30	-0.74	0.35	6.87E-04	1.31E-01	1.84E+08	1.41E+09
S + N	-1.36	-0.68	0.36	4.00E-06	1.26E-06	2.86E+04	2.27E+10
S + P	-1.34	-0.70	0.34	1.36E-03	2.37E-02	1.18E+09	4.98E+10
S + As	-1.34	-0.70	0.34	1.17E-03	1.78E-02	9.15E+08	5.14E+10
Se + N	-1.36	-0.68	0.37	4.88E-04	7.24E-02	6.16E+08	8.50E+09
Se + P	-1.31	-0.73	0.35	6.68E-04	1.21E-01	2.10E+08	1.74E+09
Se + As	-1.35	-0.69	0.34	1.92E-03	5.72E-02	3.40E+09	5.94E+10

Table 5.14. Photovoltaic and Marcus variables for the phosphorus-bridged multi-heteroatom PDI systems: Gibbs free energy of charge recombination (ΔG_{CR}) and charge transfer (ΔG_{CT}), reorganization energy (λ), electronic coupling (V_{AB}), rate of charge recombination (k_{CR}), charge transfer (k_{CT}), and k_{CT}/k_{CR} ratio.

Ch + Pn	ΔG_{CR} (eV)	ΔG_{CT} (eV)	λ (eV)	V_{AB} (eV)	k_{CR} (s^{-1})	k_{CT} (s^{-1})	k_{CT} / k_{CR}
O + N	-1.37	-0.67	0.34	1.14E-03	1.65E-03	1.50E+09	9.09E+11
O + P	-1.34	-0.70	0.33	9.30E-05	4.81E-05	4.65E+06	9.68E+10
O + As	-1.34	-0.70	0.33	7.29E-04	2.42E-03	3.00E+08	1.24E+11
S + N	-1.41	-0.63	0.34	3.03E-04	1.62E-05	2.09E+08	1.29E+13
S + P	-1.39	-0.65	0.34	4.08E-04	1.52E-04	2.89E+08	1.90E+12
S + As	-1.39	-0.65	0.34	6.98E-04	2.94E-04	8.26E+08	2.81E+12
Se + N	-1.42	-0.62	0.35	7.21E-04	1.16E-04	1.86E+09	1.61E+13
Se + P	-1.39	-0.65	0.35	4.84E-04	4.28E-04	5.30E+08	1.24E+12
Se + As	-1.40	-0.64	0.34	6.67E-04	1.95E-04	9.84E+08	5.05E+12

ratios being extremely high. A trend is seen that when moving along the 3rd row of the periodic table, the ratio increased. This is mainly due to the changes in energy to the HOMO and LUMO, and therefore the ΔG energies.

5.5 Conclusions

This study has clearly shown that the photovoltaic properties of PDI dimers can be altered by introducing multiple heteroatoms into the structure. This was done by creating a five-membered ring utilizing two carbon atoms from the PDI bay-region, and substituting two atoms of the ring with heteroatoms. The atoms were paired off, and each combination involved one atom from the chalcogen group, and another from the pnictogen group. The bridge unit between PDI units was a five-membered ring and was also altered by changing the heteroatom. The heteroatoms chosen were silicon, phosphorus and sulfur (thiophene), which are all sequential in the 3rd row of the periodic table and were inspired by our previous work with PDI dimers. This created a hybrid between the fused and unfused structures studied earlier in Chapter Four.

The first question that had to be solved was the most stable orientation for each system, and it was found that for all heteroatom combinations using oxygen or sulfur, the most stable orientation was consistent for that series. The selenium systems had a mix between cis-Ch and cis-Pn as the most stable orientation. Among all these stable orientations, only a few had non-planar structures, which is a vital attribute for PDI systems in photovoltaics. All systems had non-planar structures for the S+P and S+As heteroatom combinations, while the Se+P combination in the thiophene system, and O+N combination for the phosphorus and silicon systems, were also non-planar.

In all of these cases, the HOMO energies were most affected by the change in heteroatom combination, while the LUMO remained relatively unchanged between heteroatom combinations utilizing the same bridge unit. This is most likely due to the HOMO orbitals being heavily localized to the bridge unit and bay-region of the PDI dimer, which was the area of these heteroatom substitutions. This led to a consistent decrease in the HOMO-LUMO band gap when moving down the pnictogen column, and an increase when the heteroatom of the bridge unit changes from left to right of the 3rd row of the periodic table. Optical properties saw large changes in the global maximum of the most red-shifted peak. The trend is drawn from the band gap properties, for example, the smaller band gaps seen for silicon-bridged systems had the most red-shifted absorption spectra. Also, the systems utilizing a silicon or phosphorus bridge saw increases in the broadness of their absorption spectra.

In regard to the charge transfer variables, the main trend observed was the k_{CT}/k_{CR} ratio. Moving along the period of the periodic table, the ratio increased by a minimum of about 10^4, and in one case 10^8. This is mostly attributed to the ΔG, and therefore, the HOMO/LUMO energies. Overall, when accounting for molecular orbital energies, geometries, optical properties and charge transfer rates, the S+P and S+As combinations for each system, regardless of the bridge unit used, exhibited the most promise for photovoltaic applications.

Future work should include studying these combinations but using bridge units whose heteroatom is part of the 2nd or 4th row of the periodic table and see if the same trends are observed. Also, the heteroatom combinations using oxygen should be further investigated due to their very broad absorption spectra, especially for the silicon and

phosphorus-bridged systems. Pairing this with the proper donor molecule could cover the entire visible light and near-IR regions.

5.6 Acknowledgements

This work is supported by the Chemical Sciences, Geosciences, and Biosciences Division, Office of Basic Energy Sciences, Office of Science, U. S. Department of Energy under Award Number DE-SC0010212.

CHAPTER SIX

Conclusion

6.1 Dissertation Overview

The work presented in this dissertation has primarily focused on the fundamental properties of organic dyes used in DSSC and OSC devices. Even though there has been a plethora of research done on designing and creating new organic dyes for DSSC and OSC devices over the last couple of decades, there is still much we do not know. Thiophene has been the most common bridge unit used in these dyes by a wide margin, but our work has shown that substituting the sulfur in thiophene for a different heteroatom can provide improved photovoltaic properties. The work detailed here has shown that by introducing heteroatoms into the bridge unit of dyes used for DSSC or OSC devices can dramatically change the properties of the entire system.

In Chapter Three we investigated the π-bridge of the D5 organic dye for a DSSC device. This bridge is a thiophene ring, and we altered it by substituting the sulfur atom for: boron, carbon, nitrogen, oxygen, phosphorus, arsenic and selenium. After calculating all their HOMO/LUMO energies, absorption spectra, and injection efficiencies, we found that the larger elements, on average, led to improved photovoltaic properties. Adsorbing the dyes to a $(TiO_2)_{16}$ surface revealed that the boron substituted system, at least for the far red-shifted peak, would not inject into the surface, however, all other elements showed nearly full electron injections. Larger elements such as sulfur, phosphorus, selenium and arsenic reduce the HOMO-LUMO gap, red shift the absorption spectrum, increase the

dipole moment and are energetically favorable for electron injection. In comparison to the common thiophene bridge unit, π-bridge systems utilizing selenium or phosphorus could prove to be more efficient based on our analysis of photovoltaic properties.

Chapter Four involved us looking at the OSC, which involves a very different mechanic than what is found DSSCs. This also meant investigating a different organic dye. PDI is a very common organic dye used in OSCs due to the relative ease of tuning its electronic properties. However, it suffered from low efficiencies due to aggregation problems, so a dimerized PDI was developed which increased efficiencies tremendously. The link between each PDI is normally through a bridge unit, which has been done using a variety of ring systems. Thiophene is a common one, but benzene, and other conjugated carbon systems have also been synthesized. We applied the same bridge units tested in Chapter Three, except for the boron ring, to act as a bridge unit for these PDI dimers in both the fused and unfused variety. We investigated a variety of electronic and optical properties, as well as the electron transfer and recombination rates using Marcus Theory.

First off, we determined that the HSE06 functional vastly outperformed the prevalent B3LYP functional in estimating the molecular orbital energies. We found that for almost all measured variables, the fused systems outperformed their unfused counterparts. We also found that there is potential for other large atoms in these bridge units, such as silicon and phosphorus. Silicon is most likely the heteroatom substitution to provide the best PCE due to having a higher V_{OC}, stronger and more broad absorption peak, and providing one of the fastest charge transfer rates for both fused and unfused systems. Silicon also has one of the largest k_{CT}/k_{CR} ratios for both systems, proving it could effectively perform exciton dissociation. Bridge units utilizing the oxygen, sulfur and

selenium atoms have already be synthesized and investigated in the literature, but all the other fused system substitutions resulted in increased V_{OC}, while still maintaining acceptable $\Delta E_{L\text{-}L}$ values. They also tend to feature larger k_{CT}/k_{CR} ratios, showing these other substitutions could provide larger J_{SC} and FF values.

Our results from Chapter Four led us to wonder what would happen if we substituted more than one heteroatom into the dimerized PDI system. This was done by substituting two heteroatoms, one chalcogen and one pnictogen, into the PDI bay-region by the creation of a five-membered ring. Also, instead of just thiophene as the bridge unit, we investigated the phosphorus and silicon heteroatom ring species as well. This is because of our conclusions from Chapter Four, which speculated that these ring species could lead to improved photovoltaic results, and also so three elements in the same row of the periodic table can be compared.

The most stable orientation of each PDI unit to the bridge unit was determined to be consistent for systems using oxygen or sulfur, but not selenium. As mentioned previously, PDI has aggregation issues in BHJ cells due to its planarity, so determining if these systems are still planar was the first property investigated. Most systems were planar, but the Se+P combination with the thiophene bridge, the O+N combination with the phosphorus and silicon-bridged systems, and the S+P and S+As heteroatom combinations with every bridge system were non-planar. The HOMO energies fluctuated leading to a consistent decrease in the band gap when moving down the pnictogen column, as well as an increase in the band gap when the heteroatom of the bridge unit increased in atomic number. There was also broadening of the absorption spectra when moving from right to

left in the 3rd row of the periodic table. Overall, the S+P and S+As heteroatom combinations exhibited the most promise for photovoltaic applications.

The key takeaway from this research is that π-bridge ring structures utilizing one or more heteroatoms have the potential to vastly improve both DSSC and OSC efficiencies. Rings utilizing sulfur are currently the most prevalent in organic dyes, but other heteroatoms have been shown here to drastically improve the photovoltaic properties. Heteroatoms from the third and fourth rows of the periodic table have shown improved photovoltaic properties, such as HOMO and LUMO energies, red-shifted absorption spectra, and k_{CT}/k_{CR} ratios. Also, the introduction of multiple heteroatoms for use in an OSC device produced interesting results, especially regarding the absorption properties.

6.2. Future Directions

The future of DSSC and OSC devices is a bright one. These cells are still in their infancy compared to the popular c-Si cells and there is a lot of promise in these devices. The fact these devices are thin, flexible and cheap, has kept the interest of scientists since their conception, and the constant increases in efficiency each year has kept these cells in the discussion for commercial purposes. Even though they have been heavily researched and published for a couple decades, there are still new technologies and cell designs emerging that consistently improve the cell. With the increase in computational power, the ability for experimentalists to supplement their research with theoretical results has aided immensely, and theoreticians modeling systems using DFT has helped give experimentalists direction.

6.2.1. Future Directions for Dye-Sensitized Solar Cells

For DSSCs the technique of adsorbing multiple dyes onto the TiO_2 surface has been gaining a lot of ground lately and shows a lot of promise moving forward.[194-196] Recently, silyl anchors were tested and greatly improved cell efficiencies,[25] so the design of new anchor groups to bond the dye to the surface should also be further investigated. From a materials perspective, the investigation of new counter electrodes to replace platinum is on the rise, and new materials such as metal dichalcogenides have shown a lot of promise.[197-198] Perovskites have been of considerable interest lately as a replacement to molecular dyes, and have led to increased cell efficiencies of >20%.[199-201]

6.2.2. Future Directions for Organic Solar Cells

OSCs currently have more promise than DSSCs due having greater efficiencies, while also containing less moving parts in the cell, such as no solvent or electrolyte. Currently, the top performing OSCs utilize a tandem or ternary active layer cell structure (Figure 6.1),[66, 202-204] which utilizes more than one active layer or more than a single donor-acceptor pair, respectively. However, to our knowledge there have been no purely theoretical studies done on these kinds of systems. It is difficult to model due to the extra pathways available to an excited electron, but by splitting the overall BHJ system into smaller parts one can eventually piece together the overall picture of the cell mechanism.

In Chapter Four and Chapter Five the orientation between donor and acceptor, even when optimized, is not a true representation of the D-A coupled system. To describe the D-A orientations more accurately, molecular dynamics (MD) should be run to examine the amount of mixing between donor and acceptor molecules. There are some articles in the

literature that utilize MD to determine various BHJ properties,[205-208] but very little research has been done to combine the MD and QM results.[209] This coupled approach can

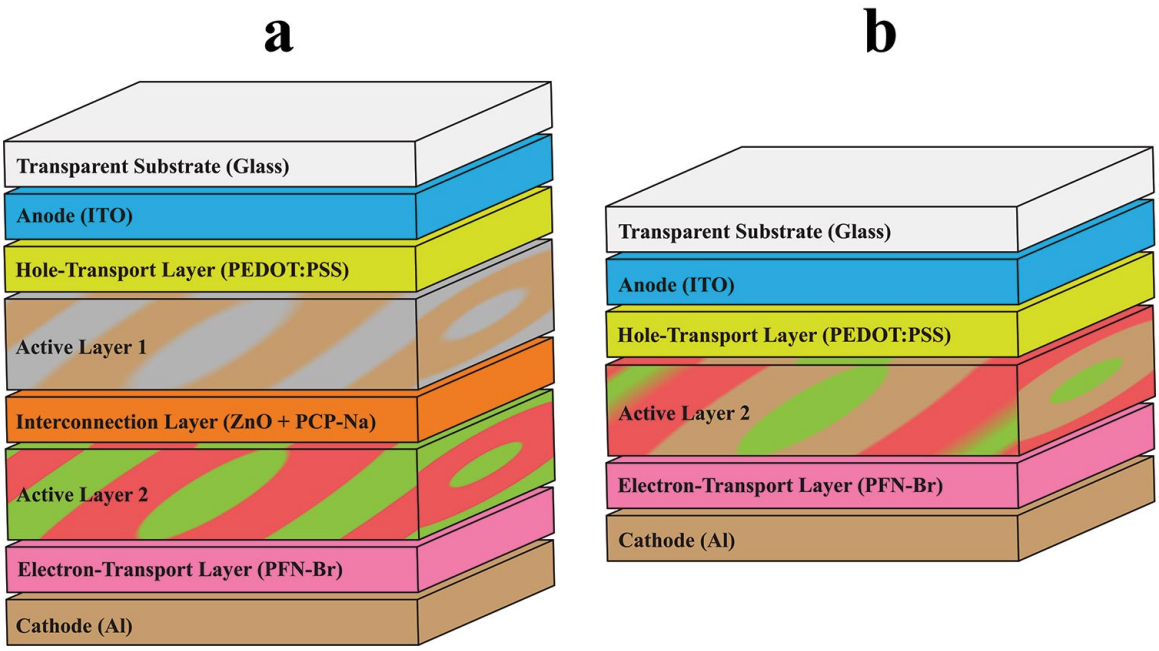

Figure 6.1. Illustration giving examples of organic solar cells using a) tandem or b) ternary architectures.

lead to accurate representations of the BHJ layer and the D-A interface. Also, current computational studies cap the polymers at a fairly small chain length,[210-211] so using methods like course-graining would lead to longer chain lengths being calculated.

In the past, these kinds of theoretical studies wouldn't be possible without the most state-of-the-art supercomputers, but with the increase in computational power the ability to model these kinds of systems is now within reason. With the use of computational tools, the inner workings of the cell can be revealed, and conclusions can be reached that can ultimately guide the development of these solar devices.

BIBLIOGRAPHY

1. Smalley, R. E., In *ACS National Meeting*, American Chemical Society: New York, NY, 2003.

2. International Energy Outlook. Administration, E. I., Ed. 2017.

3. Annual Energy Outlook. Administration, E. I., Ed. 2018.

4. Energy and the challenge of sustainability. Affairs, U. N. D. o. E. a. S., Ed. 2000.

5. Key World Energy Statistics. Agency, I. E., Ed. 2017.

6. Mills, D., Advances in solar thermal electricity technology. *Solar Energy* **2004,** *76* (1), 19-31.

7. Becquerel, A. E., Recherches sur les effets de la radiation chimique de la lumiere solaire au moyen des courants electriques. *Comptes Rendus de L'Academie des Sciences* **1839,** *9*, 145-149.

8. Einstein, A., Über einen die Erzeugung und Verwandlung des Lichtes betreffenden heuristischen Gesichtspunkt. *Annalen der Physik* **1905,** *322* (6), 132-148.

9. Smith, W., Effect of Light on Selenium During the Passage of An Electric Current*. *Nature* **1873,** *7*, 303.

10. Nelson, J., *The physics of solar cells*. World Scientific: 2003; Vol. 57.

11. Ohl, R. S. Light-sensitive electric device. 2,402,622, 1941.

12. Ohl, R. S. Light-sensitive device including silicon. 2,443,542, 1941.

13. Lashkaryov, V., Investigation of a barrier layer by the thermoprobe method. *Ukranian Journal of Physics* **2006,** *53* (Special Issue), 53-56.

14. Chapin, D. M.; Fuller, C. S.; Pearson, G. L., A New Silicon p-n Junction Photocell for Converting Solar Radiation into Electrical Power. *Journal of Applied Physics* **1954,** *25* (5), 676-677.

15. Photovoltaics Report. Energy, F. I. f. S.; Systems, Eds. 2018.

16. O'Regan, B.; Grätzel, M., A low-cost, high-efficiency solar cell based on dye-sensitized colloidal TiO2 films. *Nature* **1991,** *353*, 737.

17. Tang, C. W., Two-layer organic photovoltaic cell. *Applied Physics Letters* **1986,** *48* (2), 183-185.

18. Shockley, W.; Queisser, H. J., Detailed Balance Limit of Efficiency of p-n Junction Solar Cells. *Journal of Applied Physics* **1961,** *32* (3), 510-519.

19. Archer, M. D.; Bolton, J. R., Requirements for ideal performance of photochemical and photovoltaic solar energy converters. *The Journal of Physical Chemistry* **1990,** *94* (21), 8028-8036.

20. Markvart, T.; Landsberg, P. T., Thermodynamics and reciprocity of solar energy conversion. *Physica E: Low-dimensional Systems and Nanostructures* **2002,** *14* (1), 71-77.

21. Ross, R. T., Thermodynamic Limitations on the Conversion of Radiant Energy into Work. *The Journal of Chemical Physics* **1966,** *45* (1), 1-7.

22. Gonzalez, C. C.; Ross, R. G., Performance measurement reference conditions for terrestrial photovoltaics. In *Proceedings of the International Solar Energy Society Conference*, Phoenix, AZ, 1980.

23. Standard Tables for Reference Solar Spectral Irradiances: Direct Normal and Hemispherical on 37° Tilted Surface. 2012.

24. Mathew, S.; Yella, A.; Gao, P.; Humphry-Baker, R.; Curchod, B. F. E.; Ashari-Astani, N.; Tavernelli, I.; Rothlisberger, U.; Nazeeruddin, M. K.; Grätzel, M., Dye-sensitized solar cells with 13% efficiency achieved through the molecular engineering of porphyrin sensitizers. *Nature Chemistry* **2014,** *6*, 242.

25. Kakiage, K.; Aoyama, Y.; Yano, T.; Oya, K.; Fujisawa, J.-i.; Hanaya, M., Highly-efficient dye-sensitized solar cells with collaborative sensitization by silyl-anchor and carboxy-anchor dyes. *Chemical Communications* **2015,** *51* (88), 15894-15897.

26. Kumara, N. T. R. N.; Lim, A.; Lim, C. M.; Petra, M. I.; Ekanayake, P., Recent progress and utilization of natural pigments in dye sensitized solar cells: A review. *Renewable and Sustainable Energy Reviews* **2017,** *78*, 301-317.

27. Le Bahers, T.; Pauporté, T.; Lainé, P. P.; Labat, F.; Adamo, C.; Ciofini, I., Modeling Dye-Sensitized Solar Cells: From Theory to Experiment. *The Journal of Physical Chemistry Letters* **2013,** *4* (6), 1044-1050.

28. Feng, J.; Jiao, Y.; Ma, W.; Nazeeruddin, M. K.; Grätzel, M.; Meng, S., First Principles Design of Dye Molecules with Ullazine Donor for Dye Sensitized Solar Cells. *The Journal of Physical Chemistry C* **2013,** *117* (8), 3772-3778.

29. Pochettino, A., The development of organic conductors, including semiconductors, metals and superconductors cont. *Academy Lincei Rendus* **1906,** *15*, 355.

30. Koenigsberger, J.; Schilling, K., Über Elektrizitätsleitung in festen Elementen und Verbindungen. I. Minima des Widerstandes, Prüfung auf Elektronenleitung, Anwendung der Dissoziationsformeln. *Annalen der Physik* **2006,** *337* (6), 179-230.

31. Sariciftci, N. S.; Smilowitz, L.; Heeger, A. J.; Wudl, F., Photoinduced Electron Transfer from a Conducting Polymer to Buckminsterfullerene. *Science* **1992,** *258* (5087), 1474.

32. Yu, G.; Gao, J.; Hummelen, J. C.; Wudl, F.; Heeger, A. J., Polymer Photovoltaic Cells: Enhanced Efficiencies via a Network of Internal Donor-Acceptor Heterojunctions. *Science* **1995,** *270* (5243), 1789.

33. Scharber, M. C.; Sariciftci, N. S., Efficiency of bulk-heterojunction organic solar cells. *Progress in Polymer Science* **2013,** *38* (12), 1929-1940.

34. Carsten, D.; Vladimir, D., Polymer–fullerene bulk heterojunction solar cells. *Reports on Progress in Physics* **2010,** *73* (9), 096401.

35. Scholes, G. D.; Rumbles, G., Excitons in nanoscale systems. *Nature Materials* **2006,** *5*, 683.

36. Green, M. A., Improved value for the silicon free exciton binding energy. *AIP Advances* **2013,** *3* (11), 112104.

37. Nunzi, J.-M., Organic photovoltaic materials and devices. *Comptes Rendus Physique* **2002,** *3* (4), 523-542.

38. Günes, S.; Neugebauer, H.; Sariciftci, N. S., Conjugated Polymer-Based Organic Solar Cells. *Chemical Reviews* **2007,** *107* (4), 1324-1338.

39. Ayzner, A. L.; Mei, J.; Appleton, A.; DeLongchamp, D.; Nardes, A.; Benight, S.; Kopidakis, N.; Toney, M. F.; Bao, Z., Impact of the Crystallite Orientation Distribution on Exciton Transport in Donor–Acceptor Conjugated Polymers. *ACS Applied Materials & Interfaces* **2015,** *7* (51), 28035-28041.

40. Shaheen, S. E.; Radspinner, R.; Peyghambarian, N.; Jabbour, G. E., Fabrication of bulk heterojunction plastic solar cells by screen printing. *Applied Physics Letters* **2001,** *79* (18), 2996-2998.

41. Padinger, F.; Rittberger, R. S.; Sariciftci, N. S., Effects of Postproduction Treatment on Plastic Solar Cells. *Advanced Functional Materials* **2003,** *13* (1), 85-88.

42. Gebeyehu, D.; Maennig, B.; Drechsel, J.; Leo, K.; Pfeiffer, M., Bulk-heterojunction photovoltaic devices based on donor–acceptor organic small molecule blends. *Solar Energy Materials and Solar Cells* **2003,** *79* (1), 81-92.

43. Peumans, P.; Uchida, S.; Forrest, S. R., Efficient bulk heterojunction photovoltaic cells using small-molecular-weight organic thin films. *Nature* **2003,** *425*, 158.

44. Chen, C.-C.; Chang, W.-H.; Yoshimura, K.; Ohya, K.; You, J.; Gao, J.; Hong, Z.; Yang, Y., An Efficient Triple-Junction Polymer Solar Cell Having a Power Conversion Efficiency Exceeding 11%. *Advanced Materials* **2014,** *26* (32), 5670-5677.

45. Lee, Y.-J.; Wang, J.; Cheng, S. R.; Hsu, J. W. P., Solution Processed ZnO Hybrid Nanocomposite with Tailored Work Function for Improved Electron Transport Layer in Organic Photovoltaic Devices. *ACS Applied Materials & Interfaces* **2013,** *5* (18), 9128-9133.

46. Wang, J.; Lee, Y.-J.; Hsu, J. W. P., One-Step Synthesis of ZnO Nanocrystals in n-Butanol with Bandgap Control: Applications in Hybrid and Organic Photovoltaic Devices. *The Journal of Physical Chemistry C* **2014,** *118* (32), 18417-18423.

47. Yip, H. L.; Hau Steven, K.; Baek Nam, S.; Ma, H.; Jen Alex, K. Y., Polymer Solar Cells That Use Self-Assembled-Monolayer- Modified ZnO/Metals as Cathodes. *Advanced Materials* **2008,** *20* (12), 2376-2382.

48. Ferreira, S. R.; Lu, P.; Lee, Y.-J.; Davis, R. J.; Hsu, J. W. P., Effect of Zinc Oxide Electron Transport Layers on Performance and Shelf Life of Organic Bulk Heterojunction Devices. *The Journal of Physical Chemistry C* **2011,** *115* (27), 13471-13475.

49. Thompson Barry , C.; Fréchet Jean , M. J., Polymer–Fullerene Composite Solar Cells. *Angewandte Chemie International Edition* **2007,** *47* (1), 58-77.

50. He, Z.; Xiao, B.; Liu, F.; Wu, H.; Yang, Y.; Xiao, S.; Wang, C.; Russell, T. P.; Cao, Y., Single-junction polymer solar cells with high efficiency and photovoltage. *Nature Photonics* **2015,** *9*, 174.

51. Zhao, J.; Li, Y.; Yang, G.; Jiang, K.; Lin, H.; Ade, H.; Ma, W.; Yan, H., Efficient organic solar cells processed from hydrocarbon solvents. *Nature Energy* **2016,** *1*, 15027.

52. Yan, C.; Barlow, S.; Wang, Z.; Yan, H.; Jen, A. K. Y.; Marder, S. R.; Zhan, X., Non-fullerene acceptors for organic solar cells. *Nature Reviews Materials* **2018,** *3*, 18003.

53. Distler, A.; Sauermann, T.; Egelhaaf, H. J.; Rodman, S.; Waller, D.; Cheon, K. S.; Lee, M.; Guldi Dirk, M., The Effect of PCBM Dimerization on the Performance of Bulk Heterojunction Solar Cells. *Advanced Energy Materials* **2014,** *4* (1), 1300693.

54. Holliday, S.; Ashraf, R. S.; Wadsworth, A.; Baran, D.; Yousaf, S. A.; Nielsen, C. B.; Tan, C.-H.; Dimitrov, S. D.; Shang, Z.; Gasparini, N.; Alamoudi, M.; Laquai, F.; Brabec, C. J.; Salleo, A.; Durrant, J. R.; McCulloch, I., High-efficiency and air-stable P3HT-based polymer solar cells with a new non-fullerene acceptor. **2016,** *7*, 11585.

55. Nielsen, T. D.; Cruickshank, C.; Foged, S.; Thorsen, J.; Krebs, F. C., Business, market and intellectual property analysis of polymer solar cells. *Solar Energy Materials and Solar Cells* **2010,** *94* (10), 1553-1571.

56. Eftaiha, A. a. F.; Sun, J.-P.; Hill, I. G.; Welch, G. C., Recent advances of non-fullerene, small molecular acceptors for solution processed bulk heterojunction solar cells. *Journal of Materials Chemistry A* **2014,** *2* (5), 1201-1213.

57. Zhang, S.; Qin, Y.; Zhu, J.; Hou, J., Over 14% Efficiency in Polymer Solar Cells Enabled by a Chlorinated Polymer Donor. *Advanced Materials* **2018,** *30* (20), 1800868.

58. Zhang, H.; Yao, H.; Hou, J.; Zhu, J.; Zhang, J.; Li, W.; Yu, R.; Gao, B.; Zhang, S.; Hou, J., Over 14% Efficiency in Organic Solar Cells Enabled by Chlorinated Nonfullerene Small-Molecule Acceptors. *Advanced Materials* **2018,** *0* (0), 1800613.

59. Kumari, T.; Lee, S. M.; Kang, S.-H.; Chen, S.; Yang, C., Ternary solar cells with a mixed face-on and edge-on orientation enable an unprecedented efficiency of 12.1%. *Energy & Environmental Science* **2017,** *10* (1), 258-265.

60. Li, M.; Gao, K.; Wan, X.; Zhang, Q.; Kan, B.; Xia, R.; Liu, F.; Yang, X.; Feng, H.; Ni, W.; Wang, Y.; Peng, J.; Zhang, H.; Liang, Z.; Yip, H.-L.; Peng, X.; Cao, Y.; Chen, Y., Solution-processed organic tandem solar cells with power conversion efficiencies >12%. *Nature Photonics* **2016,** *11*, 85.

61. Anthony John, E.; Facchetti, A.; Heeney, M.; Marder Seth, R.; Zhan, X., n-Type Organic Semiconductors in Organic Electronics. *Advanced Materials* **2010,** *22* (34), 3876-3892.

62. Lin, Y.; Zhan, X., Designing Efficient Non-Fullerene Acceptors by Tailoring Extended Fused-Rings with Electron-Deficient Groups. *Advanced Energy Materials* **2015,** *5* (20), 1501063.

63. Schmidt-Mende, L.; Fechtenkötter, A.; Müllen, K.; Moons, E.; Friend, R. H.; MacKenzie, J. D., Self-Organized Discotic Liquid Crystals for High-Efficiency Organic Photovoltaics. *Science* **2001,** *293* (5532), 1119.

64. Liu, Z.; Wu, Y.; Zhang, Q.; Gao, X., Non-fullerene small molecule acceptors based on perylene diimides. *Journal of Materials Chemistry A* **2016,** *4* (45), 17604-17622.

65. Lin, Y.; Wang, J.; Zhang, Z. G.; Bai, H.; Li, Y.; Zhu, D.; Zhan, X., An Electron Acceptor Challenging Fullerenes for Efficient Polymer Solar Cells. *Advanced Materials* **2015,** *27* (7), 1170-1174.

66. Che, X.; Li, Y.; Qu, Y.; Forrest, S. R., High fabrication yield organic tandem photovoltaics combining vacuum- and solution-processed subcells with 15% efficiency. *Nature Energy* **2018,** *3* (5), 422-427.

67. Hartree, D. R., The Wave Mechanics of an Atom with a Non-Coulomb Central Field. Part I. Theory and Methods. *Mathematical Proceedings of the Cambridge Philosophical Society* **2008,** *24* (1), 89-110.

68. Blinder, S. M., Basic Concepts of Self-Consistent-Field Theory. *American Journal of Physics* **1965,** *33* (6), 431-443.

69. Roothaan, C. C. J., New Developments in Molecular Orbital Theory. *Reviews of Modern Physics* **1951,** *23* (2), 69-89.

70. Hohenberg, P.; Kohn, W., Inhomogeneous Electron Gas. *Physical Review* **1964,** *136* (3B), B864-B871.

71. Kohn, W.; Sham, L. J., Self-Consistent Equations Including Exchange and Correlation Effects. *Physical Review* **1965,** *140* (4A), A1133-A1138.

72. Langreth, D. C.; Mehl, M. J., Beyond the local-density approximation in calculations of ground-state electronic properties. *Physical Review B* **1983,** *28* (4), 1809-1834.

73. Perdew, J. P.; Chevary, J. A.; Vosko, S. H.; Jackson, K. A.; Pederson, M. R.; Singh, D. J.; Fiolhais, C., Atoms, molecules, solids, and surfaces: Applications of the generalized gradient approximation for exchange and correlation. *Physical Review B* **1992,** *46* (11), 6671-6687.

74. Becke, A. D., Density-functional exchange-energy approximation with correct asymptotic behavior. *Physical Review A* **1988,** *38* (6), 3098-3100.

75. Perdew, J. P.; Burke, K.; Ernzerhof, M., Generalized Gradient Approximation Made Simple. *Physical Review Letters* **1996,** *77* (18), 3865-3868.

76. Perdew, J. P.; Yue, W., Accurate and simple density functional for the electronic exchange energy: Generalized gradient approximation. *Physical Review B* **1986,** *33* (12), 8800-8802.

77. Lee, C.; Yang, W.; Parr, R. G., Development of the Colle-Salvetti correlation-energy formula into a functional of the electron density. *Physical Review B* **1988,** *37* (2), 785-789.

78. Becke, A. D., Density-functional thermochemistry. III. The role of exact exchange. *The Journal of Chemical Physics* **1993,** *98* (7), 5648-5652.

79. Vosko, S. H.; Wilk, L.; Nusair, M., Accurate spin-dependent electron liquid correlation energies for local spin density calculations: a critical analysis. *Canadian Journal of Physics* **1980,** *58* (8), 1200-1211.

80. Adamo, C.; Barone, V., Toward reliable density functional methods without adjustable parameters: The PBE0 model. *The Journal of Chemical Physics* **1999,** *110* (13), 6158-6170.

81. Savin, A., On degeneracy, near-degeneracy and density functional theory. In *Theoretical and Computational Chemistry*, Seminario, J. M., Ed. Elsevier: 1996; Vol. 4, pp 327-357.

82. Yanai, T.; Tew, D. P.; Handy, N. C., A new hybrid exchange–correlation functional using the Coulomb-attenuating method (CAM-B3LYP). *Chemical Physics Letters* **2004,** *393* (1), 51-57.

83. Chai, J.-D.; Head-Gordon, M., Systematic optimization of long-range corrected hybrid density functionals. *The Journal of Chemical Physics* **2008,** *128* (8), 084106.

84. Chai, J.-D.; Head-Gordon, M., Long-range corrected hybrid density functionals with damped atom-atom dispersion corrections. *Physical Chemistry Chemical Physics* **2008,** *10* (44), 6615-6620.

85. Becke, A. D., Density-functional thermochemistry. V. Systematic optimization of exchange-correlation functionals. *The Journal of Chemical Physics* **1997,** *107* (20), 8554-8560.

86. Heyd, J.; Scuseria, G. E.; Ernzerhof, M., Hybrid functionals based on a screened Coulomb potential. *The Journal of Chemical Physics* **2003,** *118* (18), 8207-8215.

87. Krukau, A. V.; Vydrov, O. A.; Izmaylov, A. F.; Scuseria, G. E., Influence of the exchange screening parameter on the performance of screened hybrid functionals. *The Journal of Chemical Physics* **2006,** *125* (22), 224106.

88. Runge, E.; Gross, E. K. U., Density-Functional Theory for Time-Dependent Systems. *Physical Review Letters* **1984,** *52* (12), 997-1000.

89. van Leeuwen, R., Mapping from Densities to Potentials in Time-Dependent Density-Functional Theory. *Physical Review Letters* **1999,** *82* (19), 3863-3866.

90. Petersilka, M.; Gossmann, U. J.; Gross, E. K. U., Excitation Energies from Time-Dependent Density-Functional Theory. *Physical Review Letters* **1996,** *76* (8), 1212-1215.

91. Zangwill, A.; Soven, P., Resonant Photoemission in Barium and Cerium. *Physical Review Letters* **1980,** *45* (3), 204-207.

92. Zangwill, A.; Soven, P., Resonant two-electron excitation in copper. *Physical Review B* **1981,** *24* (8), 4121-4127.

93. Marcus, R. A., Electron transfer reactions in chemistry. Theory and experiment. *Reviews of Modern Physics* **1993,** *65* (3), 599-610.

94. Taube, H.; Myers, H.; Rich, R. L., OBSERVATIONS ON THE MECHANISM OF ELECTRON TRANSFER IN SOLUTION1. *Journal of the American Chemical Society* **1953,** *75* (16), 4118-4119.

95. Marcus, R. A., On the Theory of Oxidation-Reduction Reactions Involving Electron Transfer. I. *The Journal of Chemical Physics* **1956,** *24* (5), 966-978.

96. Marcus, R. A.; Sutin, N., Electron transfers in chemistry and biology. *Biochimica et Biophysica Acta (BBA) - Reviews on Bioenergetics* **1985,** *811* (3), 265-322.

97. Evans, M. G.; Polanyi, M., Some applications of the transition state method to the calculation of reaction velocities, especially in solution. *Transactions of the Faraday Society* **1935,** *31* (0), 875-894.

98. Miller, J. R.; Calcaterra, L. T.; Closs, G. L., Intramolecular long-distance electron transfer in radical anions. The effects of free energy and solvent on the reaction rates. *Journal of the American Chemical Society* **1984,** *106* (10), 3047-3049.

99. Anta, J. A.; Guillén, E.; Tena-Zaera, R., ZnO-Based Dye-Sensitized Solar Cells. *The Journal of Physical Chemistry C* **2012,** *116* (21), 11413-11425.

100. Kamat, P. V., Meeting the Clean Energy Demand: Nanostructure Architectures for Solar Energy Conversion. *The Journal of Physical Chemistry C* **2007,** *111* (7), 2834-2860.

101. Grätzel, M., Dye-sensitized solar cells. *Journal of Photochemistry and Photobiology C: Photochemistry Reviews* **2003,** *4* (2), 145-153.

102. Wu, Y.; Zhu, W.-H.; Zakeeruddin, S. M.; Grätzel, M., Insight into D–A−π–A Structured Sensitizers: A Promising Route to Highly Efficient and Stable Dye-Sensitized Solar Cells. *ACS Applied Materials & Interfaces* **2015,** *7* (18), 9307-9318.

103. Tarsang, R.; Promarak, V.; Sudyoadsuk, T.; Namuangruk, S.; Jungsuttiwong, S., Tuning the electron donating ability in the triphenylamine-based D-π-A architecture for highly efficient dye-sensitized solar cells. *Journal of Photochemistry and Photobiology A: Chemistry* **2014,** *273*, 8-16.

104. Mishra, A.; Fischer, M.; Bauerle, P., Metal-Free Organic Dyes for Dye-Sensitized Solar Cells: From Structure: Property Relationships to Design Rules. *Angewandte Chemie International Edition* **2009,** *48* (14), 2474-2499.

105. Hagfeldt, A.; Boschloo, G.; Sun, L.; Kloo, L.; Pettersson, H., Dye-Sensitized Solar Cells. *Chemical Reviews* **2010,** *110* (11), 6595-6663.

106. Fischer, M. K. R.; Wenger, S.; Wang, M.; Mishra, A.; Zakeeruddin, S. M.; Grätzel, M.; Bäuerle, P., D-π-A Sensitizers for Dye-Sensitized Solar Cells: Linear vs Branched Oligothiophenes. *Chemistry of Materials* **2010,** *22* (5), 1836-1845.

107. Listorti, A.; O'Regan, B.; Durrant, J. R., Electron Transfer Dynamics in Dye-Sensitized Solar Cells. *Chemistry of Materials* **2011,** *23* (15), 3381-3399.

108. Nazeeruddin, M. K.; Kay, A.; Rodicio, I.; Humphry-Baker, R.; Mueller, E.; Liska, P.; Vlachopoulos, N.; Graetzel, M., Conversion of light to electricity by cis-X2bis(2,2'-bipyridyl-4,4'-dicarboxylate)ruthenium(II) charge-transfer sensitizers (X = Cl-, Br-, I-, CN-, and SCN-) on nanocrystalline titanium dioxide electrodes. *Journal of the American Chemical Society* **1993,** *115* (14), 6382-6390.

109. Shklover, V.; Ovchinnikov, Y. E.; Braginsky, L. S.; Zakeeruddin, S. M.; Grätzel, M., Structure of Organic/Inorganic Interface in Assembled Materials Comprising Molecular Components. Crystal Structure of the Sensitizer Bis[(4,4‘-carboxy-2,2‘-bipyridine)(thiocyanato)]ruthenium(II). *Chemistry of Materials* **1998,** *10* (9), 2533-2541.

110. Bayliss, S. L.; Cole, J. M.; Waddell, P. G.; McKechnie, S.; Liu, X., Predicting Solar-Cell Dyes for Cosensitization. *The Journal of Physical Chemistry C* **2014,** *118* (26), 14082-14090.

111. Wang, L.; Yang, R. T., New sorbents for hydrogen storage by hydrogen spillover - a review. *Energy & Environmental Science* **2008,** *1* (2), 268-279.

112. Hagberg, D. P.; Yum, J.-H.; Lee, H.; De Angelis, F.; Marinado, T.; Karlsson, K. M.; Humphry-Baker, R.; Sun, L.; Hagfeldt, A.; Grätzel, M.; Nazeeruddin, M. K., Molecular Engineering of Organic Sensitizers for Dye-Sensitized Solar Cell Applications. *Journal of the American Chemical Society* **2008,** *130* (19), 6259-6266.

113. Hagberg, D. P.; Edvinsson, T.; Marinado, T.; Boschloo, G.; Hagfeldt, A.; Sun, L., A novel organic chromophore for dye-sensitized nanostructured solar cells. *Chemical Communications* **2006,** (21), 2245-2247.

114. Meng, S.; Kaxiras, E.; Nazeeruddin, M. K.; Grätzel, M., Design of Dye Acceptors for Photovoltaics from First-Principles Calculations. *The Journal of Physical Chemistry C* **2011,** *115* (18), 9276-9282.

115. Manzhos, S.; Segawa, H.; Yamashita, K., Computational dye design by changing the conjugation order: Failure of LR-TDDFT to predict relative excitation energies in organic dyes differing by the position of the methine unit. *Chemical Physics Letters* **2012,** *527*, 51-56.

116. Pastore, M.; Mosconi, E.; De Angelis, F.; Grätzel, M., A Computational Investigation of Organic Dyes for Dye-Sensitized Solar Cells: Benchmark, Strategies, and Open Issues. *The Journal of Physical Chemistry C* **2010,** *114* (15), 7205-7212.

117. Marenich, A. V.; Cramer, C. J.; Truhlar, D. G., Universal Solvation Model Based on Solute Electron Density and on a Continuum Model of the Solvent Defined by the Bulk Dielectric Constant and Atomic Surface Tensions. *The Journal of Physical Chemistry B* **2009,** *113* (18), 6378-6396.

118. Casanova, D.; Rotzinger, F. P.; Grätzel, M., Computational Study of Promising Organic Dyes for High-Performance Sensitized Solar Cells. *Journal of Chemical Theory and Computation* **2010,** *6* (4), 1219-1227.

119. Frisch, M. J.; Trucks, G. W.; Schlegel, H. B.; Scuseria, G. E.; Robb, M. A.; Cheeseman, J. R.; Scalmani, G.; Barone, V.; Mennucci, B.; Petersson, G. A.; Nakatsuji, H.; Caricato, M.; Li, X.; Hratchian, H. P.; Izmaylov, A. F.; Bloino, J.; Zheng, G.; Sonnenberg, J. L.; Hada, M.; Ehara, M.; Toyota, K.; Fukuda, R.; Hasegawa, J.; Ishida, M.; Nakajima, T.; Honda, Y.; Kitao, O.; Nakai, H.; Vreven, T.; Montgomery Jr., J. A.; Peralta, J. E.; Ogliaro, F.; Bearpark, M. J.; Heyd, J.; Brothers, E. N.; Kudin, K. N.; Staroverov, V. N.; Kobayashi, R.; Normand, J.; Raghavachari, K.; Rendell, A. P.; Burant, J. C.; Iyengar, S. S.; Tomasi, J.; Cossi, M.; Rega, N.; Millam, N. J.; Klene, M.; Knox, J. E.; Cross, J. B.; Bakken, V.; Adamo, C.; Jaramillo, J.; Gomperts, R.; Stratmann, R. E.; Yazyev, O.; Austin, A. J.; Cammi, R.; Pomelli, C.; Ochterski, J. W.; Martin, R. L.; Morokuma, K.; Zakrzewski, V. G.; Voth, G. A.; Salvador, P.; Dannenberg, J. J.; Dapprich, S.; Daniels, A. D.; Farkas, Ö.; Foresman, J. B.; Ortiz, J. V.; Cioslowski, J.; Fox, D. J. *Gaussian 09*, Gaussian, Inc.: Wallingford, CT, USA, 2009.

120. Rühle, S.; Greenshtein, M.; Chen, S. G.; Merson, A.; Pizem, H.; Sukenik, C. S.; Cahen, D.; Zaban, A., Molecular Adjustment of the Electronic Properties of Nanoporous Electrodes in Dye-Sensitized Solar Cells. *The Journal of Physical Chemistry B* **2005,** *109* (40), 18907-18913.

121. Zhang, J.; Li, H.-B.; Sun, S.-L.; Geng, Y.; Wu, Y.; Su, Z.-M., Density functional theory characterization and design of high-performance diarylamine-fluorene dyes with different [small pi] spacers for dye-sensitized solar cells. *Journal of Materials Chemistry* **2012,** *22* (2), 568-576.

122. Anderson, N. A.; Ai, X.; Lian, T., Electron Injection Dynamics from Ru Polypyridyl Complexes to ZnO Nanocrystalline Thin Films. *The Journal of Physical Chemistry B* **2003,** *107* (51), 14414-14421.

123. Ramakrishna, G.; Singh, A. K.; Palit, D. K.; Ghosh, H. N., Dynamics of Interfacial Electron Transfer from Photoexcited Quinizarin (Qz) into the Conduction Band of TiO2 and Surface States of ZrO2 Nanoparticles. *The Journal of Physical Chemistry B* **2004,** *108* (15), 4775-4783.

124. Zimmermann, C.; Willig, F.; Ramakrishna, S.; Burfeindt, B.; Pettinger, B.; Eichberger, R.; Storck, W., Experimental Fingerprints of Vibrational Wave-Packet Motion during Ultrafast Heterogeneous Electron Transfer. *The Journal of Physical Chemistry B* **2001,** *105* (38), 9245-9253.

125. Nithya, R.; Senthilkumar, K., Theoretical studies on the quinoidal thiophene based dyes for dye sensitized solar cell and NLO applications. *Physical Chemistry Chemical Physics* **2014,** *16* (39), 21496-21505.

126. Katoh, R.; Furube, A.; Yoshihara, T.; Hara, K.; Fujihashi, G.; Takano, S.; Murata, S.; Arakawa, H.; Tachiya, M., Efficiencies of Electron Injection from Excited N3 Dye into Nanocrystalline Semiconductor (ZrO2, TiO2, ZnO, Nb2O5, SnO2, In2O3) Films. *The Journal of Physical Chemistry B* **2004,** *108* (15), 4818-4822.

127. Preat, J.; Jacquemin, D.; Perpete, E. A., Towards new efficient dye-sensitised solar cells. *Energy & Environmental Science* **2010,** *3* (7), 891-904.

128. Yang, F.; Akhtaruzzaman, M.; Islam, A.; Jin, T.; El-Shafei, A.; Qin, C.; Han, L.; Alamry, K. A.; Kosa, S. A.; Hussein, M. A.; Asiri, A. M.; Yamamoto, Y., Structure-property relationship of naphthalene based donor-[small pi]-acceptor organic dyes for dye-sensitized solar cells: remarkable improvement of open-circuit photovoltage. *Journal of Materials Chemistry* **2012,** *22* (42), 22550-22557.

129. Wu, F.; Zhu, L.; Zhao, S.; Song, Q.; Yang, C., Engineering of organic dyes for highly efficient p-type dye-sensitized solar cells. *Dyes and Pigments* **2016,** *124*, 93-100.

130. Mao, M.; Zhang, X.; Zhu, B.; Wang, J.; Wu, G.; Yin, Y.; Song, Q., Comparative studies of organic dyes with a quinazoline or quinoline chromophore as π-conjugated bridges for dye-sensitized solar cells. *Dyes and Pigments* **2016,** *124*, 72-81.

131. Long, J.; Liu, X.; Guo, H.; Zhao, B.; Tan, S., Effect of conjugated side groups on the photovoltaic performances of triphenylamine-based dyes sensitized solar cells. *Dyes and Pigments* **2016,** *124*, 222-231.

132. Zhou, N.; Prabakaran, K.; Lee, B.; Chang, S. H.; Harutyunyan, B.; Guo, P.; Butler, M. R.; Timalsina, A.; Bedzyk, M. J.; Ratner, M. A.; Vegiraju, S.; Yau, S.; Wu, C.-G.; Chang, R. P. H.; Facchetti, A.; Chen, M.-C.; Marks, T. J., Metal-Free Tetrathienoacene Sensitizers for High-Performance Dye-Sensitized Solar Cells. *Journal of the American Chemical Society* **2015,** *137* (13), 4414-4423.

133. Yang, Z.; Liu, C.; Shao, C.; Lin, C.; Liu, Y., First-Principles Screening and Design of Novel Triphenylamine-Based D−π–A Organic Dyes for Highly Efficient Dye-Sensitized Solar Cells. *The Journal of Physical Chemistry C* **2015,** *119* (38), 21852-21859.

134. Zhang, F.; Luo, Y.-h.; Song, J.-s.; Guo, X.-z.; Liu, W.-l.; Ma, C.-p.; Huang, Y.; Ge, M.-f.; Bo, Z.; Meng, Q.-B., Triphenylamine-based dyes for dye-sensitized solar cells. *Dyes and Pigments* **2009,** *81* (3), 224-230.

135. Murphy, L. R.; Meek, T. L.; Allred, A. L.; Allen, L. C., Evaluation and Test of Pauling's Electronegativity Scale. *The Journal of Physical Chemistry A* **2000,** *104* (24), 5867-5871.

136. Pauling, L., THE NATURE OF THE CHEMICAL BOND. IV. THE ENERGY OF SINGLE BONDS AND THE RELATIVE ELECTRONEGATIVITY OF ATOMS. *Journal of the American Chemical Society* **1932,** *54* (9), 3570-3582.

137. Fujisawa, J.-i.; Muroga, R.; Hanaya, M., Interfacial charge-transfer transitions in a TiO2-benzenedithiol complex with Ti-S-C linkages. *Physical Chemistry Chemical Physics* **2015,** *17* (44), 29867-29873.

138. Fujisawa, J.-i.; Hanaya, M., Light Harvesting and Direct Electron Injection by Interfacial Charge-Transfer Transitions between TiO2 and Carboxy-Anchor Dye LEG4 in Dye-Sensitized Solar Cells. *The Journal of Physical Chemistry C* **2018,** *122* (1), 8-15.

139. He, L.-J.; Chen, J.; Bai, F.-Q.; Jia, R.; Wang, J.; Zhang, H.-X., The influence of a dye-TiO2 interface on DSSC performance: a theoretical exploration with a ruthenium dye. *RSC Advances* **2016,** *6* (85), 81976-81982.

140. Li, Y.; Xu, B.; Song, P.; Ma, F.; Sun, M., D–A−π–A System: Light Harvesting, Charge Transfer, and Molecular Designing. *The Journal of Physical Chemistry C* **2017,** *121* (23), 12546-12561.

141. Labat, F.; Le Bahers, T.; Ciofini, I.; Adamo, C., First-Principles Modeling of Dye-Sensitized Solar Cells: Challenges and Perspectives. *Accounts of Chemical Research* **2012,** *45* (8), 1268-1277.

142. Yin, H.; Geng, Y.; Sun, G.-Y.; Su, Z.-M., Theoretical Design of Perylene Diimide Dimers with Different Linkers and Bridged Positions as Promising Non-Fullerene Acceptors for Organic Photovoltaic Cells. *The Journal of Physical Chemistry C* **2017,** *121* (4), 2125-2134.

143. Li, S.-B.; Geng, Y.; Duan, Y.-A.; Sun, G.-Y.; Zhang, M.; Qiu, Y.-Q.; Su, Z.-M., Theoretical study on the charge transfer mechanism at donor/acceptor interface: Why TTF/TCNQ is inadaptable to photovoltaics? *The Journal of Chemical Physics* **2016,** *145* (24), 244705.

144. Li, S.-B.; Duan, Y.-A.; Geng, Y.; Li, H.-B.; Zhang, J.-Z.; Xu, H.-L.; Zhang, M.; Su, Z.-M., A designed bithiopheneimide-based conjugated polymer for organic photovoltaic with ultrafast charge transfer at donor/PC71BM interface: theoretical study and characterization. *Physical Chemistry Chemical Physics* **2014,** *16* (47), 25799-25808.

145. Yu, G.; Heeger, A. J., Charge separation and photovoltaic conversion in polymer composites with internal donor/acceptor heterojunctions. *Journal of Applied Physics* **1995,** *78* (7), 4510-4515.

146. Halls, J. J. M.; Walsh, C. A.; Greenham, N. C.; Marseglia, E. A.; Friend, R. H.; Moratti, S. C.; Holmes, A. B., Efficient photodiodes from interpenetrating polymer networks. *Nature* **1995,** *376* (6540), 498-500.

147. He, Y.; Li, Y., Fullerene derivative acceptors for high performance polymer solar cells. *Physical Chemistry Chemical Physics* **2011,** *13* (6), 1970-1983.

148. Lin, Y.; Zhan, X., Designing Efficient Non-Fullerene Acceptors by Tailoring Extended Fused-Rings with Electron-Deficient Groups. *Advanced Energy Materials* **2015,** *5* (20), 1501063-n/a.

149. Jiang, W.; Ye, L.; Li, X.; Xiao, C.; Tan, F.; Zhao, W.; Hou, J.; Wang, Z., Bay-linked perylene bisimides as promising non-fullerene acceptors for organic solar cells. *Chemical Communications* **2014,** *50* (8), 1024-1026.

150. Zhao, D.; Wu, Q.; Cai, Z.; Zheng, T.; Chen, W.; Lu, J.; Yu, L., Electron Acceptors Based on α-Substituted Perylene Diimide (PDI) for Organic Solar Cells. *Chemistry of Materials* **2016,** *28* (4), 1139-1146.

151. Park, G. E.; Kim, H. J.; Choi, S.; Lee, D. H.; Uddin, M. A.; Woo, H. Y.; Cho, M. J.; Choi, D. H., New M- and V-shaped perylene diimide small molecules for high-performance nonfullerene polymer solar cells. *Chemical Communications* **2016,** *52* (57), 8873-8876.

152. Yan, Q.; Zhou, Y.; Zheng, Y.-Q.; Pei, J.; Zhao, D., Towards rational design of organic electron acceptors for photovoltaics: a study based on perylenediimide derivatives. *Chemical Science* **2013,** *4* (12), 4389-4394.

153. Zhao, J.; Li, Y.; Zhang, J.; Zhang, L.; Lai, J. Y. L.; Jiang, K.; Mu, C.; Li, Z.; Chan, C. L. C.; Hunt, A.; Mukherjee, S.; Ade, H.; Huang, X.; Yan, H., The influence of spacer units on molecular properties and solar cell performance of non-fullerene acceptors. *Journal of Materials Chemistry A* **2015,** *3* (40), 20108-20112.

154. Zhong, Y.; Trinh, M. T.; Chen, R.; Wang, W.; Khlyabich, P. P.; Kumar, B.; Xu, Q.; Nam, C.-Y.; Sfeir, M. Y.; Black, C.; Steigerwald, M. L.; Loo, Y.-L.; Xiao, S.; Ng, F.; Zhu, X. Y.; Nuckolls, C., Efficient Organic Solar Cells with Helical Perylene Diimide Electron Acceptors. *Journal of the American Chemical Society* **2014,** *136* (43), 15215-15221.

155. Zhong, H.; Wu, C.-H.; Li, C.-Z.; Carpenter, J.; Chueh, C.-C.; Chen, J.-Y.; Ade, H.; Jen, A. K. Y., Rigidifying Nonplanar Perylene Diimides by Ring Fusion Toward Geometry-Tunable Acceptors for High-Performance Fullerene-Free Solar Cells. *Advanced Materials* **2016,** *28* (5), 951-958.

156. Hartnett, P. E.; Matte, H. S. S. R.; Eastham, N. D.; Jackson, N. E.; Wu, Y.; Chen, L. X.; Ratner, M. A.; Chang, R. P. H.; Hersam, M. C.; Wasielewski, M. R.; Marks, T. J., Ring-fusion as a perylenediimide dimer design concept for high-performance non-fullerene organic photovoltaic acceptors. *Chemical Science* **2016,** *7* (6), 3543-3555.

157. Bérubé, N.; Gosselin, V.; Gaudreau, J.; Côté, M., Designing Polymers for Photovoltaic Applications Using ab Initio Calculations. *The Journal of Physical Chemistry C* **2013,** *117* (16), 7964-7972.

158. Nakano, K.; Tajima, K., Organic Planar Heterojunctions: From Models for Interfaces in Bulk Heterojunctions to High-Performance Solar Cells. *Advanced Materials* **2017,** *29* (25), 1603269-n/a.

159. Yao, H.; Ye, L.; Zhang, H.; Li, S.; Zhang, S.; Hou, J., Molecular Design of Benzodithiophene-Based Organic Photovoltaic Materials. *Chemical Reviews* **2016,** *116* (12), 7397-7457.

160. Ye, L.; Zhang, S.; Zhao, W.; Yao, H.; Hou, J., Highly Efficient 2D-Conjugated Benzodithiophene-Based Photovoltaic Polymer with Linear Alkylthio Side Chain. *Chemistry of Materials* **2014,** *26* (12), 3603-3605.

161. Abbotto, A.; Leandri, V.; Manfredi, N.; De Angelis, F.; Pastore, M.; Yum, J.-H.; Nazeeruddin, M. K.; Grätzel, M., Bis-Donor–Bis-Acceptor Tribranched Organic Sensitizers for Dye-Sensitized Solar Cells. *European Journal of Organic Chemistry* **2011,** *2011* (31), 6195-6205.

162. De Angelis, F.; Fantacci, S.; Gebauer, R., Simulating Dye-Sensitized TiO2 Heterointerfaces in Explicit Solvent: Absorption Spectra, Energy Levels, and Dye Desorption. *The Journal of Physical Chemistry Letters* **2011,** *2* (7), 813-817.

163. Pastore, M.; Mosconi, E.; De Angelis, F., Computational Investigation of Dye–Iodine Interactions in Organic Dye-Sensitized Solar Cells. *The Journal of Physical Chemistry C* **2012,** *116* (9), 5965-5973.

164. Yin, B.; Yang, L.; Liu, Y.; Chen, Y.; Qi, Q.; Zhang, F.; Yin, S., Solution-processed bulk heterojunction organic solar cells based on an oligothiophene derivative. *Applied Physics Letters* **2010,** *97* (2), 023303.

165. Valiev, M.; Bylaska, E. J.; Govind, N.; Kowalski, K.; Straatsma, T. P.; Van Dam, H. J. J.; Wang, D.; Nieplocha, J.; Apra, E.; Windus, T. L.; de Jong, W. A., NWChem: A comprehensive and scalable open-source solution for large scale molecular simulations. *Computer Physics Communications* **2010,** *181* (9), 1477-1489.

166. Liu, T.; Troisi, A., Absolute Rate of Charge Separation and Recombination in a Molecular Model of the P3HT/PCBM Interface. *The Journal of Physical Chemistry C* **2011,** *115* (5), 2406-2415.

167. Shi, L.-L.; Liao, Y.; Yang, G.-C.; Su, Z.-M.; Zhao, S.-S., Effect of π-Conjugated Length of Bridging Ligand on the Optoelectronic Properties of Platinum(II) Dimers. *Inorganic Chemistry* **2008,** *47* (7), 2347-2355.

168. Kavarnos, G. J.; Turro, N. J., Photosensitization by reversible electron transfer: theories, experimental evidence, and examples. *Chemical Reviews* **1986,** *86* (2), 401-449.

169. Li, Y.; Pullerits, T.; Zhao, M.; Sun, M., Theoretical Characterization of the PC60BM:PDDTT Model for an Organic Solar Cell. *The Journal of Physical Chemistry C* **2011,** *115* (44), 21865-21873.

170. Song, P.; Li, Y.; Ma, F.; Pullerits, T.; Sun, M., External Electric Field-Dependent Photoinduced Charge Transfer in a Donor–Acceptor System for an Organic Solar Cell. *The Journal of Physical Chemistry C* **2013,** *117* (31), 15879-15889.

171. Koster, L. J. A.; Shaheen Sean, E.; Hummelen Jan, C., Pathways to a New Efficiency Regime for Organic Solar Cells. *Advanced Energy Materials* **2012,** *2* (10), 1246-1253.

172. Dimitrov, S. D.; Bakulin, A. A.; Nielsen, C. B.; Schroeder, B. C.; Du, J.; Bronstein, H.; McCulloch, I.; Friend, R. H.; Durrant, J. R., On the Energetic Dependence of Charge Separation in Low-Band-Gap Polymer/Fullerene Blends. *Journal of the American Chemical Society* **2012,** *134* (44), 18189-18192.

173. Song, P.; Li, Y.; Ma, F.; Sun, M., Insight into external electric field dependent photoinduced intermolecular charge transport in BHJ solar cell materials. *Journal of Materials Chemistry C* **2015,** *3* (18), 4810-4819.

174. Sutton, C.; Sears, J. S.; Coropceanu, V.; Brédas, J.-L., Understanding the Density Functional Dependence of DFT-Calculated Electronic Couplings in Organic Semiconductors. *The Journal of Physical Chemistry Letters* **2013,** *4* (6), 919-924.

175. Thorley, K. J.; Risko, C., Mapping the configuration dependence of electronic coupling in organic semiconductors. *Journal of Materials Chemistry C* **2016,** *4* (17), 3825-3832.

176. Yang, C.-H.; Hsu, C.-P., The dynamical correlation in spacer-mediated electron transfer couplings. *The Journal of Chemical Physics* **2006,** *124* (24), 244507.

177. Hsu, C.-P., The Electronic Couplings in Electron Transfer and Excitation Energy Transfer. *Accounts of Chemical Research* **2009,** *42* (4), 509-518.

178. Farazdel, A.; Dupuis, M.; Clementi, E.; Aviram, A., Electric-field induced intramolecular electron transfer in spiro .pi.-electron systems and their suitability as molecular electronic devices. A theoretical study. *Journal of the American Chemical Society* **1990,** *112* (11), 4206-4214.

179. Scharber, M. C.; Mühlbacher, D.; Koppe, M.; Denk, P.; Waldauf, C.; Heeger, A. J.; Brabec, C. J., Design Rules for Donors in Bulk-Heterojunction Solar Cells—Towards 10 % Energy-Conversion Efficiency. *Advanced Materials* **2006,** *18* (6), 789-794.

180. Douglas, J. D.; Chen, M. S.; Niskala, J. R.; Lee, O. P.; Yiu, A. T.; Young, E. P.; Fréchet, J. M. J., Solution-Processed, Molecular Photovoltaics that Exploit Hole Transfer from Non-Fullerene, n-Type Materials. *Advanced Materials* **2014,** *26* (25), 4313-4319.

181. Nielsen, C. B.; Holliday, S.; Chen, H.-Y.; Cryer, S. J.; McCulloch, I., Non-Fullerene Electron Acceptors for Use in Organic Solar Cells. *Accounts of Chemical Research* **2015,** *48* (11), 2803-2812.

182. Fang, Y.; Pandey Ajay, K.; Nardes Alexandre, M.; Kopidakis, N.; Burn Paul, L.; Meredith, P., A Narrow Optical Gap Small Molecule Acceptor for Organic Solar Cells. *Advanced Energy Materials* **2012,** *3* (1), 54-59.

183. Zhang, S.; Uddin, M. A.; Zhao, W.; Ye, L.; Woo, H. Y.; Liu, D.; Yang, B.; Yao, H.; Cui, Y.; Hou, J., Optimization of side chains in alkylthiothiophene-substituted benzo[1,2-b:4,5-b[prime or minute]]dithiophene-based photovoltaic polymers. *Polymer Chemistry* **2015,** *6* (14), 2752-2760.

184. Zhang, X.; Li, W.; Yao, J.; Zhan, C., High-Efficiency Nonfullerene Polymer Solar Cell Enabling by Integration of Film-Morphology Optimization, Donor Selection, and Interfacial Engineering. *ACS Applied Materials & Interfaces* **2016,** *8* (24), 15415-15421.

185. Jiang, B.; Zhang, X.; Zheng, Y.; Yu, G.; Yao, J.; Zhan, C., A comparative study of photovoltaic performance between non-fullerene and fullerene based organic solar cells. *RSC Advances* **2016,** *6* (49), 43715-43718.

186. Schleyer, P. v. R.; Maerker, C.; Dransfeld, A.; Jiao, H.; van Eikema Hommes, N. J. R., Nucleus-Independent Chemical Shifts: A Simple and Efficient Aromaticity Probe. *Journal of the American Chemical Society* **1996,** *118* (26), 6317-6318.

187. Stanger, A., Nucleus-Independent Chemical Shifts (NICS): Distance Dependence and Revised Criteria for Aromaticity and Antiaromaticity. *The Journal of Organic Chemistry* **2006,** *71* (3), 883-893.

188. Chen, Z.; Wannere, C. S.; Corminboeuf, C.; Puchta, R.; Schleyer, P. v. R., Nucleus-Independent Chemical Shifts (NICS) as an Aromaticity Criterion. *Chemical Reviews* **2005,** *105* (10), 3842-3888.

189. Fallah-Bagher-Shaidaei, H.; Wannere, C. S.; Corminboeuf, C.; Puchta, R.; Schleyer, P. v. R., Which NICS Aromaticity Index for Planar π Rings Is Best? *Organic Letters* **2006,** *8* (5), 863-866.

190. Stanger, A., Obtaining Relative Induced Ring Currents Quantitatively from NICS. *The Journal of Organic Chemistry* **2010,** *75* (7), 2281-2288.

191. Darling, S. B.; You, F., The case for organic photovoltaics. *RSC Advances* **2013,** *3* (39), 17633-17648.

192. Shi, Q.; Zhang, S.; Zhang, J.; Oswald, V. F.; Amassian, A.; Marder, S. R.; Blakey, S. B., KOtBu-Initiated Aryl C–H Iodination: A Powerful Tool for the Synthesis of High Electron Affinity Compounds. *Journal of the American Chemical Society* **2016,** *138* (12), 3946-3949.

193. Deng, W.-Q.; Goddard, W. A., Predictions of Hole Mobilities in Oligoacene Organic Semiconductors from Quantum Mechanical Calculations. *The Journal of Physical Chemistry B* **2004,** *108* (25), 8614-8621.

194. Fan, S.; Lu, X.; Sun, H.; Zhou, G.; Chang, Y. J.; Wang, Z.-S., Effect of the co-sensitization sequence on the performance of dye-sensitized solar cells with porphyrin and organic dyes. *Physical Chemistry Chemical Physics* **2016,** *18* (2), 932-938.

195. Xie, Y.; Tang, Y.; Wu, W.; Wang, Y.; Liu, J.; Li, X.; Tian, H.; Zhu, W.-H., Porphyrin Cosensitization for a Photovoltaic Efficiency of 11.5%: A Record for Non-Ruthenium Solar Cells Based on Iodine Electrolyte. *Journal of the American Chemical Society* **2015,** *137* (44), 14055-14058.

196. Lodermeyer, F.; Costa Rubén, D.; Malig, J.; Jux, N.; Guldi Dirk, M., Benzoporphyrins: Selective Co-sensitization in Dye-Sensitized Solar Cells. *Chemistry – A European Journal* **2016,** *22* (23), 7851-7855.

197. Singh, E.; Kim, K. S.; Yeom, G. Y.; Nalwa, H. S., Two-dimensional transition metal dichalcogenide-based counter electrodes for dye-sensitized solar cells. *RSC Advances* **2017,** *7* (45), 28234-28290.

198. Hussain, S.; Patil, S. A.; Vikraman, D.; Mengal, N.; Liu, H.; Song, W.; An, K.-S.; Jeong, S. H.; Kim, H.-S.; Jung, J., Large area growth of MoTe2 films as high performance counter electrodes for dye-sensitized solar cells. *Scientific Reports* **2018,** *8* (1), 29.

199. Huang, J.; Shao, Y.; Dong, Q., Organometal Trihalide Perovskite Single Crystals: A Next Wave of Materials for 25% Efficiency Photovoltaics and Applications Beyond? *The Journal of Physical Chemistry Letters* **2015,** *6* (16), 3218-3227.

200. Yang, W. S.; Park, B.-W.; Jung, E. H.; Jeon, N. J.; Kim, Y. C.; Lee, D. U.; Shin, S. S.; Seo, J.; Kim, E. K.; Noh, J. H.; Seok, S. I., Iodide management in formamidinium-lead-halide–based perovskite layers for efficient solar cells. *Science* **2017,** *356* (6345), 1376.

201. Yang, W. S.; Noh, J. H.; Jeon, N. J.; Kim, Y. C.; Ryu, S.; Seo, J.; Seok, S. I., High-performance photovoltaic perovskite layers fabricated through intramolecular exchange. *Science* **2015,** *348* (6240), 1234.

202. Cui, Y.; Yao, H.; Gao, B.; Qin, Y.; Zhang, S.; Yang, B.; He, C.; Xu, B.; Hou, J., Fine-Tuned Photoactive and Interconnection Layers for Achieving over 13% Efficiency in a Fullerene-Free Tandem Organic Solar Cell. *Journal of the American Chemical Society* **2017,** *139* (21), 7302-7309.

203. Zhang, G.; Zhao, J.; Chow, P. C. Y.; Jiang, K.; Zhang, J.; Zhu, Z.; Zhang, J.; Huang, F.; Yan, H., Nonfullerene Acceptor Molecules for Bulk Heterojunction Organic Solar Cells. *Chemical Reviews* **2018,** *118* (7), 3447-3507.

204. Yang, L.; Yan, L.; You, W., Organic Solar Cells beyond One Pair of Donor–Acceptor: Ternary Blends and More. *The Journal of Physical Chemistry Letters* **2013,** *4* (11), 1802-1810.

205. Reddy, S. Y.; Kuppa, V. K., Molecular Dynamics Simulations of Organic Photovoltaic Materials: Structure and Dynamics of Oligothiophene. *The Journal of Physical Chemistry C* **2012,** *116* (28), 14873-14882.

206. Jankowski, E.; Marsh, H. S.; Jayaraman, A., Computationally Linking Molecular Features of Conjugated Polymers and Fullerene Derivatives to Bulk Heterojunction Morphology. *Macromolecules* **2013,** *46* (14), 5775-5785.

207. Lee, C.-K.; Wodo, O.; Ganapathysubramanian, B.; Pao, C.-W., Electrode Materials, Thermal Annealing Sequences, and Lateral/Vertical Phase Separation of Polymer Solar Cells from Multiscale Molecular Simulations. *ACS Applied Materials & Interfaces* **2014,** *6* (23), 20612-20624.

208. Lorenzoni, A.; Gallino, F.; Muccini, M.; Mercuri, F., Theoretical insights on morphology and charge transport properties of two-dimensional N,N[prime or minute]-ditridecylperylene-3,4,9,10-tetra carboxylic diimide aggregates. *RSC Advances* **2016,** *6* (47), 40724-40730.

209. Speelman, A. L.; Muñoz-Losa, A.; Hinkle, K. L.; VanBeek, D. B.; Mennucci, B.; Krueger, B. P., Using Molecular Dynamics and Quantum Mechanics Calculations To Model Fluorescence Observables. *The Journal of Physical Chemistry A* **2011,** *115* (16), 3997-4008.

210. Ashrafi Khajeh, A. R.; Shankar, K.; Choi, P., Prediction of the Active Layer Nanomorphology in Polymer Solar Cells Using Molecular Dynamics Simulation. *ACS Applied Materials & Interfaces* **2013,** *5* (11), 4617-4624.

211. Do, K.; Ravva, M. K.; Wang, T.; Brédas, J.-L., Computational Methodologies for Developing Structure–Morphology–Performance Relationships in Organic Solar Cells: A Protocol Review. *Chemistry of Materials* **2017,** *29* (1), 346-354.